Iron isotope fractionation in carbonatite melt systems

Maria Stuff, M. Sc. Geotechnologie

Dissertation

zur Erlangung des akademischen Grades
„doctor rerum naturalium“
(Dr. rer. nat.)
in der Wissenschaftsdisziplin Mineralogie

eingereicht an der
Mathematisch-Naturwissenschaftlichen Fakultät
der Universität Potsdam

Anfertigung der Arbeit am
Helmholtz-Zentrum Potsdam
Deutsches GeoForschungsZentrum (GFZ)

Datum der Disputation: 20. Juli 2021

Betreuer:
Prof. Dr. M. Wilke, Universität Potsdam

Gutachter:
Prof. Dr. M. Wilke, Universität Potsdam
Prof. Dr. G. Franz, Technische Universität Berlin
Prof. Dr. S. Weyer, Leibniz Universität Hannover

Published online on the
Publication Server of the University of Potsdam:
https://doi.org/10.25932/publishup-51992
https://nbn-resolving.org/urn:nbn:de:kobv:517-opus4-519928

Eidesstattliche Erklärung

Hiermit erkläre ich, dass ich die beigefügte Dissertation selbstständig verfasst und keine anderen als die angegebenen Hilfsmittel genutzt habe. Alle wörtlich oder inhaltlich übernommenen Stellen habe ich als solche gekennzeichnet. Ich versichere außerdem, dass ich die beigefügte Dissertation nur in diesem und keinem anderen Promotionsverfahren eingereicht habe und dass diesem Promotionsverfahren kein endgültig gescheitertes Promotionsverfahren vorausgegangen ist.

Berlin, den 23.03.2021
Maria Stuff

Zusammenfassung

Karbonatitische Schmelzen, die im Erdmantel gebildet werden, transportieren Material aus dem Erdmantel zur Erdkruste und ermöglichen somit Einblicke in Chemismus und Dynamiken des Erdmantels. Die Analyse stabiler Eisenisotopenverhältnisse ist eine neue und vielversprechende Methode um Schmelzprozesse und Interaktionen von Schmelzen im Erdmantel nachzuverfolgen, insbesondere da Eisenisotopenfraktionierung vom Oxidationszustand und der Bindungsumgebung in der Schmelze abhängig ist. Mittlerweile existiert ein großer Datensatz zur Eisenisotopenfraktionierung in magmatischen Gesteinen, der sowohl Zusammensetzungen von Gesamtgesteinen als auch von separierten Mineralgruppen umfasst. Karbonatite weisen extrem leichte Eisenisotopensignaturen und gleichzeitig eine breite Spannweite der δ^{56}Fe auf. Darin ähneln sie Mantelxenolithen, die ebenfalls sehr variable und teilweise extrem leichte δ^{56}Fe aufweisen, wie zum Beispiel $-0.69\,‰$ in einem Spinelllherzolith.

Ein möglicher Grund für diese große Spannweite sind metasomatische Prozesse, an denen Fluide wie hochalkalische Silikatschmelzen oder Karbonatschmelzen beteiligt sind. Welche Auswirkung Metasomatose auf die Eisenisotopenfraktionierung hat, hängt von Parametern wie dem Verhältnis von Schmelze zu Gestein, der Reaktionszeit und der Art der beteiligten metasomatischen Fluide sowie den Mineralreaktionen ab. Auch mehrere aufeinanderfolgende Phasen der Schmelzextraktion könnten zur Heterogenisierung von Teilen des Erdmantels beigetragen haben. Bisher existieren allerdings nur wenige Untersuchungen zur Eisenisotopenfraktionierung zwischen Silikat- und Karbonatphasen.

Um Eisenisotopenfraktionierung im Karbonatitsystem besser zu verstehen, wurden im Rahmen dieser Arbeit Experimente im Natrokarbonatitsystem durchgeführt. Dazu wurden unmischbare Silikat- und Karbonatschmelzen bei Temperaturen zwischen 900 und 1200 °C und Drücken von 0,5 und 0,7 GPa in einem intern beheizten Autoklaven bei intrinsischen Redoxbedingungen equilibriert. Im Anschluss wurden die Silikat- und Karbonatschmelzen separiert, aufgeschlossen und die Eisenisotopenverhältnisse beider Phasen mittels MC-ICP-MS analysiert. Dabei konnte gezeigt werden, dass die Proben nach spätestens 48 Stunden Fe-isotopisch equilibriert sind und dass im Gleichgewicht leichte Eisenisotope in der Karbonatschmelze angereichert sind.

Die größte Isotopenfraktionierung von $\Delta^{56}Fe_{\text{sil.m.-carb.m. (mean)}} = 0{,}13\,‰$ wurde in einem System mit stark peralkalischer Zusammensetzung der Silikatschmelze (ASI $\geq 0{,}21$, Na/Al $\leq 2{,}7$) gemessen. In den Systemen mit extrem peralkalischer Zusammensetzung der Silikatschmelze (ASI zwischen 0,11 and 0,14) hingegen war die Eisenisotopenfraktionierung analytisch nicht auflösbar.

Zusätzlich wurde die Eisenisotopenfraktionierung zwischen Magnetit- und

Olivinkörnern *in situ* mittels UV-Femtosekunden-Laserablation gekoppelt mit MC-ICP-MS untersucht. Bei der Probe handelt es sich um eine Melilititbombe aus der Salt-Lake-Crater-Gruppe in Honolulu (Oahu, Hawaii), die deutliche Anzeichen für Kontakt mit einer karbonatitischen Schmelze aufweist. Während die Magnetite eher homogen hinsichtlich ihrer Eisenisotopenzusammensetzung sind ($-0{,}17\,‰$, $\pm 0{,}11\,‰$, 2SE, to $+0{,}08\,‰$, $\pm 0{,}09\,‰$, 2SE), weisen die Olivine eine weitaus größere Spannweite an δ^{56}Fe auf ($-0{,}66\,‰$, $\pm 0{,}11\,‰$, 2SE, to $+0{,}10\,‰$, $\pm 0{,}13\,‰$, 2SE). Da Eisen unterschiedliche Diffusionskoeffizienten in Olivin und Magnetit hat, sind in beiden unterschiedliche Informationen zur kinetischen und Gleichgewichtsisotopenfraktionierung enthalten.

Die Beobachtungen aus den Experimenten und in den Eisenisotopenanalysen *in situ* deuten darauf hin, dass die extrem leichten Eisenisotopensignaturen in Karbonatiten durch Isotopenfraktionierung in mehreren Schritten während der Karbonatitgenese entstanden sind, die sowohl Gleichgewichts- als auch kinetische Fraktionierung umfassen können. Da die Eisenisotopensignaturen in natürlichen Systemen durch eine Kombination mehrerer Faktoren (Druck, Temperatur, Redoxbedingungen, Phasenzusammensetzung und -struktur, Zeitskala) entstehen, werden Multi-Tracer-Ansätze benötigt, um die in natürlichen Gesteinen beobachteten Signaturen zu erklären.

Abstract

Carbonatite magmatism is a highly efficient transport mechanism from Earth's mantle to the crust, thus providing insights into the chemistry and dynamics of the Earth's mantle. One evolving and promising tool for tracing magma interaction are stable iron isotopes, particularly because iron isotope fractionation is controlled by oxidation state and bonding environment. Meanwhile, a large data set on iron isotope fractionation in igneous rocks exists comprising bulk rock compositions and fractionation between mineral groups. Iron isotope data from natural carbonatite rocks are extremely light and of remarkably high variability. This resembles iron isotope data from mantle xenoliths, which are characterized by a variability in δ^{56}Fe spanning three times the range found in basalts, and by the extremely light values of some whole rock samples, reaching δ^{56}Fe as low as $-0.69\,‰$ in a spinel lherzolite. Cause to this large range of variations may be metasomatic processes, involving metasomatic agents like volatile bearing high-alkaline silicate melts or carbonate melts. The expected effects of metasomatism on iron isotope fractionation vary with parameters like melt/rock-ratio, reaction time, and the nature of metasomatic agents and mineral reactions involved. An alternative or additional way to enrich light isotopes in the mantle could be multiple phases of melt extraction. To interpret the existing data sets more knowledge on iron isotope fractionation factors is needed.

To investigate the behavior of iron isotopes in the carbonatite systems, kinetic and equilibration experiments in natro-carbonatite systems between immiscible silicate and carbonate melts were performed in an internally heated gas pressure vessel at intrinsic redox conditions at temperatures between 900 and 1200 °C and pressures of 0.5 and 0.7 GPa. The iron isotope compositions of coexisting silicate melt and carbonate melt were analyzed by solution MC-ICP-MS. The kinetic experiments employing a Fe-58 spiked starting material show that isotopic equilibrium is obtained after 48 hours. The experimental studies of equilibrium iron isotope fractionation between immiscible silicate and carbonate melts have shown that light isotopes are enriched in the carbonatite melt. The highest $\Delta^{56}Fe_{\text{sil.m.-carb.m. (mean)}}$ of $0.13\,‰$ was determined in a system with a strongly peralkaline silicate melt composition ($ASI \geq 0.21$, $Na/Al \leq 2.7$). In three systems with extremely peralkaline silicate melt compositions (ASI between 0.11 and 0.14) iron isotope fractionation could analytically not be resolved. The lowest $\Delta^{56}Fe_{\text{sil.m.-carb.m. (mean)}}$ of $0.02\,‰$ was determined in a system with an extremely peralkaline silicate melt composition ($ASI \leq 0.11$, $Na/Al \geq 6.1$). The observed iron isotope fractionation is most likely governed by the redox conditions of the system. Yet, in the systems, where no fractionation occurred, structural changes induced by compositional changes possibly overrule the influence of redox conditions. This interpretation implicates, that the iron isotope system holds the potential to be useful not only for exploring redox conditions in magmatic systems, but also for

discovering structural changes in a melt.

In situ iron isotope analyses by femtosecond laser ablation coupled to MC-ICP-MS on magnetite and olivine grains were performed to reveal variations in iron isotope composition on the micro scale. The investigated sample is a melilitite bomb from the Salt Lake Crater group at Honolulu (Oahu, Hawaii), showing strong evidence for interaction with a carbonatite melt. While magnetite grains are rather homogeneous in their iron isotope compositions, olivine grains span a far larger range in iron isotope ratios. The variability of δ^{56}Fe in magnetite is limited from $-0.17\,‰$ ($\pm 0.11\,‰$, 2SE) to $+0.08\,‰$ ($\pm 0.09\,‰$, 2SE). δ^{56}Fe in olivine range from $-0.66\,‰$ ($\pm 0.11\,‰$, 2SE) to $+0.10\,‰$ ($\pm 0.13\,‰$, 2SE). Olivine and magnetite grains hold different informations regarding kinetic and equilibrium fractionation due to their different Fe diffusion coefficients.

The observations made in the experiments and in the in situ iron isotope analyses suggest that the extremely light iron isotope signatures found in carbonatites are generated by several steps of isotope fractionation during carbonatite genesis. These may involve equilibrium and kinetic fractionation. Since iron isotopic signatures in natural systems are generated by a combination of multiple factors (pressure, temperature, redox conditions, phase composition and structure, time scale), multi tracer approaches are needed to explain signatures found in natural rocks.

Acknowledgements

First I gratefully acknowledge the funding of this research project by the Helmholtz Association through the Helmholtz-Russia Joint Research Group “Structural properties of carbonate-silicate melts and their effect on fractionation processes in the deep Earth investigated by synchrotron radiation, spectroscopic and ion probe methods” (HRJRG-404).

Further I would like to thank my supervisors Prof. Dr. Max Wilke and Dr. Jan A. Schüssler for being ready at any time to help me meet the newest upcoming challenges by advice and support in the labs and through scientific discussions and encouragement. I also owe thanks to Prof. Dr. Gerhard Franz for sparking my fascination and enthusiasm for mineralogy from the first lecture in the bachelor’s programme on.

This research was made possible through all people who provided extensive technical support. Therefore I like to thank Jutta Schlegel, Josefine Buhk, and Cathrin Schulz for their support in the HELGES-lab (and for making work a lot more fun), Hans-Peter Nabein for the constant support in the chemistry lab and daily routines, for running experiments in the CSPV, and recording XRD patterns, Andreas Ebert for showing me how to roll the Re-foil, as well as Reiner Schulz for his help and expertise with trouble-shooting and keeping the IHPV up and running. The latter, of course, required more than one caretaker, therefore I would also like to thank Matthias Kreplin, Reik Sünkel, Michael Voigt, and Wilfried Steiner.

Furthermore I like to thank Prof. Dr. Monika Koch-Müller for granting me many possiblities to share and discuss my work on conferences and workshops, Prof. Dr. Matthias Gottschalk for helping me understand the thermodynamics and calculations in the CO_2-dominated system, and Dr. Christina Günther for making long days at the SEM in Golm a welcome change in the daily routine. Further thanks is due to Uwe Dittmann for preparing samples for EMPA, and to Oona Appelt and Dr. Dieter Rhede for performing the EMP-Analyses. I would like to thank Dr. Dina Schultze and Stefan Gehrmann for their advice and practical help in finding a polishing routine for the Na-carbonate samples, Dr. Alexander Rocholl for providing the thin section of the melilitite bomb, along with data and knowledge on the salt lake crater setting, and Prof. Dr. Catherine McCammon for determining the $Fe^{3+}/\Sigma Fe$ in the silicate glasses. Much appreciated and extremely helpful were the discussions on natro-carbonatites with Dr. Ilya Veksler and Dr. Sören Wilke.

And finally: Thanks to all the iron heroes, my collegs, friends and my family, who accompanied and supported me along the way. Nils – thank you!

Contents

List of Figures

List of Tables

1 Introduction

Carbonatites are carbonate-rich magmatic rocks formed within the Earth's mantle, providing insights into chemistry and dynamics of the mantle and hence attracting the mantle geochemists interest for decades (Mitchell, 2005; Jones et al., 2013, and references therein). They can be subdivided based on their respective dominant carbonate mineral, such as calcite-, or dolomite-carbonatites, and on their corresponding major element geochemistry, i.e. Mg-, Ca-, Fe-, and natro-carbonatites (Woolley and Kempe, 1989). To interpret the information derived from carbonatites, a set of process-sensitive tracers is needed to distinguish between primordial signatures and contributions from steps in their evolution, like fractionation processes and crustal contamination (e. g. Liu et al., 2015a; Song et al., 2017). Geochemical tracers, such as light rare-earth elements (LREE) and radiogenic and stable isotopes, have already shed light on the mantle-sourced origins of carbonatites (Powell et al., 1962; Bell and Tilton, 2001, and references therein).

One evolving and promising tool for tracing magma interaction are stable iron isotopes. Meanwhile, there is a large data set on iron isotope fractionation in igneous rocks, that comprises bulk rock compositions and fractionation between mineral groups. Still, gathered data, and especially a large data set on iron isotope fractionation in carbonatites by Johnson et al. (2010), cannot be interpreted satisfyingly because iron isotope fractionation factors are unknown for a large number of phases (Dauphas et al., 2017). The overall aim of my thesis is to contribute to and enhance the fidelity of iron isotope systematics in igneous rocks for the interpretation of genetic processes. More specifically, the main objective is to experimentally determine the iron isotope fractionation factors in carbonatite melt systems. With these data, models for carbonatite genesis can be improved. An additional objective is to supplement existing data with a new perspective from the microscale. The grain-to-grain and intra-grain iron isotope fractionation in mantle-derived rocks is scarcely investigated, with the exception of iron isotope fractionation in olivine grains by Fe-Mg interdiffusion (Oeser et al., 2015, 2018; Sio et al., 2013, 2018). These along with other studies investigating a grain-to-grain iron isotope fractionation (e. g. Teng et al., 2008; Weyer and Seitz, 2012; Dziony et al., 2014) demonstrate, that information on iron isotope fractionation from the microscale can improve our understanding of magma evolution.

In the following chapters of the introduction I will explain my objectives in the current scientific context, as well as my scientific approach to address them. At the end of the introduction (section 1.4) I define the scope of my thesis and present an overview of the following chapters.

1.1 Carbonatites

Even though there are only little more than 500 known occurrences of carbonatites on Earth's surface, a large part of our knowledge about the subcontinental mantle is derived from these rocks. The mantle origin of carbonatites was established using Pb, Sr, Nd isotope and noble gas data (Powell et al., 1962; Bell and Tilton, 2001, and references therein). To decipher the information derived from carbonatites, it is necessary to understand the genetic processes from melting in the mantle to magma interaction during ascent, magma differentiation, and fluid alteration near the surface.

More than 60 years of research revealed the variability and complexity of carbonatites (compiled in numerous books and reviews, e. g. Bell, 1989; Bell et al., 1998; Mitchell, 2005; Jones et al., 2013). Within the mantle, metasomatizing carbonatite melts[1] play an important role in the redistribution of material (as discussed by Shatskiy et al., 2013; Hammouda and Keshav, 2015). Due to carbonatite melt properties such as low viscosity (e. g. Treiman, 1989; Dobson et al., 1996) and good wetting properties documented by low dihedral angles (Hunter and McKenzie, 1989; Minarik and Watson, 1995), carbonatite melts derived from low degree melting have high infiltration rates in an olivine-rich mantle. In these carbon-rich melts, silicate incompatible elements such as Ba, Sr, and REE (especially LREE) can be efficiently enriched and transported. At the surface, many carbonatite occurrences are linked to intracontinental rifting and thus provide the rare chance on insights into the subcontinental mantle. Other tectono-magmatic settings that allow carbonatite melts to approach Earth's surface are linked to orogenic cycles, or are associated with large igneous provinces and with mantle plumes (e. g. Bell and Simonetti, 2010; Woolley, 1989; Woolley and Kjarsgaard, 2008[2]).

The large variety of carbonatite occurrences is accompanied by a multitude of hypotheses regarding their petrogenetic origin. Three main mechanisms to generate a carbonatite magma have been identified, one of them being low-degree melting of a carbonated mantle that might generate primary carbonatite magmas. The other two involve the differentiation of a carbonated silicate melt, either by crystal fractionation or by exsolution of an immiscible carbonate melt. For all of these mechanisms, evidence has been found both in natural rocks and in experiments (summary e. g. in Bell et al., 1998). Further debates are concerned with the source region of carbonatite magmas (lithospheric, asthenospheric or deeper, see for example Bell and Simonetti, 2010) and with the carbon source (recycled

[1] To my knowledge, a consistent nomenclature for the use of "carbonate", "carbonatite", or "carbonatitic" is lacking. In the following I will use "carbonate melt" either for a silica-free carbon-rich melt, but also for a carbon-rich melt opposed to a immiscible silicate melt through exsolution (which may still contain silica).

[2] Woolley and Kjarsgaard (2008) visualized all known carbonatite occurrences in a global map. In the accompanying database the authors document the large variety of carbonatite rocks.

crust or juvenile carbon from a mantle source, Hammouda and Keshav, 2015, and references therein). This complexity in itself was addressed by Mitchell (2005), stating that

- carbonatites are a diverse group of rocks with a multiplicity of origins (which was already suggested by Harmer and Gittins, 1998), and that
- too few studies of carbonatite complexes combine geology, mineralogy and isotope geochemistry into an integrated petrogenetic scheme.

Many recent studies, though, pick up these recommendations and use multi-method approaches, including process sensitive tracers such as (non-traditional) stable isotope systems, to unravel the petrogenesis of the investigated carbonatites (e. g. Tappe et al., 2017; Song et al., 2017; Liu et al., 2015b; Bodeving et al., 2017). Among these, iron isotopes are evolving as a new tool to decipher magmatic systems.

1.2 Iron isotopes in igneous rocks

The progress in multicollector inductively coupled plasma mass spectrometry (MC-ICP-MS) analytical techniques about 15 years ago made it possible to resolve the very small variations in iron isotopic compositions in high temperature rocks. Since then, iron isotopes are evolving as a new tool to trace magmatic processes[3]. To geologists, iron is special because of its abundance as a major element from Earth's core to crust and its three oxidation states. These properties make iron isotopes a potential tracer of the mantle redox state (Dauphas et al., 2009). In the following chapter I present an overview from the general applications of stable isotope systems to iron isotope fractionation in igneous rocks, and from a whole rock perspective down to observations in mineral separates and on a grain-to-grain scale.

1.2.1 Notation

MC-ICP-MS is used to measure the (iron) isotope ratio in a sample. In the delta notation, the iron isotope ratio in a sample is compared to the international standard IRMM-014[4]:

$$\delta^{5x}Fe_{sample} = \left(\frac{\frac{^{5x}Fe}{^{54}Fe\,sample}}{\frac{^{5x}Fe}{^{54}Fe\,IRMM-014}} - 1 \right) \times 1000\,[‰] \tag{1.1}$$

[3]Comprehensive presentations of the development and utilization of iron isotope analytics to explore high and low temperature environments from core to space as well as geobiochemical and surficial processes can be found in Johnson et al. (2020) and Dauphas et al. (2017). In my thesis, the focus is on igneous and especially on mantle derived rocks.

[4]Institut for Reference Materials and Measurements

where x indicates ^{56}Fe, ^{57}Fe, or ^{58}Fe, respectively. In my thesis, all data on iron isotope fractionation are reported as $\delta^{56/54}\text{Fe}_{\text{IRMM-014}}$, if not indicated otherwise. From cited data given as $\delta^{56/54}\text{Fe}_{\text{IR}}$, in which IR stands for the average of terrestrial igneous rocks, $\delta^{56/54}\text{Fe}_{\text{IRMM-014}}$ was calculated as $\delta^{56}\text{Fe}_{\text{IRMM-014}} = 0.09 + \delta^{56}\text{Fe}_{\text{IR}}$ (valid for isotopic fractionation close to 0). In cases where literature data on iron isotope fractionation were reported as $\delta^{57/54}\text{Fe}_{\text{IRMM-014}}$ only, $\delta^{56/54}\text{Fe}_{\text{IRMM-014}}$ were calculated using a linear approximation (valid over small ranges in isotopic composition) of the mass-depenent fractionation law (Johnson et al., 2004): $\delta^{56/54}\text{Fe} = (m_{56} - m_{54})/(m_{57} - m_{54}) * \delta^{57/56}\text{Fe}$, i. e. $\delta^{56/54}\text{Fe} = 0.67 * \delta^{57/54}\text{Fe}$.

The equilibrium iron isotope fractionation between two phases (A, B) can be described by the equilibrium iron isotope fractionation factor

$$\alpha_{A-B} = \frac{R_A}{R_B} \tag{1.2}$$

in which R is the measured isotope ratio $R = {}^{56}\text{Fe}/{}^{54}\text{Fe}$ in phase A and phase B, respectively. A very convenient way to estimate the iron isotope fractionation between two phases is to approximate α_{A-B} by using the difference between the δ^{56}Fe values, which is valid for small δ^{56}Fe:

$$\Delta^{56}\text{Fe}_{A-B} = \delta^{56}\text{Fe}_A - \delta^{56}\text{Fe}_B \approx 1000 \ln \alpha_{A-B}. \tag{1.3}$$

Besides measuring iron isotope ratios directly, there are two more methods to obtain estimates of equilibrium iron isotope fractionation factors. One approach is based on electronic structure theory and computational methods (Schauble et al., 2001; Dauphas et al., 2017). In the other approach, data from Mössbauer spectroscopy (Polyakov et al., 2007; Polyakov and Mineev, 2000) or from nuclear resonant inelastic X-ray scattering (NRIXS, Polyakov et al. (2007); Dauphas et al. (2012) are used to investigate the vibrational properties of iron in solids[5]. From these two approaches the reduced partition function ratio is derived, which is referred to as β-factor. β-factors can be expressed as a function of the mean force constant of iron bonds, F (Bigeleisen and Goeppert-Mayer, 1947):

$$1000 \ln \beta = 1000 \left(\frac{1}{m_{54}} - \frac{1}{m_{56}} \right) \frac{\hbar^2}{8k^2T^2} F = 2904 \frac{F}{T^2} \tag{1.4}$$

in which k is the Boltzman constant, T is the temperature and $\hbar$ the reduced Planck constant. β-factors refer to the equilibrium fractionation between a given phase and the

[5]Of these two methods, NRIXS is "far superior to Mössbauer spectroscopy" (Dauphas et al., 2012, p. 255).

reference state of monoatomic iron vapor Dauphas et al. (2017). This has the advantage that "equilibrium fractionation factors between any coexisting phases can be calculated" (Dauphas et al., 2017, p. 433) if the β-factors of the phases are known. A comprehensive collection of β-factors is provided in Dauphas et al. (2017). Experimentally determined α-values can be compared to β-factors by

$$\Delta^{56}\mathrm{Fe}_{A-B} = 1000\,(\ln\beta_A - \ln\beta_B) \approx 1000 \ln\alpha_{A-B} \approx \delta^{56}\mathrm{Fe}_A - \delta^{56}\mathrm{Fe}_B \tag{1.5}$$

as suggested by Dauphas et al. (2017).

1.2.2 Mechanisms of stable (iron) isotope fractionation

Stable isotope systems can improve the understanding of magmatic systems: they can be used to estimate pressure, temperature, and, in the case of multivalent elements, redox conditions, as well as to trace kinetic processes. Mass dependent equilibrium isotope fractionation is mainly determined by bond strength (e. g. Schauble, 2004). Heavy isotopes prefer sites that provide a high bond stiffness (i. e., high mean vibrational force constants), which correlates with stronger and shorter bonds. Bond strength in turn is linked to the molecular structure: stronger bonds correlate with low coordination numbers. Parameters that change the coordination environment of iron in melts and minerals are oxygen fugacity, chemical composition, pressure, and temperature, so these are expected to have a direct impact on iron isotope fractionation (Shahar et al., 2017, and references therein). According to Equation 1.4, equilibrium (iron) isotope fractionation factors decrease with temperature ($\backsim 1/T^2$).

A plot of Fe-O force constants against $Fe^{3+}/\Sigma Fe$ (Figure 1.1) shows the interdependence between force constants, oxidation state, and coordination environment of iron (see Dauphas et al., 2014; Roskosz et al., 2015; Sossi and O'Neill, 2017). The two oxidation states of iron in the mantle and the crust (Fe^{3+} and Fe^{2+}) are associated with different bonding environments and thus with different force constants. The force constants of pure Fe^{2+} and Fe^{3+}, respectively, can be considered as endmembers, defining distinct linear correlations for the specific coordination environments of iron in silicate phases (4-, 6-, and 8-fold coordination). The force constants of a set of rhyolite samples investigated by Dauphas et al. (2014) are slightly above the trend defined by minerals with iron in 4-fold coordination, while the force constants of basic melts define a linear array between the trends of 4- and 6-fold iron coordination (Sossi and O'Neill, 2017). The force constants Sossi and O'Neill (2017) estimated for almandine indicate that 8-fold coordinated iron may define a trend below these two. In general, heavy isotopes are enriched in minerals that incorporate Fe^{3+} over Fe^{2+}, and in minerals providing low co-

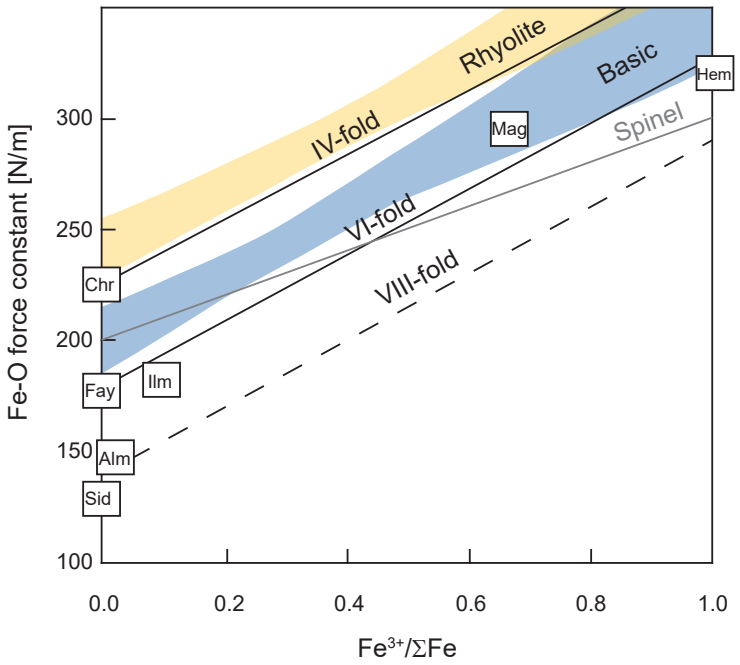

FIGURE 1.1: Fe-O force constants plotted against $Fe^{3+}/\Sigma Fe$ and coordination number (redrawn after Dauphas et al., 2014; Roskosz et al., 2015; Sossi and O'Neill, 2017). The force constants of most minerals were determined by Sossi and O'Neill (2017) and Roskosz et al. (2015, spinel), the force constant of siderite was calculated from β-factors given in Dauphas et al. (2017). Underlain are trends measured by Dauphas et al. (2014) for series of basic (basaltic to dacitic) and rhyolitic glasses; Hem = hematite, Mag = magnetite, Chr = chromite, Fay = fayalite, Ilm = ilmenite, Alm = almandine, Sid = siderite).

ordination numbers of iron. In equilibrium $\delta^{56}Fe_{almandine} < \delta^{56}Fe_{olivine} \leqslant \delta^{56}Fe_{orthopyroxene} < \delta^{56}Fe_{clinopyroxene} < \delta^{56}Fe_{spinel}$ (e. g. Polyakov and Mineev, 2000; Polyakov et al., 2007; Roskosz et al., 2015; Macris et al., 2015; Sossi and O'Neill, 2017). Force constants of iron in carbonate minerals (siderite, ankerite) are lower than in olivine (Polyakov and Mineev, 2000; Dauphas et al., 2014; Sossi and O'Neill, 2017), although iron occurs in the same oxidation state and coordination. This may be due to differences in iron bonding mechanisms in silicate and carbonate phases. Still, experiments systematically investigating iron isotope fractionation in carbonate minerals and melts are lacking.

Kinetic isotope fractionation can occur in processes where transport is involved, like diffusion, evaporation, melting and crystallization. Usually, these are one-directional processes, in which light isotopes move faster than heavy isotopes and are enriched in the reaction product, producing large kinetic isotope fractionations even at magmatic temperatures (Schauble, 2004; Richter et al., 2003). A well investigated example for kinetic iron isotope fraction occurs during Fe-Mg interdiffusion in olivine. During crystal growth from or in exchange with an evolving melt, iron diffuses into the olivine crystal in exchange for

magnesium along a chemical gradient. The iron diffusion may result in an isotopic zoning, in which the kinetic isotope fractionation exceeds equilibrium isotope fractionation by an order of magnitude (Teng et al., 2011; Weyer and Seitz, 2012; Sio et al., 2013; Oeser et al., 2015). Thus, the order of magnitude of the iron isotope fractionation can be one way identifying kinetic iron isotope fractionation in magmatic systems.

To be able to identify equilibrium iron isotope fractionation, however, the fractionation factors between the participating phases are needed. Most knowledge about equilibrium isotope fractionation of iron in high-temperature environments is derived from calculations from Mössbauer spectroscopy and NRIXS (Polyakov and Mineev, 2000; Polyakov et al., 2007; Dauphas et al., 2012, 2014; Roskosz et al., 2015), complemented by empirical observations in nature (e. g. Williams et al., 2005; Weyer and Ionov, 2007; Schuessler et al., 2009; Sossi et al., 2012; Wu et al., 2017). Experiments to determine equilibrium iron isotope fractionation factors between silicate phases and sulfides or oxides were performed by Schuessler et al. (2007); Shahar et al. (2008), and Sossi and O'Neill (2017), whereas Huang et al. (2009) contributed experiments on thermal diffusion, and Sio et al. (2018) investigated the isotope effect for Fe-Mg interdiffusion in olivine.

1.2.3 Iron isotope fractionation on the whole rock scale

The variability of iron isotope compositions observed in igneous rocks (Figure 1.2) indicates that "magmatic processes result in real, measurable and quite complex Fe-isotopic differentiation trends" (Foden et al., 2015, p. 42, see also e. g. Weyer et al., 2005; Poitrasson and Freydier, 2005; Schoenberg and von Blanckenburg, 2006). On the whole rock scale it is visible that, on average, felsic rocks are heavier than intermediate and mafic rocks by 0.10 to 0.14 ‰ in δ^{56}Fe (at a precision of usually ± 0.05 ‰ or higher), and these again are heavier than most ultramafic rocks by roughly the same value (see Figure 1.2). These effects are assigned to equilibrium iron isotope fractionation during fractional crystallization and melt extraction by partial melting: Fe^{3+} and thus heavy iron isotopes are enriched preferentially in silicate melts over Fe^{2+}-bearing minerals, due to the higher oxidation state and lower coordination numbers provided in silicate melts (Weyer, 2008; Dauphas et al., 2009; Poitrasson et al., 2013; Foden et al., 2015). The difference in iron isotope compositions between mid-ocean ridge basalt (MORB) and ocean island basalt (OIB) can be explained by the difference in their mantle source (e. g. Williams and Bizimis, 2014; Sun et al., 2020; Teng et al., 2013). The assumption that the mantle is rather heterogeneous regarding its iron isotopic composition is also supported by findings in mantle xenoliths.

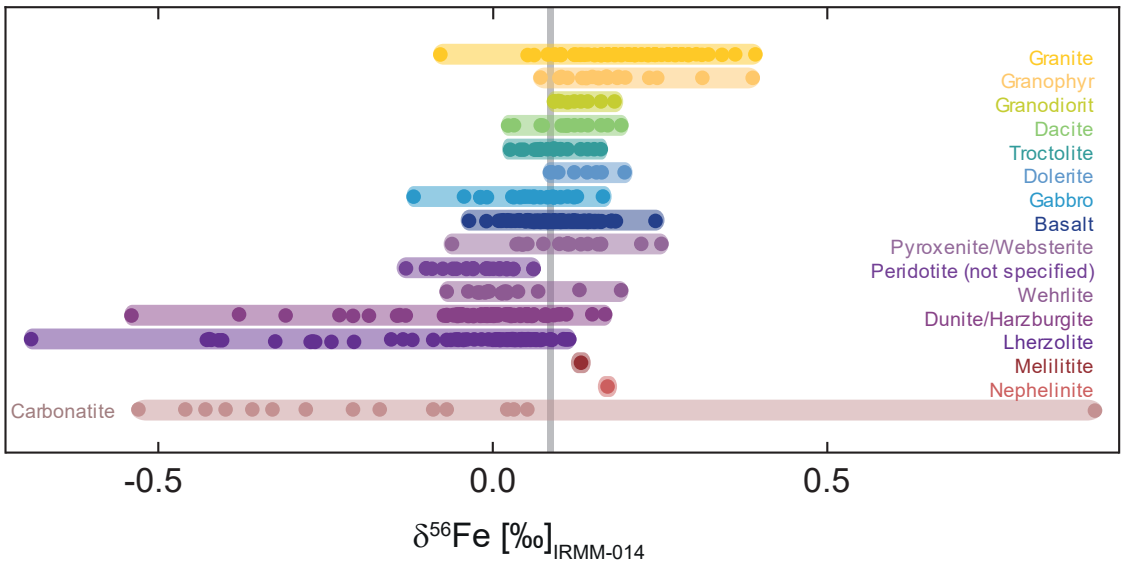

FIGURE 1.2: Data compilation of iron isotope compositions in igneous whole rocks[6]. Bars indicate the range found in the respective rocks, whereas each circle represents a bulk rock analysis.

Mantle xenoliths are characterized by

- their δ^{56}Fe values spanning three times the range found in basalts, and
- the extremely light values found in some samples, reaching δ^{56}Fe as low as -0.69 ‰ (Beard and Johnson, 2004; Williams et al., 2005; Weyer and Ionov, 2007; Poitrasson et al., 2013; Williams and Bizimis, 2014; Zhao et al., 2012, 2015).

Interestingly, these two features are shared by carbonatite rocks, as observed by Johnson et al. (2010). Johnson et al. (2010) analyzed the iron isotopic compositions of carbonatite bulk rock samples and mineral separates of 17 carbonatite complexes from four continents (details on mineral separates see subsection 1.2.4). They found that δ^{56}Fe in the investigated bulk rock carbonatite samples range from -0.53 to $+0.05$ ‰, and in one exceptionally heavy sample reach up to $+0.89$ ‰. The majority of the samples was significantly lighter than average ultramafic rocks (see Figure 1.2). Johnson et al. (2010) explained the extremely heavy signature in one sample by fluid-rock mixing with a Fe^{3+}-rich fluid at crustal levels, and the extremely light δ^{56}Fe values by a chain of genetic events. To estimate direction and order of magnitude of the iron isotope fractionation, Johnson et al. (2010) used the predictions of Polyakov and Mineev (2000) and Polyakov et al. (2007) on fractionation between silicate and carbonate minerals. According to these assumptions, equilibrium iron isotope fractionation between a calcio-carbonate magma and the mantle would enrich light isotopes in the carbonate magma. Further steps of carbonatite magma evolution, such as crystal fractionation, liquid immiscibility, and finally the loss of Fe^{3+}-rich fluids at crustal levels, would then move the iron isotope ratios of the carbonatite

melt to even lighter values. Kinetic effects as a cause of the extremely light δ^{56}Fe in carbonatites and the role of carbonatite melts as metasomatic agents were not discussed by Johnson et al. (2010). Yet, they play a role in the discussion of extremely light δ^{56}Fe in mantle xenoliths.

Both heavy and extremely light δ^{56}Fe of mantle xenoliths can be explained by metasomatic processes and multiple phases of melt extraction. Extremely light δ^{56}Fe may be generated in one-directional processes during which the faster moving light (iron) isotopes would be enriched in the product, i. e. first in the transport medium and then in the metasomatized host rock. This should create a corresponding source region depleted in light iron isotopes, i. e. with a heavy δ^{56}Fe signature. (e. g. Williams and Bizimis, 2014; Weyer and Ionov, 2007; Zhao et al., 2012, 2015). The effects of metasomatism may vary with parameters like melt/rock-ratio, reaction time, chemical disequilibrium between host rock and melt or fluid, and the nature of metasomatic agents and mineral reactions involved (see Poitrasson et al., 2013 and references therein). Given the multitude of possibilities, "it is difficult to identify the contributions of specific processes to the observed isotopic signature" (Teng et al., 2008, p. 1620), and without more knowledge on iron isotope fractionation factors, interpretations of the existing data sets remain ambiguous.

Recent research has shown that carbon takes part in many melting processes that produce potential metasomatic agents such as Fe-rich supercritical aqueous fluids, volatile or CO_2-bearing high alkaline silicate melts, carbonate and carbonatite melts, and high-CO_2 high-H_2O incipient melts (e. g. Poitrasson et al., 2013; Beard and Johnson, 2004; Williams et al., 2005; Zhao et al., 2015, 2017a; Hammouda and Keshav, 2015; Gaillard et al., 2019). The mobility of carbon in the Earth's mantle is linked not only to pressure and temperature conditions, but also to oxygen fugacity (Stagno et al., 2019). Iron isotopes as a redox sensitive tracer may therefore be a key to a better understanding of transport processes in Earth's mantle. To improve the discussion around the extremely light δ^{56}Fe in carbonatites and mantle xenoliths and the processes that may cause these, equilibrium iron isotope fractionation factors between carbonate melts, silicate phases, and oxides are needed to distinguish between equilibrium and kinetic iron isotope fractionation. Therefore, the main objective of my thesis is to experimentally determine the equilibrium iron isotope fractionation factors

[6]Williams et al. (2005); Weyer et al. (2005); Poitrasson and Freydier (2005); Schoenberg and von Blanckenburg (2006); Weyer and Ionov (2007); Heimann et al. (2008); Teng et al. (2008); Dauphas et al. (2009); Schuessler et al. (2009); Johnson et al. (2010); Sossi et al. (2012); Weyer and Seitz (2012); Zhao et al. (2012, 2015, 2017b); Poitrasson et al. (2013); Craddock et al. (2013); Williams and Bizimis (2014); Teng et al. (2013); Chen et al. (2014); Foden et al. (2015); Nebel et al. (2015); Su et al. (2015); Wu et al. (2017); An et al. (2017).

- between silicate and carbonate immiscible melts,
- between magnetite and carbonate minerals and a carbonatite melt (systems with silica)
- between magnetite, calcite, and carbonate melt (silica free systems)

(see section 1.3). As a further benefit, my experiments provide the iron distribution between the phases involved and an estimate of iron isotope equilibration times. While experiments were successful in determining iron isotope fractionation factors between silicate and carbonate melts, phase relation experiments that produced magnetite, calcite and carbonate melt could not be used for iron isotope analyses, since the phases could not be separated sufficiently for iron isotope analyses (subsection 4.1.2). My experimental approach is explained in more detail in section 1.3.

1.2.4 Mineral separates and smaller scales

The analysis of mineral separates can help detecting equilibrium or disequilibrium conditions. During sample digestion, the different mineral groups are separated chemically by sequential extraction. The subsequent iron isotope analyses of the solutions provide the apparent inter-mineral iron isotope fractionation between different minerals (and melt). Thus, kinetic processes like metasomatism and phenocryst and magma mixing can be identified, as long as at least one mineral group is affected significantly by one of these processes (see e. g. Johnson et al., 2010; Sossi et al., 2012; Weyer and Seitz, 2012; Williams and Bizimis, 2014). The mineral separates from the carbonatites investigated by Johnson et al. (2010) mostly indicate disequilibrium iron isotope fractionation between silicates, carbonates, oxides, and sulfides, with the exception of three samples recording iron isotopic equilibrium between olivine and magnetite. According to Johnson et al. (2010), these findings underline the "cumulate nature" of most carbonatites.

As in the study of Johnson et al. (2010), mineral separate analyses often are sufficient to identify iron isotopic disequilibrium. Yet, there is one drawback of this method. In the average of a mineral separate analysis consisting of many individual grains, local kinetic signatures might be averaged out. They become visible on a grain-to-grain scale, though. The first studies to report large differences in iron isotope compositions ($> 0.8\,‰$ in δ^{56}Fe) between single olivine grains of the same hand specimen are Teng et al. (2008), investigating single olivine grains from pristine Hawaiian basalts, and Weyer and Seitz (2012), investigating single olivine grains from a nephelinite specimen. The authors suggested that strong thermal (Teng et al., 2008) and chemical (Weyer and Seitz, 2012) gradients between melt, pheno-, and xenocrysts amplified the kinetic exchange. Further evidence for iron isotope variability within mineral groups on the thin section scale was presented by Dziony

et al. (2014). They discovered differences in iron isotope composition $>0.70\,‰$ in δ^{56}Fe (precision $<0.1\,‰$, 2σ level) within mineral groups in a basalt thin section, which were caused by a hydrothermal metamorphic overprint. Even more information can be gained from in situ iron isotope analyses that resolve intra-grain iron isotope analyses. Sio et al. (2013, 2018) and Oeser et al. (2014, 2015, 2018) observed iron (and magnesium) isotope fractionation within olivine grains exceeding equilibrium iron isotope fractionation by an order of magnitude. These signatures were generated by chemical Fe-Mg interdiffusion. The combination of in situ Fe and Mg isotope analyses with Fe-Mg chemical zoning can be used to unravel the complex zoning patterns in olivine grains caused by crystal growth and Fe-Mg interdiffusion. With this knowlegde, magma mixing-to-eruption timescales can be estimated (Oeser et al., 2015, 2018). All of these studies indicate, that the mm- to micro-scale holds information that will be missed out in bulk rock and mineral separate analyses. Yet, to date only few in situ iron isotope analyses of mantle derived rocks exist.

To analyze in situ iron isotope fractionation, ultraviolet femtosecond (UV-fs) laser ablation is a straightforward method (Dziony et al., 2014; Oeser et al., 2014, 2015, 2018). To complement the existing data of single-grain analyses in mantle derived rocks, iron isotope ratios of magnetite and olivine grains in a melilitite bomb from the Salt Lake Crater (SLC; Oahu, Hawaii) were analyzed by in situ UV-fs laser ablation coupled to MC-ICP-MS. The sample has been collected and characterized by A. Rocholl, who found strong geochemical and petrographical evidence for magma mixing with a carbonatite magma in the sample (see section 2.2). Most olivine grains in this sample also have Fe-Mg zoning patterns, pointing to a complex magma evolution including most likely several events of magma mixing. For this sample, I address the questions

- do iron isotope ratios in olivine and magnetite record information on magma mixing? If this is the case,
- are olivine and magnetite grains affected in a similar way, and
- could a carbonatite signal (like markedly light isotopic signatures) be identified?

A further question could be, whether iron isotope signatures of olivine and magnetite can be used as a geothermometer, given that equilibrium iron isotope fractionation at high temperature between these minerals is thouroughly investigated (Dauphas et al. (2017) and references therein). Since the petrologic and chemical evidence indicates a complicated genetic history of magma mixing events, it is unlikely to find equilibrated phases. To my knowledge, my analyses provide the first data set on single-grain analyses of olivine and magnetite in a plume derived sample.

1.3 Experimental strategy

1.3.1 Experiments in the natro-carbonatite system

Oldoinyo Lengai is the only carbonatite volcano active today. Since it is producing an alkali-rich carbonatite magma, the natro-carbonatite system is one of the most thoroughly investigated carbonatite systems, both in nature and experiment (in nature: e. g. Dawson, 1962; Zaitsev et al., 2008; de Moor et al., 2013; Li et al., 2016; Potter et al., 2017; in experiments: e. g. Koster van Groos and Wyllie, 1966; Freestone and Hamilton, 1980; Brooker and Kjarsgaard, 2011). This makes the natrocarbonatite system a convenient starting point for my experiments. The phase relations in dependence of total pressure (P), temperature (T), and carbon dioxide partial pressure (p_{CO2}) (Brooker, 1998), and trace element partitioning between the phases in the natrocarbonatite system are well known for a large number of elements and compositions (e. g. Veksler et al., 2012; Martin et al., 2012, 2013) – with the exception of iron. Since iron causes trouble in most experimental setups, only few reliable data exist on phase relations that include iron and the partitioning of iron in the carbonatite system (some successful experiments were done by Brooker, 1998). Thus, the first aim of my studies was to test a capsule design that prevented the reaction of iron and the platinum capsule. With this design it was possible to investigate the influence of iron on the phase stabilites in the natro-carbonatite system. Experiments in the internally heated pressure vessel (IHPV) and cold seal pressure vessel (CSPV) at varying pressure and temperature were perfomed to find stable

- silicate and carbonate immiscible melts (starting materials KGW and BR designed after Koster van Groos and Wyllie, 1973, and Brooker, 1998, respectively)
- magnetite, carbonate minerals, and a carbonatite (i. e. silica containing) melt (starting material KB, designed after Kjarsgaard (1998) and Brooker and Kjarsgaard (2011))
- magnetite, calcite, and carbonate melt (a silica free system, starting material CaNa)

The compositions of the starting materials shown in Figure 1.3 are given in Table 2.1 - Table 2.2 in subsection 2.1.2.

For the experimental determination of iron isotope fractionation factors based on isotope analyses with MC-ICP-MS (in solutions or by laser ablation), a number of requirements have to be fulfilled. A sample needs to 1) have at least two iron-containing phases, that 2) need to be separable for subsequent solution analyses (or spatially resolvable for laser ablation analyses). The lower the iron content in one of the phases, the higher the

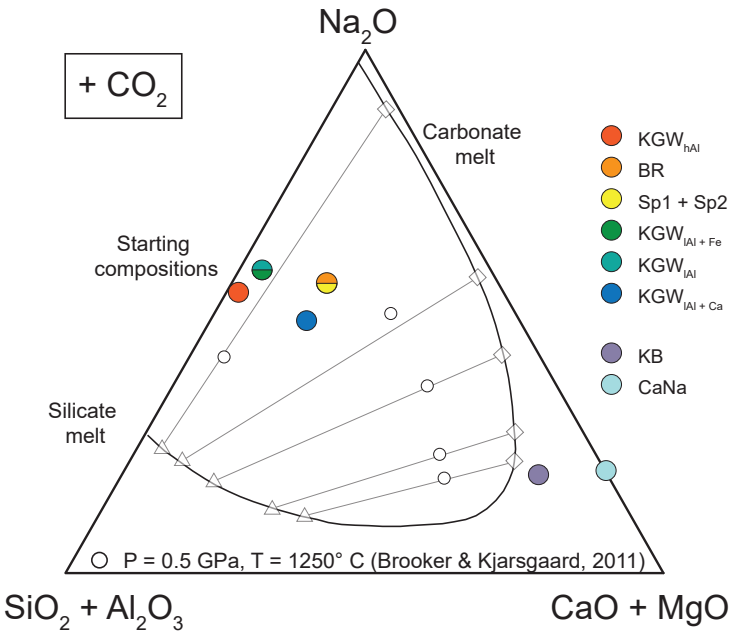

FIGURE 1.3: Hamilton-plot of the natro-carbonatite system. Here the starting composition of the phase and equilibration experiments are presented in a quasi-ternary plot projected from CO_2. The extend of the miscibility gap between silicate and carbonate melts was mapped out by Brooker and Kjarsgaard (2011). To allow for a better comparison with their experiments, the iron content is intentionally not represented in this figure. The isotope kinetic and equilibration experiments (system Sp, and systems BR and KGW, respectively) supposed to produce silicate and carbonate melts are located in the miscibility gap. The starting compositions of the phase stability experiments (systems KB and CaNa), in which the occurrence of a silicate melt was not desired, are located on the carbonate side.

demand for quantitative separation of the two phases. After these requirements are met, 3) controls on isotopic equilibrium are needed. In this work, a sufficient phase separation could be realized only in experiments producing immiscible silicate and carbonate melts (subsection 4.1.2). Thus, further strategies were developed only for this experimental design. Control on iron isotopic equilibrium between the silicate and carbonate melts was established by time series experiments including run durations from 2 to 92 hours (subsection 2.1.1) and by kinetic experiments (subsection 2.1.2). In the kinetic experiments, a Fe-58 doped glass (representing the silicate liquid) equilibrated with a mixed carbonate and oxide powder (representing the carbonate liquid). This sensitive enriched-isotope tracer approach was conducted using time series experiments between 3 and 92 hours. To investigate possible effects of composition and structure on iron isotope fractionation, six different chemical compositions within the two-liquid field were investigated. The starting material KGW has the additional advantage of a stable two liquid field at very low temperatures (750 °C in the experiments by Koster van Groos and Wyllie, 1973), thus allowing to investigate the effect of temperature on iron isotope fractionation.

1.3.2 Controls on iron isotope fractionation between silicate and carbonate immiscible melts

Measurable iron isotope equilibrium fractionation can be expected even at high temperatures, as long as the involved phases provide distinct coordination environments and/or oxidation states for iron and thus differ in iron bond strength (Dauphas et al., 2017 and references therein). Between silicate melts (polymerized networks) and carbonate melts (ionic fluids) this should be the case. Presumably, the polymerized networks of silicate melts provide stronger bonds for iron than the open frameworks in the carbonate melt. This would lead to enrichment of heavy iron isotopes in the silicate melt. A difference in Fe oxidation state between the co-existing silicate and carbonate melt might further enhance this effect. Since melt structure is essential for iron isotope fractionation, the structure of silicate and carbonate melts are described in more detail in the following.

Silicate melt structure

In a silicate melt, Si-tetrahedra connected by oxygen atoms form polymerized three-dimensional networks. In addition to silicon, some cations that can adopt a tetrahedral coordination (e. g. Al^{3+}, Fe^{3+}) act as network forming units. Other cations either function as charge balance to the network forming Al^{3+} or Fe^{3+}, or act as network modifiers, which are accommodated in larger sites (see Hudon and Baker, 2002a, and references therein). Network modifying cations bind to oxygen atoms, which are then no longer bridging two tetrahedral units and therefore are referred to as non-bridging oxygens (NBO).

Assuming the behavior of all cations is known, the degree of polymerization can be assessed by counting the NBO per tetrahedral unit (T) (Mysen et al., 1985). The highest degree of polymerization is reached if all oxygens are bridging oxygens (NBO/T = 0), which corresponds to a 3d-polymeric network. With increasing number of network modifying cations, the number of NBO increases and the silicate 3d-network is broken down to connected sheet and chain structures (e. g. Mysen et al., 1980; Murdoch et al., 1985).

Which role cations assume in a silicate melt, is predominantly determined by their size and electronegativity. Large cations like Na^{+} and Ca^{2+} usually have coordination numbers of 5 or higher and act as network modifiers (e. g. Hudon and Baker, 2002a). Intermediate smaller cations like Al^{3+} can adopt a tetrahedral coordination and act as network formers, where they need to be charge balanced by network modifying cations, or they adopt higher coordination numbers and act as network modifying cations. Iron in silicate melts occurs as ferrous and ferric iron, and in both oxidation states it achieves a 4- to 6-fold coordination (Wilke et al., 2001, 2007; Farges et al., 2004; Kim et al., 2016, and references therein). Fe^{3+} more often assumes a tetrahedral symmetry and acts as network former, while the

site symmetry of Fe^{2+} is more ambiguous. On average, Fe^{2+} occurs in 5-fold coordination, acting as network modifier (e. g. Farges et al., 2004; Wilke et al., 2004).

CO_2 speciation in the silicate melt is controlled by composition, pressure and temperature (e. g. Brooker et al., 2001b, and references therein). CO_2 occurs in three potential figurations in a silicate melt,

- as free ionic carbonate $M^{n+}\,CO_3^{2-}$ groups (FIC, with M = Ca, Na, Fe, ...), which are disconnected from the silicate network
- attached to a network tetrahedra via a non-bridging oxygen (acting as a depolymerizing agent)
- as bridging element between two tetrahedral units (promoting the polymerization of the melt)

Of these dissolution mechanisms, the dissolution of CO_2 in the silicate melt structure as FIC is considered to be the predominant one for low silica (30-40 wt % SiO_2) depolymerized melts (Xue et al., 2018; Morizet et al., 2015, 2017; Moussallam et al., 2016). The FIC groups are disconnected from the silicate network and form a carbonate subnetwork within the silicate network, a precursor of immiscibility. This leads to a higher degree of polymerization in the silicate network itself, but at the same time the silicate melt becomes diluted by the carbonate subnetworks (Morizet et al., 2017).

Carbonate melt structure

Carbonate melts are ionic fluids consisting of carbonate anions and cations. In contrast to silicate melts, the carbonate groups are unable to polymerize. Hence, most carbonate melts do not quench to a glass. Consequently, investigation and knowledge of structural properties of carbonate melts are rather restricted, compared to what is known about silicate melts. It is assumed that carbonate melts form open frameworks in which metal cations act as bridging elements between the carbonate groups (Genge et al., 1995b). The term “framework” is used to indicate that the carbonate melt cannot polymerize to a rigid structure such as the silicate three-dimensional “network”. However, in recent studies by high energy XRD and simulations in the temperature range between 1100 K and 1600 K, carbonate chains were found in molten carbonates at low temperatures, forming low dimensional networks (Wilding et al., 2016). The diversity in coordination environments resulting from the loose framework structures or low dimensional networks enhances the large ion solubility in carbonate melts.

With regard to iron isotope fractionation between silicate and carbonate melts, it is of interest,

- whether iron can be expected to dissolve in the carbonate melt,
- which would be the preferred speciation of iron in the systems investigated in this study,
- whether iron bonds are stronger or weaker in the carbonate melt compared to the silicate melt

From research developing molten carbonate fuel cells (MCFC) it is known that the transition metals Ni and Fe readily dissolve in alkali metal carbonate melts. The dissolution of metal oxides in molten carbonates can be described by an acid / base concept (Li et al., 1999; Flood and Foerland, 1947). Alkali metal carbonates dissociate following the equilibrium reactions

$$M_2CO_3(l) \rightleftharpoons 2M^+ + CO_3^{2-} \tag{1.6}$$

and

$$CO_3^{2-} \rightleftharpoons O^{2-} + CO_2(g) \tag{1.7}$$

in which CO_3^{2-} is the basic component and CO_2 the acidic component. The gaseous CO_2 is assumed to be in equilibrium with carbonate in the melt (Li et al., 1999). The basicity / acidity of the melt can be defined as a function of $-\log a_{O2-}$ or $-\log p_{CO2}$. Given the oversaturation of CO_2 in the investigated systems, most likely the high partial pressure of CO_2 leads to an acidic dissolution of iron, in which Fe^{2+} can be assumed to be the predominant oxidation state of iron in the carbonate melt, analogous to the reactions formulated for NiO by Orfield and Shores (1989):

$$NiO \rightleftharpoons Ni^{2+} + O^{2-} \tag{1.8}$$

$$NiO + CO_2 \rightleftharpoons Ni^{2+} + CO_3^{2-} \tag{1.9}$$

Due to the open framework structure of carbonate melts, bond length between cations and neighbouring oxygen atoms can be expected to be larger in carbonate melts compared to silicate melts, accompanied by a decrease in bond strength. This was observed for example for REE and alkaline earth elements (Pohlenz et al., 2018).

To investigate the influence of compositional changes on iron isotope fractionation between silicate and carbonate melts, variable starting compositions were employed (see subsection 2.1.2).

These compositions vary in their proportion of network-modifying to network-forming cations and therefore are expected to vary in the degree of polymerization of the silicate

melt. Additionally, in two starting materials an enhanced Ca or Fe content, respectively, was employed to test the influence of a changing concentration of these components on iron isotope fractionation.

To gain insights into $Fe^{3+}/\Sigma Fe$ and the iron coordination environment in the silicate glasses, three selected samples were investigated by Mössbauer spectroscopy (performed by C. McCammon). The quench products of the corresponding carbonate melts did not quench to glasses, due to their low viscosities, lack of melt polymerization, and low activation energies for nucleation in carbonate melts, that facilitate crystallization (Genge et al., 1995a). Hence, the carbonate quench products could not be analyzed by Mössbauer spectroscopy.

1.4 Scope of the thesis

The main objective of my thesis is to improve the understanding on the controls on iron isotope fractionation in carbonatites and other mantle derived rocks. To do so, I focus on the following:

- I experimentally investigate phase stabilities in iron containing carbonatite systems to provide a first insight into iron distribution between carbonate minerals, silicate minerals, iron oxides, and carbonate and silicate liquids. In these experiments I focus on the usability of the run products for iron isotope analyses.

- I address the lack of knowlegde on iron isotope fractionation factors in carbonatite systems required to distinguish kinetic and equilibrium processes. My approach involves experimental determination of iron isotope fractionation factors between immiscible silicate and carbonate melts.

- I analyze inter-mineral iron isotope variabilities on the microscale in a natural mantle-derived melilitite rock sample. Here, my focus is on the iron isotope behavior during interaction of carbonatites with silicates in the mantle at the micro scale environment. My results show significant isotopic variability, measured for the first time in situ in a melilitite rock.

- The new data sets on iron isotope fractionation from the experiments and from the in situ analyses of the melilitite sample are then used to improve current models of carbonatite formation.

Although my experimental approach was successfully applied in the silicate - carbonate melt system, for mineral-melt-systems this was found more challenging. Hence, despite extensive exploration and optimization of experimental techniques during this study,

not all experiments did meet the requirements for isotope analyses (as formulated in subsection 1.3.1 and discussed in subsection 4.1.2). In the following chapters, I will first describe the materials and methods used (chapter 2), then the results of chemical and isotope analyses (chapter 3), followed by the discussion (chapter 4).

2 Materials and Methods

2.1 Experimental setup

The experimental work was organized in three sets of experiments. In the first set, the phase relation experiments, the goal was to find an applicable capsule design and natro-carbonatite systems providing phases suitable for iron isotope analyses. While the desired phase stabilities could be achieved, only the systems producing silicate and carbonate immiscible melts were eligible for iron isotope analyses, since other phases could not be separated satisfyingly. In the second set, the iron isotope equilibration experiments, the focus was on the samples eligible for iron isotope analyses. Various starting compositions were employed to investigate the influence of melt composition on iron isotope fractionation between immiscible carbonate and silicate melts. A third set of kinetic experiments was designed to assess the time scale of isotopic equilibration.

2.1.1 Synthesis of the starting materials of the phase relation experiments and equilibration experiments

In the phase relation experiments and equilibration experiments, mixtures of synthetic carbonate and oxide powders were used to investigate the phase relations in iron bearing natro-carbonatite systems and the iron isotope equilibrium fractionation between carbonate and silicate immiscible melts, respectively.

The starting materials were prepared in batches of 0.5 to 9.0 g, using analytical grade powders of $CaCO_3$, basic $MgCO_3$ (hydromagnesite), Na_2CO_3 (dried at 200 °C), SiO_2 and Al_2O_3 γ-phase (dried at 500 °C). Iron was added in the form of a synthetic hematite powder in shares of 3 to 20 wt % Fe_2O_3. The weighed powder mixtures were homogenized for 15 to 30 min in an agate mortar in ethanol and dried overnight at 100 °C. The starting materials were stored in a desiccator and dried before use at 200 °C to minimize water adsorption. Most of the starting materials were nominally H_2O free, nevertheless minor adsorption of water to the hygroscopic Na_2CO_3 was unavoidable. In Mg-bearing compositions, the use of hydromagnesite added small amounts of H_2O to the starting mixtures (less than 0.2 wt % water, calculated from the stoichiometric formula Vagvoelgyi et al., 2008). In water-bearing experiments, de-ionised H_2O was added to the capsules with a syringe. All compositions are CO_2-saturated at experimental conditions. The advantage of a CO_2-saturated system is that the extent of the two-liquid field is at its maximum, while at CO_2-undersaturated conditions it will vary largely even at small changes in p_{CO2} (Brooker,

1998). Furthermore, the dissolution mechanisms of iron in carbonate melts are sensitive towards small changes in p_{CO2}. CO_2-saturation was reached by the use of carbonate powders as starting materials. The influence of adsorbed N_2 was considered negligible. All starting compositions are presented in Table 2.1 (phase relations, compositions KB designed after Kjarsgaard, 1998, and Brooker and Kjarsgaard, 2011, compositions CaNa free of SiO_2) and Table 2.2 (equilibration experiments, compositions KGW designed after Koster van Groos and Wyllie, 1973, compositions BR and Sp designed after Brooker, 1998).

One aim of the equilibration experiments was to investigate the influence of melt composition on iron isotope fractionation. Therefore, different proportions of network modifying and network forming cations were employed in the starting materials, assuming that the composition of the starting material would be mirrored in the silicate glasses after the experiments. The degree of polymerization was estimated by the aluminum saturation index (ASI = molar $Al_2O_3/CaO + Na_2O + FeO$). At an ASI of 1, all cations are used to charge balance Al^{3+} in tetrahedral positions, while an ASI < 1 indicates an excess of network modifying cations compared to aluminum. ASI values were between 0.03 and 0.14 in the starting materials, resulting in ASI between 0.10 and 0.50 in the silicate glasses. Since the ASI does not take into account variations in silicon concentrations present in the material, the degree of polymerization was estimated additionally by counting the network modifying cations in relation to network forming cations ($n_{mod}/n_{form} = (n_{Ca} + n_{Mg} + n_{Na} + n_{Fe} - n_{Al})/(n_{Si} + n_{Al})$, n = molar concentration). In both ASI and n_{mod}/n_{form} calculations, all iron was counted as network modifier (since experiments were performed under relatively reducing conditions, Fe^{3+} contents were low, see subsection 2.1.5). The influence of CO_2 on polymerization was not accounted for, since it remains unknown. The NBO/T ratio as described in subsection 1.3.2 was not used to estimate the degree of polymerization, since it refers to a homogenous silicate melt network, which might not be present if free ionic carbonate groups are present (details in the discussion section 4.3).

2.1.2 Synthesis of the starting materials for the kinetic experiments

To assess the time scale of iron isotopic equilibration between silicate and carbonate melt, an experimental setup to monitor the kinetics of iron isotope exchange was designed, based on the approach of Schuessler et al., 2007 (further references therein, e. g. Criss et al., 1987; Criss, 1999). In the kinetic experiments a ^{58}Fe enriched glass, representing the silicate melt, equilibrates with a synthetic carbonate and oxide powder of natural iron isotopic composition, resembling in chemical composition the carbonate melt. The addition of ^{58}Fe enhances the equilibrium iron isotopic value of the system three orders of magnitude

($\delta^{58}Fe_{enhanced}$ = 209 ‰) compared to natural systems. Thus, the equilibrium fractionation between carbonate and silicate melt becomes insignificant. Instead, the kinetics of iron isotopic exchange can be monitored as the approach of the artificially enhanced equilibrium isotopic value from two sides becomes visible.

The chemical compositions of the silicate and carbonate component were based on the compositions measured in the run products of the BR-series, i. e. in the silicate glass and the Na-rich carbonate quench phase. For the carbonate endmember mixture a synthetic siderite, which was produced following the protocol of French (1971), was used as iron source. The siderite was checked by XRD analyses for purity, and then mixed and homogenized in an agate mortar with the appropriate carbonate and oxide powders. The silicate endmember mixture was prepared in two steps. First, a glass doped with a ^{58}Fe-enriched tracer (metal powder, obtained from STB Isotope Germany GmbH, enrichment: 99.86 % ^{58}Fe) was prepared. To do so, the ^{58}Fe-enriched metal powder was dissolved in diluted HCl for better handling and added to a mixture of carbonate and oxide powders. This mixture was homogenized in an agate mortar and then fused to a glass by melting in a platinum crucible at 1400 °C for 13 hours, followed by rapid cooling in cold water to quench the melt to a glass. To improve homogeneity the glass was crushed and remelted for 2 hours at 1400 °C. Glass shards were analysed by SEM-EDX and EMPA to ensure sufficient chemical homogeneity (Appendix A). Iron isotope analyses on selected glass pieces were performed to ensure isotopic homogeneity (Appendix B). In a second step, the glass was crushed and ground and Na_2CO_3 was added and homogenized with the ground glass to reach an excess of CO_2 in the bulk composition.

Both compound endmember mixtures were then weighed in the appropriate proportions to represent chemically the starting materials of the BR-equilibration experiments. They were homogenized, dried overnight at 200 °C, and weighed and sealed in capsules for the high-T high-P experiments. The chemical compositions of both the silicate and the carbonate endmember mixtures and of the mixed bulk compositions are presented in Table 2.2. The isotopic starting compositions are given in Appendix B.

TABLE 2.1: Chemical compositions (in wt %) of the KB- and CaNa-series starting materials (phase relation experiments)

	$KB_{2.6}$[a)]	$KB_{5.0}$[a)]	$KB_{10.0}$[a)]	$KB_{17.3}$[a)]	$KB_{20.0}$[a)]	$CaNa_{3.0}$	$CaNa_{5.9}$	$CaNa_{10.0}$	$CaNa_{12.0}$	$CaNa_{24.0}$
SiO_2	5.9	5.7	5.4	5.0	4.8					
Al_2O_3	0.9	0.8	0.8	0.7	0.7					
Fe_2O_3	2.6	5.0	10.0	17.3	20.0	3.0	5.9	10.0	12.0	24.0
MgO	0.3	0.3	0.3	0.3	0.2	0.3	0.3	0.3	0.3	0.3
CaO	40.7	39.8	37.7	34.6	33.5	43.5	42.2	40.4	39.5	34.1
Na_2O	10.2	9.9	9.4	8.6	8.4	10.9	10.6	10.1	9.9	8.5
CO_2	39.4	38.6	36.5	33.5	32.5	42.2	40.9	39.2	38.3	33.1

a) Designed after Kjarsgaard (1998) and Brooker and Kjarsgaard (2011). The water content in all of the samples is below 0.05 wt %.

TABLE 2.2: Chemical compositions (in wt %) of the KGW-, BR-, and Sp-series starting materials (equilibration and kinetic experiments)

	Equilibration experiments					**Kinetic experiments**				
	KGW_{lowAl}[a)]	KGW_{highAl}[a)]	$KGW_{lowAl+Fe}$[a)]	$KGW_{lowAl+Ca}$[a)]	BR[b)]	GL-1	GL-2	Carb	Sp1 57 % GL-1, 43 % Carb	Sp2 57 % GL-2, 43 % Carb
SiO_2	23.4	22.1	22.5	19.5	19.6	44.1	44.2	0.0	19.2	19.1
Al_2O_3	2.8	8.4	2.7	2.3	5.2	10.8	10.9	0.3	4.9	4.9
Fe_2O_3	5.9	5.6	9.9	4.9	12.3	16.3	16.3[c)]	0.0	7.1	7.0
FeO								9.7	5.5	5.5
MgO					1.6	1.1	1.1	1.9	1.5	1.5
CaO	1.6	1.5	1.5	10.7	5.3	2.3	2.3	9.3	6.3	6.3
Na_2O	38.0	35.8	36.4	31.7	29.4	16.2	16.2	37.4	28.2	28.2
H_2O	< 0.05	< 0.05	< 0.05	< 0.05	0.14	< 0.05	< 0.05	< 0.05	< 0.05	< 0.05
CO_2	28.3	26.6	27.1	30.9	26.4	9.1	9.1	41.4	27.4	27.4

a) Designed after Koster van Groos and Wyllie (1973). b) Designed after Brooker (1998). c) including 837 µg ^{58}Fe.

2.1.3 Capsule design and preparation

Gold was chosen as capsule material for experiments below 1025 °C, and platinum for higher temperatures. The inside of the platinum capsules was lined with a rhenium foil (25 µm thickness, Rhenium Alloys Inc.) to prevent iron loss to the platinum, which was crucial for iron isotope analyses. This approach is preferable over graphite capsules, as low viscosity carbonate melts can escape into the porous graphite (Jones et al., 1995; Martin et al., 2013). The use of Pt capsules pre-saturated with Fe was discarded as well, to preclude potential kinetic reactions with an additional iron source. At oxygen fugacities close to the fayalite-magnetite-quartz buffer (FMQ, as given in the experiments, see subsection 2.1.5) rhenium is a convenient container material, due to the low solubility of iron in rhenium and a very slow diffusion rate of iron into rhenium (Borisov and Jones, 1999). This makes the combination of rhenium and platinum a promising capsule design, as shown by Matsukage and Kubo (2003) in peridotite melting experiments. One experimental aim of this study was to transfer the capsule design of Matsukage and Kubo (2003) to the carbonatite system.

Prior to filling and sealing the capsules, gold and platinum tubes (3.0 mm outer diameter, 2.6 mm inner diameter) were annealed at 600 °C for several hours. The rhenium foil was cleaned in ethanol in an ultrasonic bath and then placed inside the platinum tubes (Figure 2.1). The outer platinum capsule was welded shut at one side by arc welding. Starting materials were loaded into the capsule, that was then sealed by welding the other side. Platinum capsules (length 15 mm) contained 30 to 40 mg of starting material, gold capsules (length 20 to 30 mm) contained 90 to 120 mg of starting material.

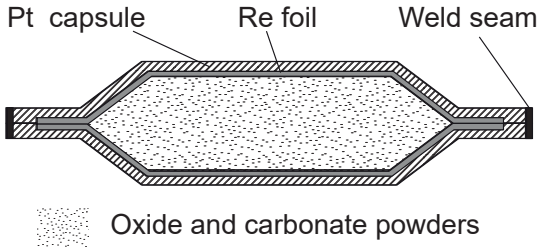

FIGURE 2.1: Capsule design. The rhenium foil prevented reactions between iron and the platinum capsule.

2.1.4 Experimental run conditions

The experiments were run in an internally heated pressure vessel (IHPV) pressurized with argon at pressures of 0.5 and 0.7 GPa, and at temperatures from 900 to 1200 °C, measured with an uncertainty of ± 20 MPa and ± 20 °C, respectively (more technical details

see Borchert et al., 2010). In the large sample holder, up to ten capsules can be run simultaneously. For investigating isotope fractionation factors, another advantage of the IHPV over other autoclaves is the temperature stability throughout the sample holder, which prevents kinetic iron isotope fractionation along a temperature gradient. Run durations were between 2 and 92 hours. At the end of the experiments, the samples were quenched isobarically with an initial cooling rate of 200 °C per minute. Redox conditions of the equlibration experiments are assessed in the following chapter.

One experiment at 0.2 GPa and 750 °C (measured with an uncertainty of ± 5 MPa and ± 10 °C, respectively) was run by H.-P. Nabein in the externally heated cold seal pressure vessel (CSPV). In this setup H_2O was used as pressure medium and the run duration was 68 hours. The samples were quenched with a cooling rate of 200 °C per minute. An overview of the run conditions together with the resulting phases is presented in the result section (subsection 3.1.2, Table 3.2 and Table 3.3).

2.1.5 Oxygen fugacity

All experiments were performed at the intrinsic redox conditions of the IHPV. The intrinsic conditions of the IHPV are transferred to the charge in the capsule via osmotic equilibration in hydrogen partial pressure p_{H2} through the capsule wall (e. g. Chou, 1986). Thus, the oxygen fugacity f_{O2} of the sample charge depends on the fluid composition present in the capsule. Therefore, oxygen fugacities in the capsules of the iron isotope equilibration experiments were approximated with help of the fluid phase, which is assumed to be in chemical equilibrium with both silicate and carbonate melts at run conditions. Additionally, oxygen fugacities were estimated from the $Fe^{3+}/\Sigma Fe$ ratio determined in three silicate glasses by Mössbauer spectroscopy, using the empirical equation of Kress and Carmichael (1991).

While in many geological settings H_2O is the main fluid component and can be used to calculate oxygen fugacities, this does not apply to the carbonate dominated system investigated in this study. Here, CO_2 is the main fluid constituent, while contributions of H_2O, CO, N_2, and Na are considered minor. The exact fluid composition remains unknown due to the formation of thermonatrite ($Na_2CO_3 \cdot H_2O$) quench crystals from the fluid phase upon cooling, changing the composition of the fluid phase by incorporating both CO_2 and H_2O. For simplicity, the influence of H_2O, H_2, carbon species like CO_3^{2-} or CH_4, and other minor fluid components was considered negligible. Accordingly, oxygen fugacities were calculated from the equilibrium reaction

$$2\,CO_2 \rightleftharpoons 2\,CO + O_2 \tag{2.1}$$

as a function of X_{CO2} (with $X_{CO2} = (n_{CO2}/(n_{CO} + n_{CO2}))$ for the P-T-conditions of the time series experiments ($P = 0.7$ GPa, $T = 1200$ °C). For the equilibrium reaction Equation 2.1, the change of the Gibbs free energy G at pressure P and temperature T can be described as

$$\Delta G_{(P,\,T)} = 2\ G_{CO\,(P,\,T)} - G_{O2\,(P,\,T)} - 2\ G_{CO2\,(P,\,T)} \tag{2.2}$$

In equilibrium, $\Delta G_{(\mathrm{P,T})} = 0$. f_{O2} is then related to the Gibbs free energy by

$$RT\ ln f^{0}_{O_2(P,\,T)} = 2\ G^{0}_{CO(P_r,\,T)} + G^{0}_{O_2(P_r,\,T)} - 2\ G^{0}_{CO_2(P_r,\,T)} - RT\ ln\frac{{f^{0}_{CO(P,\,T)}}^{2}}{{f^{0}_{CO_2(P,\,T)}}^{2}} - RT\ ln\frac{(1-X_{CO_2})^2}{{X_{CO_2}}^2} \tag{2.3}$$

in which $f^{0}_{(P,\,T)}$ are the fugacities of the respective pure fluid phase components, and G^{0} the Gibbs free energies of the respective phase components at standard conditions $P_r = 0.1$ MPa and $T_r = 298$ K (e. g. Gottschalk, 1997, and references therein). The Gibbs free energies were calculated using the enthalpy of formation from Holland and Powell (2011), the entropy and heat capacity from Robie et al. (1995), and fugacities of CO and CO_2 derived from Churakov and Gottschalk (2003a,b). Since no graphite was identified in the run products, f_{O2} in the capsule should be above the graphite buffer, which constrains the compositions of the fluid phase to a range of X_{CO2} between 0.81 and 1. These correspond to $\log10\, f_{\mathrm{O2}}/\mathrm{bar}$ between -9.6 and -6.9 (Figure 2.2). The f_{O2} derived from the empirical equation of Kress and Carmichael (1991) for the samples R16-1 ($\log10\, f_{\mathrm{O2}}/\mathrm{bar} = -7.9$) and R15-3 ($\log10\, f_{\mathrm{O2}}/\mathrm{bar} = -9.1$) at 1200 °C fall in this range. Also the $\log10\, f_{\mathrm{O2}}/\mathrm{bar} = -10.6$ at 1100 °C of sample R13-3 fits this range, considering the lower run temperature. Yet, the silicate melt compositions of this study differ drastically from the compositions employed by Kress and Carmichael (1991), most notably in their high alkali content. As Borisov et al. (2017) have shown, this may lead to an overestimation of f_{O2}, since the addition of Na_2O (as well as CaO) increases the $Fe^{3+}/\Sigma\,Fe$ ratio at constant f_{O2}. The experiments of Borisov et al. (2017) are restricted to atmospheric conditions. To estimate the difference in f_{O2}, $Fe^{3+}/\Sigma\,Fe$ at atmospheric conditions were calculated using the empirical equations of Kress and Carmichael (1991) and Borisov et al. (2017), respectively. Then the difference derived at atmospheric conditions was added to the $Fe^{3+}/\Sigma\,Fe$ used to estimate f_{O2} in the empirical equation of Kress and Carmichael (1991). This correction shifts the f_{O2} to slightly lower values in samples R16-1 ($\log10\, f_{\mathrm{O2}}/\mathrm{bar} = -8.2$) and R13-3 ($\log10\, f_{\mathrm{O2}}/\mathrm{bar} = -10.8$). Due to the elevated Al content, balancing the high Na content, the f_{O2} of sample R15-3 remains nearly unaltered ($\log10\, f_{\mathrm{O2}}/\mathrm{bar} = -9.0$).

In Figure 2.3, the estimates of f_{O2} from both the fluid phase and the silicate glasses are compared to the oxygen fugacity buffers Fe_3O_4–Fe_2O_3 (MH), Re–ReO_2 (RRO), and

Fe_2SiO_4–Fe_3O_4 + SiO_2 (FMQ). Estimates of f_{O2} both from the fluid phase and from the silicate glasses are below the value of the RRO buffer. This fits observations from the phase relations experiments. In samples where f_{O2} was elevated by addition of H_2O compared to the equilibration experiments, the Re-foil dissolved and Re oxides were formed.

Redox reactions

Mössbauer spectroscopy data show, that iron in the silicate glasses is in a rather reduced state ($Fe^{3+}/\Sigma Fe$ between 0.24 and 0.12, subsection 3.2.2). Additionally, iron in the carbonate melt is assumed to be mostly Fe^{2+} (see subsection 1.3.2). This means, that Fe_2O_3 from the starting material was reduced significantly. In the equilibration experiments of this study, elements participating in redox reactions are Fe and C from the starting material, Re from the capsule inlay, and H_2. H may enter the capsule in the form of hydromagnesite with the starting materials, from water adsorption to starting powders, and as H_2 permeating through the Pt capsule wall (see Chou, 1986). While CO_2 is assumed to be an excess phase, H_2O and H_2 are present only in small amounts.

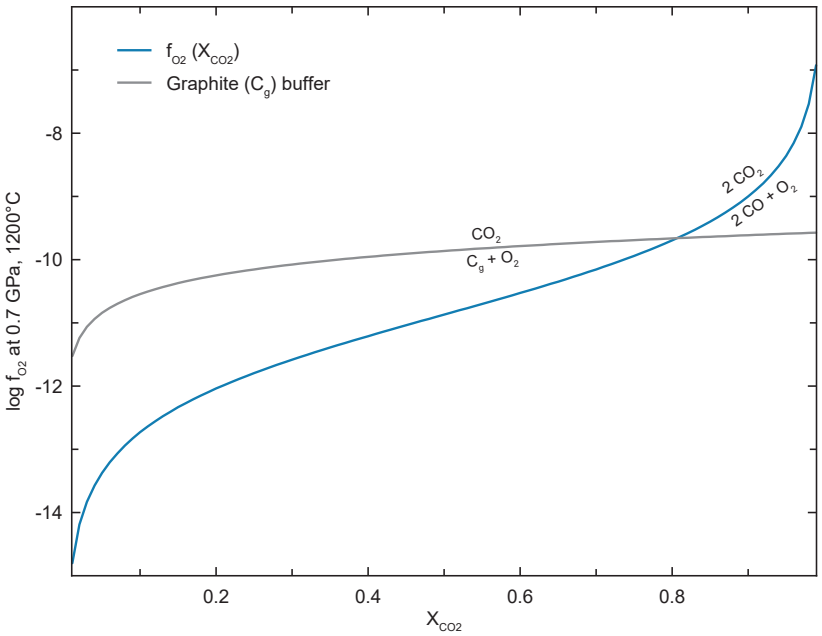

FIGURE 2.2: Oxygen fugacity as a function of fluid composition (X_{CO2}, blue curve) and graphite stability (grey curve; both curves plotted by M. Gottschalk). Since no graphite was identified in the run products, f_{O2} in the capsule should be above the graphite buffer. This constrains the compositions of the fluid phase to a range of X_{CO2} between 0.81 and 1, and the $\log 10\, f_{O2}/\,\mathrm{bar}$ to a range between -9.6 and -6.9.

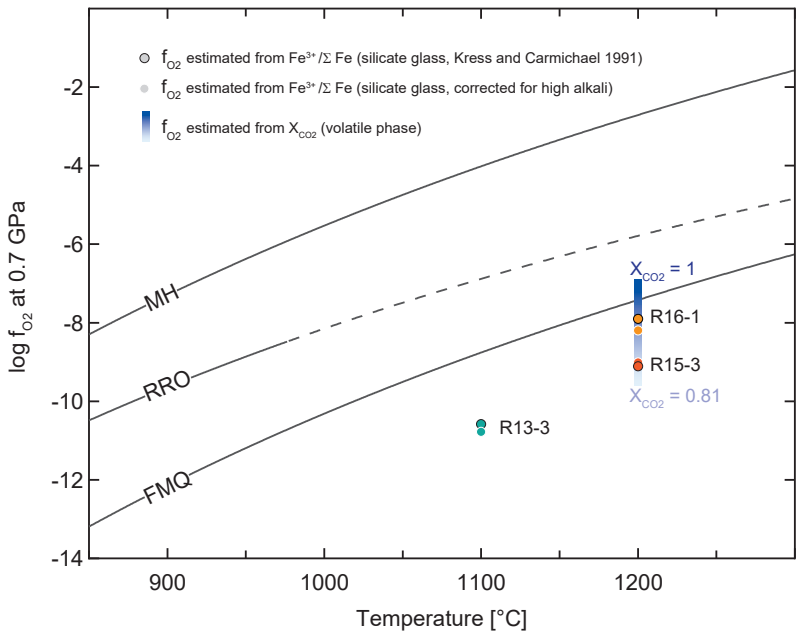

FIGURE 2.3: Estimated oxygen fugacities compared to the oxygen buffers MH, FMQ and RRO. MH and FMQ were calculated from Robie et al. (1995), RRO was calculated from Pownceby and O'Neill (1994). The dotted line represents the extrapolation of the equation of Pownceby and O'Neill (1994) (defined up to 1250 K) to the temperature range of the experiments R13-3, R16-1 and R15-3. The range of f_{O2} calculated from X_{CO2} at 1200 °C (see Figure 2.2) is underlain in blue.

2.1.6 Opening of the capsules and sample preparation

After each run, the recovered capsules were cleaned and checked for leakages by weighing. The capsules were then pierced or cut open and reweighed to estimate the released CO_2 amount. After drying at 100 °C for at least ten minutes, the capsules were weighed again to estimate the water content of the fluid phase, if present. This method provides only a rough estimate of the fluid composition at experimental conditions, since quench phases such as thermonatrite formed upon cooling incorporating H_2O and CO_2. Finally, the solid sample material was recovered for further analyses. In the systems BR, Sp, and KGW which yield two immiscible melts, in some cases the carbonate quench phase was sampled multiple times at different positions in the capsule, to detect possible isotopic heterogeneities within the texturally heterogeneous carbonate quench phase. It was distinguished between the upper part of the carbonate melt, where the carbonate was usually of a lighter color, and the lower part of the carbonate, closer to the silicate glass bead and of a darker color. Due to its higher density, the silicate glass bead was always located at the bottom of the capsules, which were positioned vertically in the autoclave.

For a fast qualitative phase analysis with scanning electron microscopy and energy dispersive X-ray spectroscopy (SEM-EDX), samples from the phase relation experiments were glued on a cylindrical aluminum sample holder with Planocarbon (conductive carbon) or strewn on Plano conductive tabs. Detailed chemical analyses were perfomed only on the experiments selected for iron isotope analyses (systems BR, Sp, and KGW with immiscible silicate and carbonate melts) and on selected samples from the phase relation experiments. Of these samples polished mounts for electron microprobe analyses (wavelength dispersive X-ray spectroscopy, EMP-WDX) and SEM-EDX, respectively, were prepared.

While the silicate glasses could be prepared with a conventional polishing routine for EMP-WDX analyses, the run products of the carbonate melts presented a challenge in the preparation of polished mounts. The carbonate melt, present at run conditions in all samples, quenched to cryptocrystalline, sodium-rich carbonates (in the following called Na-Ca-carb$_{qu}$) upon cooling (subsection 3.1.2). The high sodium content makes this material very soft, hygroscopic, and extremely unstable under an electron beam used for electron microprobe analyses (Brooker and Kjarsgaard, 2011; Martin et al., 2012, I. Veksler, personal communication). Also, the high contrast in hardness compared to other phases occurring in the samples such as magnetite or silicate glass made these samples difficult to polish. A plain surface with a surface roughness of less than 0.25 µm is required for EMP-WDX analyses but could not be obtained. Hence, chemical analyses were done by SEM-EDX, which does not require a highly polished sample surface. Due to the high solubility of the samples not only in water but also in ethanol and isopropanol, a dry

polishing routine was implemented, including several steps of rehardening in epoxy resin under vacuum (Lee and Wyllie, 1997; Martin et al., 2012, and personal communication with D. Schultz, S. Gehrmann, M. Koch-Müller, see Appendix C). After polishing, sample surfaces were still hygroscopic and altered very fast, i. e. within minutes, when exposed to air. Therefore, the polished mounts were stored before analyses at 100 °C, and then transported to the SEM in a portable desiccator. After the analyses, samples were stored in an evacuated desiccator.

To ensure that the rhenium inlay stayed intact and unaltered, SEM-EDX analyses were performed on samples from initial test runs with the rhenium inlay. For this purpose, cross sections were cut from the whole, unopened capsules with a low-speed saw, mounted in epoxy resin, and polished with several steps of rehardening under vacuum in epoxy resin. On cutting the capsules with the saw, large amounts of sample material were lost. To avoid this, some capsules were mounted unopened in epoxy resin and then carefully polished open, with several steps of rehardening under vacuum in epoxy resin.

2.2 Sample description of the melilitite bomb from the SLC group

The natural sample for spatially resolved in situ iron isotope analyses was provided by A. Rocholl. It is a thin section of a melilitite bomb from the Salt Lake Crater group at Honolulu (Oahu, Hawaii, sample B-1/h). The Honolulu Volcanics are a series of small-volume magmas, ranging in composition from alkali basalts to nepheline melilitites. They erupted 0.3 to 0.6 million years ago from small vents scattered across the underlying tholeiitic Koolau shield (Rocholl et al., 1996). The origin of the Honolulu Volcanics is still debated, but they are known for their diversity in mantle derived xenoliths. Rocholl et al. (1996) analysed a series of Honolulu Volcanic samples, ranging from basanitic to melilitic tuffs. In four of the samples they found evidence for the presence of a carbonatite component in mantle depth, such as enrichment in the elements P, Mn, REE, Sr, and Ba. The melilitite bomb B-1/h is one of these samples and consists mainly of olivine (grainsizes from 0.2 to 1.5 mm), magnetite (grainsizes up to 0.2 mm), and melilite (up to 0.4 mm lenght and 0.05 mm width) in a fine-grained melilite groundmass.

2.2.1 Olivine

All olivines are inclusion rich and have rims that are altered to monticellite (Figure 2.4). Nevertheless, the olivine grains can be seperated into at least two groups, according to their grain size and habit. One group has diameters of ≥ 0.5 mm and is characterized by a rather prismatic to skeletal habit. These grains are eu- to subhedral, but have altered rims.

The other group features diameters < 0.5 mm, and appears to be of acicular habit. These crystals are sub- to anhedral and appear rounded due to the altered rims. Many olivines of both the larger and the smaller group have reverse and oscillatory Fe-Mg zoning.

2.2.2 Magnetite

Most magnetite grains are eu- to subhedral. Some have cores that appear dark in reflected light (Figure 2.4). These cores are enriched in chromium and aluminum, while the rims are enriched in iron and titanium (personal communication A. Rocholl).

2.2.3 Possible steps of magma evolution

The petrographic observations named above can be explained by the following steps of magma evolution:

- The Fe-Mg zoning in olivine may result from crystal growth in an evolving melt, or from a chemical exchange between crystal and a changing melt, e. g. during magma mixing, or result from a combination of both.
- The two groups of olivine may represent two different populations of olivine, which would be another indicator of magma mixing.
- The altered rims of the olivine grains also point to a magma mixing event, possibly with a carbonatite magma. Since all olivine grains are altered to monticellite, this would be the most recent event.

The hypothesis of magma mixing with a carbonatite magma is also supported by the observations in magnetite. While the Cr- and Al-rich cores in some magnetites point to a mantle origin, the Fe- and Ti-rich rims may have formed in contact with a carbonatite magma, either by crystal growth or by chemical interdiffusion of the respective elements. To cause these changes, the possible carbonatite magma had to be Ca-rich (to enable the growth of monticellite) and at least Fe-bearing (if not Fe-rich) to enrich Fe in the magnetite grains.

To investigate, whether the influence of the three mentioned events is visible in the iron isotope composition, the iron isotope ratios of magnetite and olivine grains were analysed by in situ by femtosecond laser ablation coupled to MC-ICP-MS (subsection 2.3.5). Phases not eligible for UV-fs laser ablation (melilite, melilite groundmass) were not analysed.

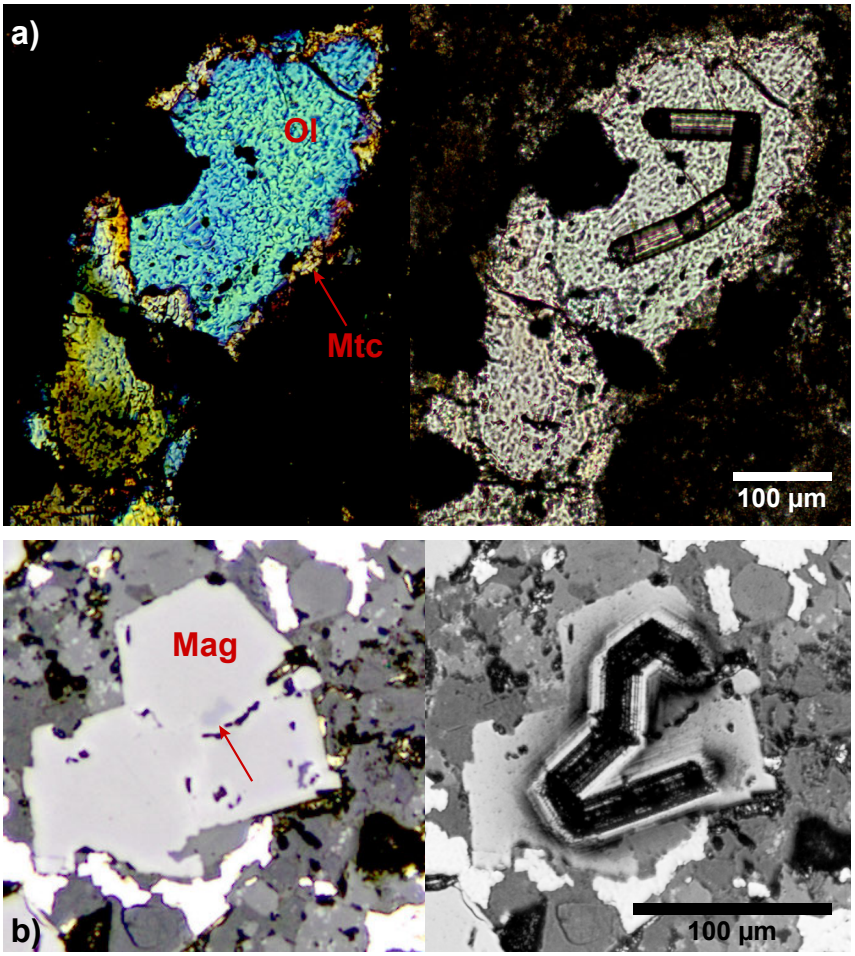

FIGURE 2.4: Photographs of olivine (a, transmitted light, left: crossed-polarized) and magnetite crystals (b, reflected light) before and after laserablation. The olivine rims are altered to monticellite (arrow in a), potentially by interaction with a carbonatite fluid. A few magnetites have darker cores (arrow in b) with high Cr and Al. The laser ablation paths were programmed for each grain individually to avoid cracks and inclusions.

2.3 Analytical Methods

In the following chapter, the analytical methods applied to characterize the sample material are described. Phase analyses were performed on the run products of all experiments (phase relation, isotope equilibration, and kinetic experiments). In the investigation of the phase relation experiments, the focus was on whether or not the samples were eligible for iron isotope analyses, therefore some of these samples were scanned only roughly for their mineral composition. Only the samples used for iron isotope analyses were characterized in detail regarding their chemical composition. The presence of Na-Ca-carb$_{qu}$ in most experimental run products hampered the use of standard methods, as addressed below. All analyses were done at the Helmoltz-Zentrum Potsdam (Deutsches GeoForschungsZentrum, GFZ), if not mentioned otherwise.

2.3.1 Phase analyses

Mineral identification by powder X-ray diffraction

Powder XRD was used to identify crystalline phases in the phase relation experiments. An aliquot of each sample was ground and glued between two Mylar boPET (biaxially-oriented polyethylene terephthalate) foils for transmission XRD analyses. The diffraction patterns were recorded by H.-P. Nabein with a STOE Stadi P diffractometer, equipped with a Germanium (111) primary monochromator and a position sensitive detector, using Cu-K$_{\alpha 1}$ radiation, an acceleration voltage of 40 kV, and a tube current of 40 mA. Qualitative phase analyses were done with the PANanlytical X-pert HighScore Plus software. Due to the high content of Na-Ca-carbonates in all samples, concentrations of accessory minerals were often below the detection limit of approximately 3 wt %. Therefore, also SEM imaging and EDX analyses were used to detect and identify accessory minerals (subsection 2.3.2).

Textures in the carbonate phases

Powder XRD does not provide means to distinguish solid carbonate phases stable at run conditions from carbonate quench phases. Instead, this was achieved by interpreting the textures of the carbonate phases in BSE images. The interpretation of the observed textures was sometimes ambiguous, though. This is due to the occurrence of round pure $CaCO_3$ phases with a liquid-like texture (s. Figure 2.5, after Brooker and Kjarsgaard, 2011). As Brooker and Kjarsgaard (2011) summarized, previous studies suggested two interpretations, 1) a solid phase at run conditions or 2) an immiscible, pure $CaCO_3$ liquid. Brooker and Kjarsgaard (2011) interpreted the round $CaCO_3$ as solid calcite, based on a careful

re-examination of the two-liquids ± calcite phase equilibria. Following their description, one indication for calcite is its pure $CaCO_3$ chemistry. A dendritic to laminar texture on the other hand points to a fast exsolution of two liquids during quench. Still, in some run products, small round $CaCO_3$ phases align to form a texture very similar to a dendritic pattern (s. Figure 2.5, Figure 3.2, Figure 3.3, and sample descriptions in subsection 3.1.2).

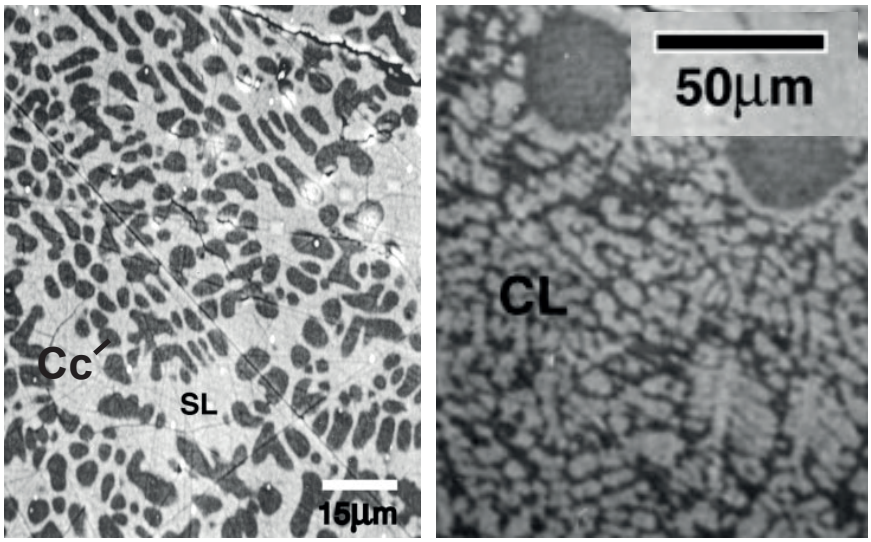

FIGURE 2.5: Figures from Brooker and Kjarsgaard (2011, Figures. 1c and 3b): BSE images of round calcite textures in the left image (dark gray = solid calcite, Cc, light gray = in silicate melt, SL) and on the right hand a dendritic exsolution texture in a carbonate melt (CL), that formed during the quench.

2.3.2 Chemical analyses of the run products

Chemical analyses of the run products were done by scanning electron microscopy combined with energy dispersive X-ray spectroscopy (SEM-EDX), electron microprobe analyses, employing wavelength dispersive spectroscopy (EMP-WDX), and inductively coupled plasma optical emission spectroscopy (ICP-OES). Due to the properties of the sample materials, each of these methods has its advantages and drawbacks. These are summerized in Table 2.3. The resulting uncertainties in bulk composition of the run products are addressed below in subsubsection 2.3.2.

Scanning electron microscopy and EDX spectroscopy

SEM-EDX analyses were done on all samples of the phase relation, isotope equilibration, and kinetic experiments to identify phases and determine their chemical compositions. The prepared samples were coated with carbon and analysed with a Jeol JSM-6510 SEM

TABLE 2.3: Advantages and drawbacks of the analytical methods

Phase	Element	Method SEM-EDX	Method EMP-WDX	Method ICP-OES
Silicate melt	Si	✓	✓	Evaporates during HF-digestion
	Al	✓	✓	✓
	Fe	✓	✓	✓
	Mg	✓	✓	✓
	Ca	✓	✓	✓
	Na	Unstable in the electron beam, this necessitates short measurement times	Unstable in the electron beam, this necessitates short measurement times	✓
	H_2O	-	Adsorbs on highly hygroscopic sample material	Adsorbs on highly hygroscopic sample material
	CO_2	-	Due to water adsorption, CO2 can not be estimated from missing totals	Due to water adsorption, CO2 can not be estimated from missing totals
Carbonate melt	Si	Fine dispersed sil. melt droplets (s. Table 3.1) cannot be analyzed seperately		Evaporates during HF-digestion
	Al	Very low content, often below detection limit	Sample preparation not possible (s. subsection 2.1.6)	Al could be used for maximum estimate of contamination of seperated phase with sil. melt
	Fe	✓		✓
	Mg	✓		✓
	Ca	✓		✓
	Na	The short dwell time of the rastering beam helps to prevent loss of unstable Na		✓
	H_2O	Adsorbs on highly hygroscopic sample material		Adsorbs on highly hygroscopic sample material
	CO_2	-		Due to water adsorption, CO2 can not be estimated from missing totals

equipped with an Oxford Instruments INCA X-act detector at the University of Potsdam, supervised by C. Günther. EDX spectra were collected using an accelerating voltage of 15 kV. To minimize evaporation of sodium a short acquisition time of 20 seconds was used while scanning areas of a minimum of 100 μm^2 on silicate glasses, as suggested by Brooker and Kjarsgaard (2011). The Na-Ca-$carb_{qu}$ phases usually showed dendritic exsolution textures, so larger areas of several 100s of μm^2 across all textures were scanned to estimate the original carbonate melt composition. Silicate minerals in the phase relation experiments (KB-series) were analyzed by spot analyses, which were sufficient to identify the mineral phases in most cases.

In the Na-Ca-$carb_{qu}$ phases that crystallized from the carbonate melt upon cooling, sodium is very loosely bound and volatile in an electron beam. In the analysis of Na-Ca-$carb_{qu}$, SEM combined with an EDX detector has an advantage over EMP-WDX, since the short dwell time of the rastering beam of the SEM helps to prevent loss of sodium and a high beam damage on the sample, as observed in EMP-WDX analyses. Yet, compared to ICP-OES analyses, sodium is still systematically underestimated by SEM-EDX analyses. A disadvantage of SEM-EDX lies in the carbon coating of the samples, which prevents a direct measurement of the CO_2 content of silicate glasses and Na-Ca-$carb_{qu}$. Instead, CO_2 contents of the Na-Ca-carbonate quench phases were calculated as stoichiometric carbonate for all Fe-, Mg-, Ca- and Na-cations. The CO_2 content of the silicate glasses could not be estimated by EDX analyses. Furthermore, EDX analyses of the Na-Ca-$carb_{qu}$ systematically displayed the local heterogeneities of the quench textures.

Electron microprobe analyses (WDX spectroscopy)

EMP-WDX analyses were performed to determine the chemical composition of the silicate glasses of iron isotope equilibration experiments and of selected magnetite and calcite minerals from the phase relation experiments. The Na-Ca-$carb_{qu}$ phases were not stable in the EMP electron beam. The analyses were done with a JeolSuperprobe JXA-8230 and a JeolHyperprobe JXA-8500F, with five wavelength dispersive spectrometers each, using an accelerating voltage of 15 kV and a beam current of 5 nA. Both instruments were operated by O. Appelt. The standards used were tugtupite (Si, Na, Al), hematite (Fe), diopside (Ca), and periclase (Mg). Due to the high sodium content in the silicate glasses analyses were performed using large beam diameters of 10 to 15 µm and a short acquisition time of 5 seconds per spot.

The analytical data quality in the silicate glasses is limited by the large number of pores in the glasses that inevitably intersected with the beam. The CO_2 content could not be measured, but was estimated for the silicate glases as difference to 100 % total, after recalculating all FeO as Fe_2O_3, and adding contaminations of rhenium as detected with ICP-OES. The CO_2 content of calcite was calculated stoichiometrically.

Optical emission spectrometry (ICP-OES)

All samples of the isotope equilibration experiments (Na-Ca-carb$_{qu}$ phases and silicate glasses) were brought in solution (see below) and then analysed with an axial ICP-OES Varian 720-ES to determine their chemical bulk composition. The instrument was calibrated using 10 multi-element ICP standard solutions in 0.3 M HNO_3 matrix with concentrations of iron and most other elements ranging from 5 ppb to 10 ppm and rhenium concentrations ranging from 5 ppb to 1 ppm, measured with an uncertainty of < 5 %.

To avoid loss of material and to minimize the risk of contamination of the small sized samples (0.3 to 10 mg), samples have not been dried before weighing. All H_2O, CO_2 and SiO_2 were lost during the HF digestion and could not be measured. Missing totals comprise not only H_2O, CO_2 and SiO_2 from the sample material but also adsorbed water. After recalculating CO_2 and SiO_2 contents as described below, the calculated totals were between 80 and 120 % for most samples.

The CO_2 content of the Na-Ca-carb$_{qu}$ phases was recalculated as stoichiometric carbonate for all Fe-, Mg-, Ca- and Na-cations. The CO_2 content of the silicate glasses could not be estimated from ICP-OES measurements. The SiO_2 content of the Na-Ca-carb$_{qu}$ of the BR-series was estimated using the Al concentration measured with ICP-OES in the Na-Ca-carb$_{qu}$. From the Al concentrations, SiO_2 was recalculated using the Si/Al ratios determined with SEM-EDX analyses of the Na-Ca-carb$_{qu}$. In the Na-Ca-carb$_{qu}$ samples of the KGW-series, Al contents were below the detection limit of the EDX detector. Therefore the Si/Al ratios of the silicate glasses as determined with SEM-EDX or EMP analyses were used for recalculations. The SiO_2 content of the silicate glasses was recalculated from the Si/Fe ratios obtained in EDX or WDX analyses. The possibility, that Si and Al in the Na-Ca-carb$_{qu}$ are contaminants from the silicate melt is addressed below (subsection 2.3.4).

Uncertainty of the combined chemical analyses

In subsection 3.2.1, the results of all three methods are presented. ICP-OES and EMP-WDX analyses usually agreed within 10 % on oxide content of the silicate glasses, except for CaO, which was systematically overestimated with ICP-OES analyses, probably due to matrix effects. The SEM-EDX data of the Na-Ca-carb$_{qu}$ phase are of higher variability compared to ICP-OES data, since SEM-EDX data reflect the local inhomogeneities of the Na-Ca-carb$_{qu}$. In the further evaluation of the data in the result and discussion section, the ICP-OES analyses are used, corrected for the missed out elements, as described above. From the ICP-OES analyses of the run products, the original bulk composition of each capsule was recalculated, adding in CO_2 of the volatile phase as estimated from weighting at the capsule opening. In the recalculations, the ratios of silicate melt : carbonate melt

were determined iteratively. The recalculated bulk compositions for each capsule were then accurate within 3 wt % (oxides) of the original composition for each element, except for Na_2O, FeO, and CO_2 which were accurate within 5 wt % (Na_2O and FeO) and 10 wt % (CO_2).

2.3.3 Iron oxidation state

To be able to interpret the observed iron isotope fractionation, it is crucial to know the iron oxidation state (in the following described as $Fe^{3+}/\Sigma Fe$) in both silicate and carbonate melt, but at the same time this was difficult to obtain. The $Fe^{3+}/\Sigma Fe$ of the silicate melt was assessed by Mössbauer spectroscopy on three compositionally different silicate glasses. This method could not be applied to the cryptocrystalline Na-Ca-$carb_{qu}$ phases representing the carbonate melt. The wet chemistry colorimetric method as described in Schuessler et al. (2008) could not be used to detemine $Fe^{3+}/\Sigma Fe$. The method utilizes a reversible reaction, in which vanadium is reduced by Fe^{2+} during sample dissolution and thus "memorizes" the amount of Fe^{2+}. This reaction would be disturbed by the presence of any other multivalent element. Due to the rhenium content detected in the Na-Ca-$carb_{qu}$ phases, wet chemistry analyses of the carbonate phases were discarded.

Mössbauer spectroscopy

Mössbauer analyses as well as data evaluation and interpretation were done by C. McCammon (Bavarian Research Institute of Experimental Geochemistry and Geophysics, BGI). To determine the $Fe^{3+}/\Sigma Fe$ of three compositionally different silicate glasses, Mössbauer analyses were performed on glass shards of the samples R13-3 (composition $KGW_{low\,Al}$), R15-3 (composition $KGW_{high\,Al}$), and R16-1 (composition BR). ^{57}Fe Mössbauer spectra were recorded at room temperature in transmission mode on a constant acceleration Mössbauer spectrometer with a nominal 370 MBq ^{57}Co point source in a 12 µm Rh matrix. The velocity scale of the spectra was calibrated relative to α-Fe. Line widths of 0.36 mm/s were obtained for outer lines of α-Fe at room temperature. The collection of the spectra took 1 to 2 days for each sample. The spectra were fitted using the MossA software (Prescher et al., 2012) and the extended Voigt-based fitting model (xVBF, Alberto et al., 1996; Lagarec and Rancourt, 1997). $Fe^{3+}/\Sigma Fe$ was determined from relative areas.

2.3.4 Iron isotope analyses by solution MC-ICP-MS

Work in the cleanlab as well as measurements with the MC-ICP-MS in solution and coupled with UV fs laser ablation was supervised by J. A. Schuessler and technically supported by J. Schlegel and J. Buhk.

Only experiments that produced immiscible carbonate and silicate melts were used for iron isotope analyses (details see below in subsection 4.1.2).

Phase separation

Prior to sample digestion the silicate glasses were separated from the Na-Ca-carb$_{qu}$ phases by physical separation of the two phases: Each experiment contained a silicate glass bead that could easily be separated from the carbonate phase due to the sharp meniscus between the two phases. In one sample (BR-series, sample R07-1) silicate and carbonate melts were seperated by leaching, using modified dissolution steps as described by von Blanckenburg et al. (2008) and Johnson et al. (2010). The results were in perfect agreement with the results for physically separated samples. Secondary electron (SE) and backscattered electron (BSE) imaging showed no carbonate inclusions in the silicate glass, so it was assumed that the glass shards picked for iron isotope analyses represent the pure silicate phase. The Na-Ca-carb$_{qu}$ phases usually contained spheres of silicate glass that were too small to be separated physically by hand picking. Spheres < 15 µm can be interpreted as exsolutions from the carbonate melt during quenching (Brooker and Kjarsgaard, 2011). In this case the glass spheres should be included in the analyses of the Na-Ca-carb$_{qu}$ phase to obtain the bulk chemical and isotopic composition of the carbonate melt at experimental conditions. On the other hand, at least the larger silicate spheres can be interpreted as parts of the silicate melt that did not join with the main bead (Brooker and Kjarsgaard, 2011). To estimate the quality of the phase separation the amount of iron derived from such a contamination of the Na-Ca-carb$_{qu}$ phases by silicate melt droplets was calculated. To do so, aluminum was used as an indicator, assuming that all aluminum measured with ICP-OES in the Na-Ca-carb$_{qu}$ phase originated from the silicate phase. For samples of the BR-series, the estimated purity of the Na-Ca-carb$_{qu}$ phase is between 90 and 95 % , which would lead to an underestimation of the fractionation factor by 0.01 ‰. This is well below the Fe isotope analytical uncertainty (0.05 ‰). For samples of the KGW-series an even higher purity of 97 to 99 % was estimated.

Sample digestion and iron purification

The separated samples were weighed into 7 ml Savillex® PFA beakers. Sample weights of 0.3 to 10 mg were digested in HF and HNO_3 at 145 °C. Then iron was purified from matrix elements by anion-exchange chromatography as described in Schoenberg and von Blanckenburg (2005), using 1 mL of Dowex® 1-X8 anion resin. In some samples, rhenium from the capsule inlay had migrated into the melts, preferably into the carbonate melt, and could not be completely removed by chromatography. For these samples a purification step was added, in which iron was quantitatively precipitated with ammonia, and rhenium was

removed together with the supernate (as described in Schoenberg and von Blanckenburg, 2005) to achieve a ratio of Re/Fe < 0.01 in all samples. MC-ICP-MS measurements of iron isotope ratios on test solutions of IRMM-014 doped with Re show that a ratio of Re/Fe < 0.03 is necessary to avoid matrix effects, which would lead to a shift of δ^{56}Fe towards more negative values. ICP-OES analyses before and after the column chemistry or the precipitation step, respectively, ensured the quantitative recovery of iron and sufficient purity of the solution before MC-ICP-MS measurements.

Mass spectrometry

All samples were measured with a MC-ICP-MS (Thermo Scientifc Neptune) following the method described by Schoenberg and von Blanckenburg (2005). The uncertainty (long-term reproducibility) of this method, including sample digestion and iron purification, is 0.05 ‰ (2 standard deviation, 2SD) on δ^{56}Fe and 0.07 ‰ (2SD) on δ^{57}Fe (Schoenberg and von Blanckenburg, 2005). The instrumental setup is described in detail in Schuessler et al. (2016). Operating parameters during the solution measurements are documented in Table 2.4. Gas flows and ion-optical lenses were tuned to optimum conditions before each measurement session. The samples were introduced into the system in concentrations of 3 to 5 ppm Fe in 0.3 M HNO_3, resulting in intensities on ^{56}Fe of 11 to 19 V (10^{11} Ohm amplifier). Sample-standard bracketing with the international isotope measurement standard IRMM-014 was used to correct for instrumental mass bias. With every batch of unknown samples two international reference materials (BHVO-2, basalt; COQ-1, carbonatite) were processed and measured to verify accuracy and the repeatabilityof the method. The results of reference materials measurements are: δ^{56}Fe (BHVO-2) = 0.11 ‰ ± 0.05 (2SD, $n_{procedure}$ = 7) and δ^{56}Fe (COQ-1) = −0.05 ‰ ± 0.04 (2SD, $n_{procedure}$ = 7), which agree with values measured in other laboratories (see GeoReM Database, Jochum et al., 2005). Additionally, the instrumental precision and accuracy were evaluated in each measurement session by analyses of an internal laboratory standard HanFe (pure Fe solution). The measurements of δ^{56}Fe (HanFe) = 0.29 ‰ ± 0.05 (2SD, $n_{replicates}$ = 117) are in excellent agreement with previous analyses in other laboratories (e. g. Moeller et al., 2014). In every analytical session 2 to 4 replicates of each sample were measured. Total procedural blanks contained less than 36 ng iron, which is 3 orders of magnitude less than iron processed from samples and is therefore considered negligible.

The analytical uncertainty of the method (0.05 ‰, 2SD) represents the long term reproducibility of iron isotope analyses, including all steps from sample digestion to the actual MC-ICP-MS measurement, but does not assess the repeatability of the experimental work. This was evaluated by calculating the mean $\Delta^{56}Fe_{sil.\,m.\text{-}carb.\,m.}$ from experiments of the same pressure and temperature conditions (1200 °C and 0.7 GPa). The standard deviation of the sample from the mean $\Delta^{56}Fe_{sil.\,m.\text{-}carb.\,m.}$ in each system contains information about the

repeatability of the whole experimental procedure, from filling starting materials into the capsules, running the experiments in the IHPV, opening of the capsules and phase separation, to sample digestion and iron purification in the clean lab. This repeatability of the complete experimental procedure is 0.04 ‰ (2SD, $n_{exp.}$ = 3) in the BR-system, 0.08 ‰ (2SD, $n_{exp.}$ = 3) in the $KGW_{high\ Al}$-system, and 0.09 ‰ (2SD, $n_{exp.}$ = 5) in the Sp-system. In each of the systems $KGW_{low\ Al}$, $KGW_{low\ Al+Fe}$, and $KGW_{low\ Al+Ca}$ only two experimental runs could be repeated at the same $P-T$-conditions.

TABLE 2.4: Operating parameters of the MC-ICP-MS (solution measurements)

MC-ICP-MS	Thermo Scientific Neptune
Cool gas (Ar) [L min^{-1}]	15.00
Auxiliary gas (Ar) [L min^{-1}]	0.65 – 0.70
Nebuliser gas (Ar) [L min^{-1}]	0.605 – 0.618
RF generator power [W]	1200
Accerlation voltage [V]	– 10 000
Extraction [V]	– 2000
Focus [V]	– 740 to – 625
Cones	Ni: N-type sampler and H-type skimmer
Mass resolution [m/Δm]	> 6400
Amplifiers [Ω]	10^{11}
Faraday cup setup: ^{52}Cr (L4), ^{54}Fe (L2), ^{56}Fe (C), ^{57}Fe (H1), ^{58}Fe (H2), ^{60}Ni (H4)	

2.3.5 Iron isotope analyses by UV femtosecond laser ablation coupled to MC-ICP-MS

Iron isotope compositions of magnetite and olivine grains in the melilitite bomb were determined with a MC-ICP-MS (Thermo Scientific Neptune) coupled to an in-house built UV femtosecond laser ablation (fs LA) system. Using the sample-standard-bracketing method developed by Horn et al. (2006), this setup allows a high spatial resolution analysis of iron isotopes with minimized artifical isotope and elemental fractionation. The matrix independency of the UV fs laser ablation method on olivine and magnetite has been demonstrated by Steinhoefel et al. (2009).

The laser ablation system (GFZ fem^2, described in detail in Schuessler and von Blanckenburg, 2014) is based on a Ti:sapphire regenerative amplifier system (Spectra Physics Solstice) with a fundamental wavelenght of 785 nm that is converted to the deep UV wavelenght of 196 nm by nonlinear optics. Operating parameters of the laser ablation system and the coupled MC-ICP-MS are given in Table 2.5. The thin section was placed

in a He-flushed ablation cell together with the international isotope measurement standard IRMM-014 as bracketing standard and reference materials, both in polished epoxy mounts. The sample-standard-bracketing corrects for instrumental drift and mass bias. Focusing the laser beam below the sample surface produced spotsizes between 25 and 33 µm with resulting energy densities between 0.4 and 0.8 J/cm^2. An Olympus BX-61 microscope connected to a custom-designed software was used to adjust ablation paths on mineral grains induvidually to avoid the ablation of mineral inclusions and cracks in the sample. Standard and reference materials were ablated in rasters. Depending on the iron content and ablation behavior of the material, laser pulse repetition rates were set between 5 and 200 Hz to match signal intensities between samples and bracketing standard (Table 2.6). The background signal on ^{56}Fe was between 1 and 4 mV.

The standard integration time of the signal was 100 seconds (50 cycles á 2 seconds). On some grains ablation paths were extremely short due to the small grainsizes, which left significantly less cycles (<30) for evaluation and led to high uncertainties. Each ablation of sample or bracketing standard was followed by 60 cycles used for washout of the signal and consequent background gas blank measurement. Background contributions to the total signals of ^{54}Fe, ^{56}Fe, and ^{57}Fe were <0.3 %. The reported isotope ratios were blank corrected. For each measurement, the time resolved signals were checked individually for a gaussian normal-distribution and significant variations, outliers >2 standard deviation were elimited.

The mineral grains were measured in three different sessions in which mass resolutions >7600 (m/Δm, where m is the mass of the ion of interest and Δm the difference between its 5 and 95 % peak hight) were reached. These were sufficient to resolve molecular interferences (^{40}Ar^{16}O, ^{40}Ar^{17}O, ^{40}Ar^{18}O) on ^{56}Fe, ^{57}Fe and ^{58}Fe. The signals of ^{52}Cr and ^{60}Ni were measured simultaneously to estimate the extent of isotobaric interferences of ^{54}Cr on ^{54}Fe and ^{58}Ni on ^{58}Fe. Where chromium contents were high in olivine and magnetite grains (^{54}Cr/^{54}Fe ratio >0.0001, Steinhoefel et al., 2009), $\delta^{56/54}$Fe values were calculated from $\delta^{57/56}$Fe as

$$\delta^{56/54}\mathrm{Fe}_{\mathrm{calculated}} = 1.99 * \delta^{57/56}\mathrm{Fe}_{\mathrm{measured}}$$

which is a linear approximation (valid over small ranges in isotopic composition) of the mass-depenent fractionation law (Johnson et al., 2004):

$$\delta^{56/54}\mathrm{Fe} = (m_{56} - m_{54})/(m_{57} - m_{56}) * \delta^{57/56}\mathrm{Fe}.$$

The reported uncertainties are error propagations from the internal standard error of the mean at 95 % confidence level of the measured isotope ratios of the individual measurements. Uncertainties of the calculated $\delta^{56/54}$Fe are the scaled uncertainties of the $\delta^{57/56}$Fe using the same factor (1.99) as for calculating the $\delta^{56/54}$Fe. The long-term repeatability of the method, based on the analyses of various reference materials over one year, is ± 0.10 ‰

(2 SD) in $\delta^{56/54}$Fe and $\pm 0.20\,‰$ (2 SD) in $\delta^{57/54}$Fe (Steinhoefel et al., 2009; Horn et al., 2006; Dziony et al., 2014).

In the analyses, uncertainties as low as 0.10 ‰ (2 SD) are reached only in the first analytical session. In the second session (LA-4), low signal-to-background ratios ($< 10^3$ on ^{57}Fe) caused a loss of accuracy. In the third session LA-5, signal intensities on ^{56}Fe were quite low (6-8 V). This was due to small spot sizes (23 µm) required to fit the small remaining magnetites and a low laser power. Furthermore, some ablation paths on both olivine and magnetite grains were extremely short, which reduced the number of cycles left for evaluation and thus the precision. The reason for the short ablation paths were numerous mineral inclusions and cracks. The data eligible for further evaluation were further reduced by mineral inclusions hidden below the surface that were hit during ablation. Also laser paths at mineral rim zones sometimes cut too deep and hit the material underlaying the olivine.

In each session, at least one reference material was analysed repeatedly to assess accuracy and precision. Iron isotopic composition of these reference materials were obtained independently by solution MC-ICP-MS. Used as reference materials were an iron rod (Puratronic®, 99.995 % Fe, AlfaAesar Johnson Matthew Company, Lot Number: H24U033), a pure magnetite (CM b), and the international reference material BHVO-2g (Basalt glas, United States Geological Survey). The results of the measurements on reference materials are presented in Table 2.7. Data are reported together with the error propagation on the $\delta^{56/54}$Fe, calculated from the internal standard errors of the mean at 95 % confidence level ($2SE = t * \frac{SD}{\sqrt{n}}$, with SD = standard deviation and t derived from student-t distribution at 95 % confidence) of the iron isotope ratio measurements. The uncertainties of the calculated $\delta^{56/54}$Fe are the measurement uncertainties of the $\delta^{57/56}$Fe scaled with the factor of 1.99 used for calculating the $\delta^{56/54}$Fe.

TABLE 2.5: Operating parameters of the MC-ICP-MS and the fs LA system

MC-ICP-MS	Thermo Scientific Neptune
Cool gas (Ar) [L min^{-1}]	15.00
Auxiliary gas (Ar) [L min^{-1}]	0.70 – 0.73
Nebuliser gas (Ar) [L min^{-1}]	0.605 – 0.618
LA carrier gas (He) [L min^{-1}]	1.20 – 1.23
RF generator power [W]	1200
Accerlation voltage [V]	– 10 000
Extraction [V]	– 2000
Focus [V]	– 689 to – 541
Cones	Ni: N-type sampler and X-type skimmer
Mass resolution [m/Δm]	> 7500
Amplifiers [Ω]	10^{11}
Faraday cup setup: ^{52}Cr (L4), ^{54}Fe (L2), ^{56}Fe (C), ^{57}Fe (H1), ^{58}Fe (H2), ^{60}Ni (H4)	
LA system	GFZ Fem^2
Cycle interagtion time [s]	2
Number of cycles on IRMM-014[a]	40 – 50
Wavelength [nm]	193
Pulse width [fs]	< 200
Laser energy at sample [J cm^{-2}]	0.4 – 0.8
Spot diameter [µm]	25 – 33
Scan speed [µm s^{-1}]	40
Ablation mode	Raster/Individual paths

[a] Number of cycles on olivine and magnetite grains vary and are given with the results in Table 3.14, section 3.4

TABLE 2.6: Repetition rates and measured intensities on samples and reference materials

Sample	IRMM-014 / Puratronic			BHVO		CMb		Olivine		Magnetite	
	LA3	LA4	LA5	LA3	LA4	LA3	LA5	LA3	LA4	LA3	LA5
Repetition rate [Hz]	9.5	5	9	200	166	11.5	13	100	77	22.2	22.0
^{56}Fe intensity [V]	12-19	10	6-8	12-21	11	14-15	6-7	8-15	11-17	17-24	6-8

TABLE 2.7: Results of fs-LA measurements on reference materials

	Puratronic			CM b			BHVO-2g		
	δ^{56}Fe (meas.) [‰]	2SD	n	δ^{56}Fe (meas.) [‰]	2SD	n	δ^{56}Fe (calc.) [‰]	2SD	n
LA-3	0.26	0.08	6	0.95	0.09	3	0.25 ($\pm$0.12, 2SE)		1
LA-4	0.30	0.02	4			-	0.12	0.22	10
LA-5	0.22	0.16	12	1.12	0.27	5			-
Solution MC-ICP-MS	0.20	0.07	14	0.99[1]	0.07	4	0.11	0.02	4

[1] Measured by J. A. Schuessler, personal communication

3 Results

In this chapter, first the results of the phase relation experiments are presented (section 3.1), starting with an evaluation of the experimental runs to test the Re-inlay capsule design. Samples chosen for iron isotope analyses (BR-, Sp- and KGW-series) were characterized in more detail by chemical analyses (section 3.2). The results of iron isotope analyses, comprising kinetic and equilibration experiments between silicate and carbonate melt, are presented in section 3.3. The results of iron isotope ratios on olivine and magnetite grains in the melilitite bomb are presented in the last section of the result chapter (section 3.4).

3.1 Results of the phase relation experiments

A prerequisite for performing phase relation experiments at temperatures above 1025 °C was to find a capsule design that prevented iron loss to the platinum capsule (subsection 3.1.1). With this achieved, the phase relations in iron bearing carbonatite systems could be investigated at pressures of 0.5 and 0.7 GPa and temperatures between 900 and 1200 °C (subsection 3.1.2). The main aim of the phase relation experiments was to obtain phase assemblages suitable for iron isotope analyses.

3.1.1 Capsule design: stability of the Re-inlay

One experimental aim of this study was to test the applicability of a Re-foil inlay in Pt capsules (Matsukage and Kubo, 2003, peridotite melting experiments) for experiments in the carbonatite system at temperatures > 1025 °C, which exceeds the melting point of Au capsules. The Re-inlay was stable during the experimental runs and effectively prevented the loss of iron from the sample into the Pt capsule wall, except for water-containing samples. In some test runs H_2O was added to the starting material. This shifted the p_{O2} of the sample towards more oxidizing conditions, which caused Re to dissolve readily into the carbonate melt, so that the Re-foil was severely damaged. Figure 3.1 illustrates typical cross sections cut from intact capsules after the experiment. Using EDX analyses on the Re-inlay, no iron diffusion into the rhenium was detected (Appendix D). Moreover, mass balance calculations based on the chemical analyses indicate a complete iron recovery after the experiments. The stability of the Re-foil indicates that oxygen fugacity was below the Re–ReO_2 buffer in these experiments (see subsection 2.1.5).

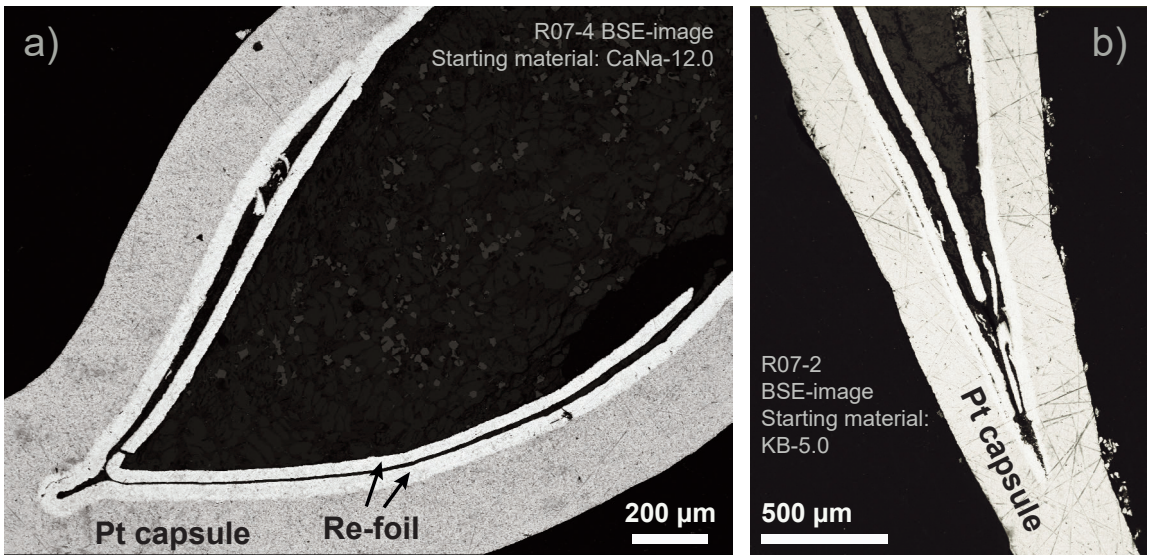

FIGURE 3.1: BSE-images of intact Re-foil inlaying a Pt capsule after an experimental run. Opening the capsules with a low-speed saw and polishing are most likely responsible for the cracks in the Re-foil visible in both images. a) Middle part of a sample cut perpendicular to the long axis of the capsule. b) Capsule end cut along the long axis.

3.1.2 Phase assemblages in the systems KB, CaNa, BR, Sp, and KGW

Table 3.1 lists the phases observed with SEM-EDX and XRD in all experiments. Table 3.2 and Table 3.3 report the changes of the phase assemblages observed in the systems BR and KB with changes of pressure and temperature. The most prevalent phases are illustrated in Figure 3.2 and Figure 3.3. Overall, the phase relations in the iron bearing experiments of this study are similar to those observed in carbonatite systems with no or little iron (e. g. Koster van Groos and Wyllie, 1973; Freestone and Hamilton, 1980; Kjarsgaard, 1998; Brooker and Kjarsgaard, 2011). The presence of iron resulted in the following main features: Iron partitioned into the silicate melt, into silicate minerals, and into the carbonate melt. Calcite did not incorporate iron in amounts detectable with SEM-EDX or EMP-WDX. The chemistry of the systems BR, Sp, and KGW is described in subsection 3.2.1. Notably, when water was added to the system BR, growth of silicate minerals was promoted. As mentioned above, water destabilized the Re-foil.

TABLE 3.1: Phase assemblages observed in the experimental run products

System	Observations
KB (Na_2O-SiO_2-Al_2O_3-CaO-MgO-Fe_2O_3-CO_2)	Phases: carbonate melt, calcite, clinopyroxene, feldspar, a silicate mineral of the aenigmatite-group, magnetite, and a volatile phase. In one sample a quench phase containing silica occurred. The phase assemblage changed with temperature (Table 3.2), textures changed as well.
CaNa (Na_2O-CaO-MgO-Fe_2O_3-CO_2)	Phases: carbonate melt, calcite, magnetite, and a volatile phase. The phase assemblage remained stable over the investigated temperature range, the sample textures changed with temperature.
BR (Na_2O-SiO_2-Al_2O_3-CaO-MgO-Fe_2O_3-CO_2)	Phases: silicate melt, carbonate melt, clinopyroxene, and a volatile phase. In experiments with a runtime < three hours a mineral of the aenigmatite-group occurred. The phase assemblage changed with temperature (Table 3.3).
Sp (Na_2O-SiO_2-Al_2O_3-CaO-MgO-Fe_2O_3-FeO-CO_2)	Phases: silicate melt, carbonate melt, and a volatile phase. In experiments with a runtime < three hours, small amounts (< 1 wt %) of a silicate mineral occurred, all experiments of this series were run at the same pressure and temperatures.
KGW (Na_2O-SiO_2-Al_2O_3-CaO-Fe_2O_3-CO_2)	Phases: silicate melt, carbonate melt, and a volatile phase. The phase assemblages remained stable at 1200 and 1100 °C. At 900 °C, only the system KGW_{1Al} was still above liquidus, in all other compositions silicate minerals occurred, which were not determined in detail. Sample textures and all phases are described below.

TABLE 3.2: Phase assemblages observed by XRD and SEM-EDX analyses in the system KB

Run no.	Starting material[a]	T [C°]	P [GPa]	t [h]	Capsule material	Phase assemblage
R01-1	$KB_{2.6}$	950	0.7	93	Au	Carb. m. + Cc + Cpx + Ab
R01-2	$KB_{5.0}$	950	0.7	93	Au	Carb. m. + Cc + Cpx + Ab + Mag
R01-3	$KB_{10.0}$	950	0.7	93	Au	Carb. m. + Cc + Cpx + Ab + Mag
R01-4	$KB_{17.3}$	950	0.7	93	Au	Carb. m. + Cc + Cpx + Ab + Mag
R04-4	$KB_{5.0}$	1025	0.5	72	Au	Carb. m. + Cc + Cpx + Ae + Mag + V [b]
R04-5	$KB_{10.0}$	1025	0.5	72	Au	Carb. m. + Cc + Cpx + Ae + Mag + V [b]
R046	$KB_{20.0}$	1025	0.5	72	Au	Carb. m. + Cc + Cpx + Mag + V [b]
R05-1	$KB_{5.0}$	1025	0.7	48	Au	Carb. m. + Cc + Cpx + Mag + V [b]
R05-2	$KB_{10.0}$	1025	0.7	48	Au	Carb. m. + Cc + Cpx + Mag + V [b]
R05-3	$KB_{20.0}$	1025	0.7	48	Au	Carb. m. + Cc + Cpx + Mag + V [b]
R07-2	$KB_{5.0}$	1200	0.7	24	Pt + Re	Carb. m. + Cc + Cpx + V [b]
R07-3	$KB_{10.0}$	1200	0.7	24	Pt + Re	Carb. m. + Cc + Cpx + Mag + Q (Si) + V
R06-3	$KB_{20.0}$	1200	0.7	24	Pt + Re	Carb. m. + Cc + Cpx + Mag + V [b]
R080-6	$KB_{5.0}$	1200	0.5	24	Pt + Re	Carb. m. + Cc + Cpx + Mag + V

T – temperature, P – pressure, t – run duration, Carb. m. – carbonate melt, Cc – round calcite, Cpx – clinopyroxene, Ab – albite-rich feldspar, Ae – mineral of the aenigmatite-group, Mag – magnetite, V – volatile phase, Q (Si) – quench texture containing Si. [a] Subscripts indicate the amount of Fe_2O_3 in wt % of the starting material , [b] These samples were scanned only roughly to find samples suited for isotope analyses.

TABLE 3.3: Phase assemblages observed by XRD and SEM-EDX analyses in the system BR

Run no.	Water content [wt %]	T [C°]	P [GPa]	t [h]	Capsule material	Phase assemblage
Water content < 0.2 wt. % (resulting from the use of hydromagnesite as starting material)						
R12-1		1025	0.7	24.5	Au	Sil. m. + Carb. m. + Cpx +V
R11-2		1100	0.7	45	Pt + Re	Sil. m. + Carb. m. + Cpx[a] +V
R13-2		1100	0.7	90.5	Pt + Re	Sil. m. + Carb. m. + V
R80-5		1200	0.5	23	Pt + Re	Sil. m. + Carb. m. + V
R14-1		1200	0.7	2	Pt + Re	Sil. m. + Carb. m. + Ae (< 1 wt %) + V
R14-2		1200	0.7	2	Pt + Re	Sil. m. + Carb. m. + Ae (< 1 wt %) + V
R18-1		1200	0.7	3	Pt + Re	Sil. m. + Carb. m. + V [b]
R07-1		1200	0.7	24	Pt + Re	Sil. m. + Carb. m. + V
R09-1		1200	0.7	42	Pt + Re	Sil. m. + Carb. m. + V
R16-1		1200	0.7	50.5	Pt + Re	Sil. m. + Carb. m. + V
R15-1		1200	0.7	92.5	Pt + Re	Sil. m. + Carb. m. + V
Samples with water added to starting material						
RH-01	10	750	0.2	68	Au	Sil. m. + Carb. m. + Mag + silicate minerals, and others
R12-2	5	1025	0.7	24.5	Au	Sil. m. + Carb. m. + Cpx +V
R12-3	10	1025	0.7	24.5	Au	Sil. m. + Carb. m. + Cpx +V
R08-10	6	1200	0.5	23	Pt + Re	Re dissolved into Carb. m. to form Na-Re-oxides

T – temperature, P – pressure, t – run duration, Sil. m. – silicate melt, Carb. m. – carbonate melt, Cpx – clinopyroxene, Ae – mineral of the aenigmatite-group, V – volatile phase. [a]This run was intermitted and re-started several times. Crystals might be remnants from this. [b]No SEM analyses, small amounts of Cpx or Ae may be present.

Silicate melt

The silicate melt in the BR-, Sp-, and KGW-series quenched to a glass, forming in most cases a single glass bead at the bottom of the capsules, and some smaller droplets separate from the main glass body (Figure 3.3). Mostly, the silicate glass was separated from the surrounding quenched carbonates by sharp, curved menisci (Figure 3.3, b, d), which indicates that the phases separated at run conditions, not during quenching, and are in chemical equilibrium (e. g. Freestone and Hamilton, 1980). The color of the silicate glass varied from light blue over green blue in the KGW-series to brown and dark brown in the BR- and Sp-series. All silicate glasses from experiments of a runtime >3 hours were interspersed with homogeneously sized and distributed spherically shaped bubbles (Figure 3.3, d). These are interpreted as CO_2 bubble nucleation upon cooling. The instantaneous release of CO_2 indicates CO_2 saturation in the silicate melt at run conditions. In silicate glasses from experiments with runtimes <3 hours the pores were not homogeneously distributed and some streaks were visible in BSE-images, indicating an incomplete chemical equilibration.

Clinopyroxene

Clinopyroxene occurred in all samples of the KB-series and in the BR-series in runs below the liquidus temperature. Crystal shapes ranged from idiomorphic needle-shaped crystals with diameters $<15\,\mu m$ to xenomorphic crystals (Figure 3.2). Depending on the chemical compositions of the systems, they contained Fe, Ca, Na, and Mg in varying amounts.

Other silicate minerals

The silicates of the aenigmatite-group observed in the KB-series were hypidiomorphic with diameters of 10 to $20\,\mu m$. Minerals of the aenigmatite-group observed in the BR-series in experiments with runtimes below three hours were of radial growth, needle-shaped (diameter $<3\,\mu m$, length 20 to $30\,\mu m$) and distributed inhomogeneously. The silicate minerals observed in the Sp-series in experiments with runtimes below three hours could not be determined due to their very small grainsizes ($<3\,\mu m$ diameter). Given that in runs with longer durations no minerals were found in samples of the BR- and Sp-series, the observed crystals are interpreted as remnants of phases formed during heating of the experiment.

Sodium-rich carbonate melt

The interpretation of carbonate textures was not unambiguous (subsection 2.3.1), since all carbonate phases were crystalline in the run products. Thus, indicators were needed to

distinguish between carbonate crystalline phases stable at run temperature and carbonate phases that crystallized upon cooling. In the run products of the KB- and CaNa-series, Na-rich carbonate phases with an elongated, laminar texture (Figure 3.2, a, e) coexisted with round pure $CaCO_3$ phases (as described in the next section). Due to the dendritic exsolution textures of iron-oxides found within the Na-Ca-carbonates in some of the samples (Figure 3.2, e), the laminar textures were interpreted as quench products, representing a Na-rich carbonate melt at run conditions.

In run products of the BR-, Sp-, and KGW-series, in which a Na-rich carbonate melt coexisted with a silicate melt, the Na-carbonate phases were identified as quenched liquids by their exsolution textures. These were of dendritic (BR- and Sp-series, Figure 3.3, a-c) to fine-laminar (KGW-series, Figure 3.3, d-f) shapes. Usually, small droplets of silicate melt were dispersed in the carbonate melt. Brooker and Kjarsgaard (2011) found in their experiments that droplets of a diameter > 15 µm had the same composition as the silicate main glass body, whereas smaller droplets differed in composition and were interpreted as exsolution from the carbonate melt during quench.

Small amounts of rhenium diffused into the carbonate melt where it formed small nuggets (Figure 3.3, c). The Re contamination necessitated an additional purification step after the column chemistry and impeded the determination of $Fe^{3+}/\Sigma Fe$ by wet chemistry (subsection 2.3.4, subsection 2.3.3).

Calcite

In all run products of the KB- and CaNa-series, a pure $CaCO_3$ phase of round shape occurred, which was interpreted as calcite, following the guidelines of Brooker and Kjarsgaard (2011), as described in subsubsection 2.3.1. At low run temperatures of 950 °C, the diameters of this phase reached up to 300 µm and calcite formed globules clearly separated from each other (Figure 3.2, e). At run temperatures of 1200 °C, calcite appeared more irregular, but still with round shapes with maximum diameters below 50 µm. These smaller round calcites lined up to form a pattern that looked almost dendritic, but lacked the tree-like form of an exsolution pattern (Figure 3.2, c, d, g, h), therefore these were still interpreted as calcite stable at run conditions. Intermediate temperatures yielded intermediate forms between these two textural extremes.

Magnetite

Magnetite occurred in the run products of the KB- and CaNa-series and had idiomorphic to hypidiomorphic forms. Sizes ranged from 1 up to 100 µm (Figure 3.2, a, e, f). Most crystals contained Al_2O_3, in some cases in amounts up to 9 wt %. In most samples, magnetite crystals were dispersed homogeneously over the whole sample.

Volatile phase

The presence of a volatile phase at run conditions consisting most likely of CO_2, H_2O and dissolved Na^+ was indicated by

- the loss of a fluid phase upon capsule opening (probably CO_2 and H_2O),
- large voids (diameter up to several mm), some of them leaving a negative imprint on the capsule wall after decompression, and
- a white precipitate of sodium carbonate (possibly thermonatrite) that occurred inside of the voids and at the top of the capsule interior. Most likely the precipitate cristallized from the volatile phase during quenching (cf. description in Freestone and Hamilton, 1980).

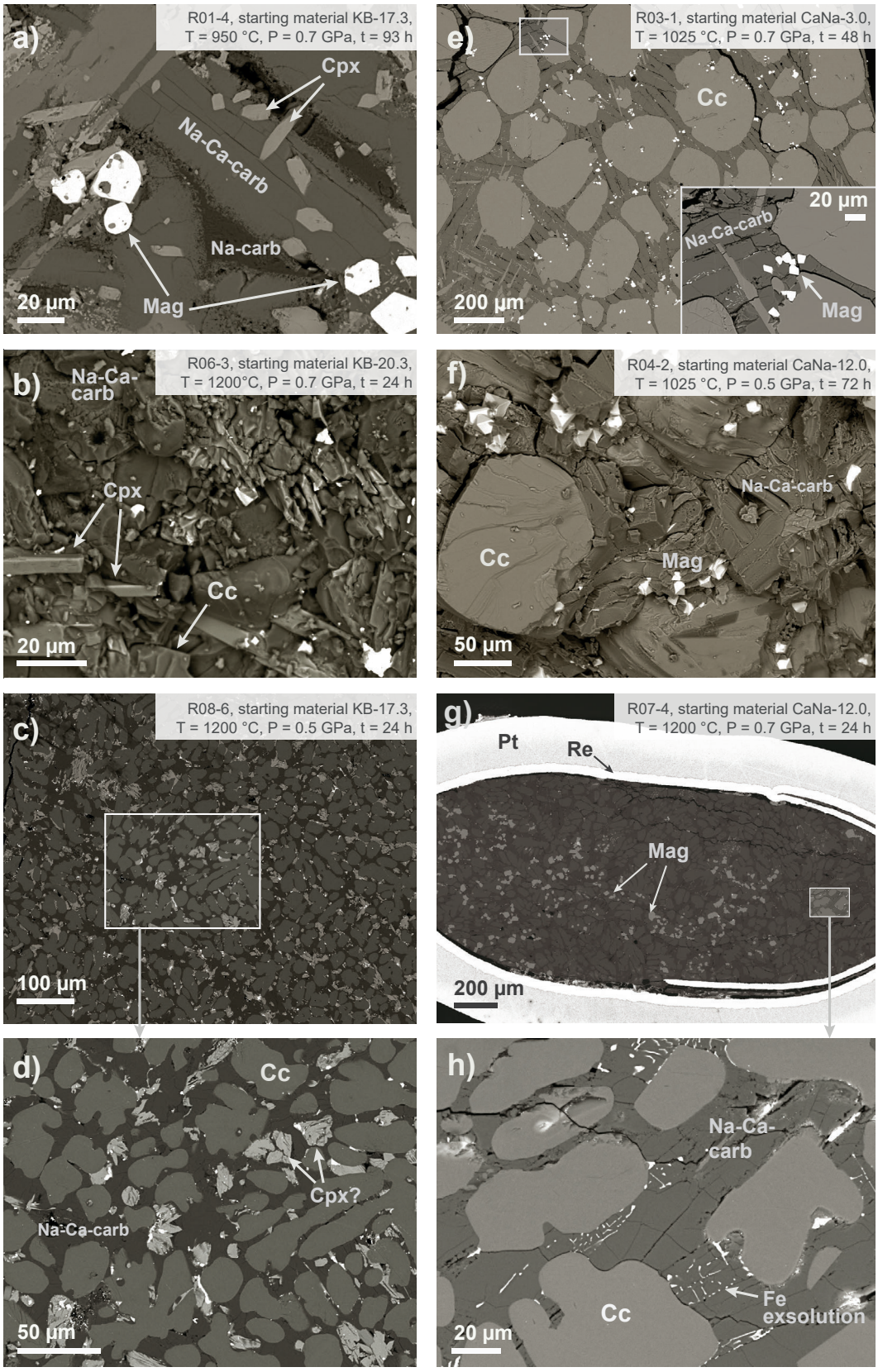

FIGURE 3.2: Representative BSE images of KB run products (left) and CaNa run products (right). All micrographs show polished mounts, except for b) and f), which show mounted broken pieces. g) and h) show a capsule embedded in epoxy and cut open perpendicular to it's elongation. Mag = magnetite, Cc = calcite, Cpx = clino-pyroxene, Pt = platinum capsule, Re = Rhenium inlay.

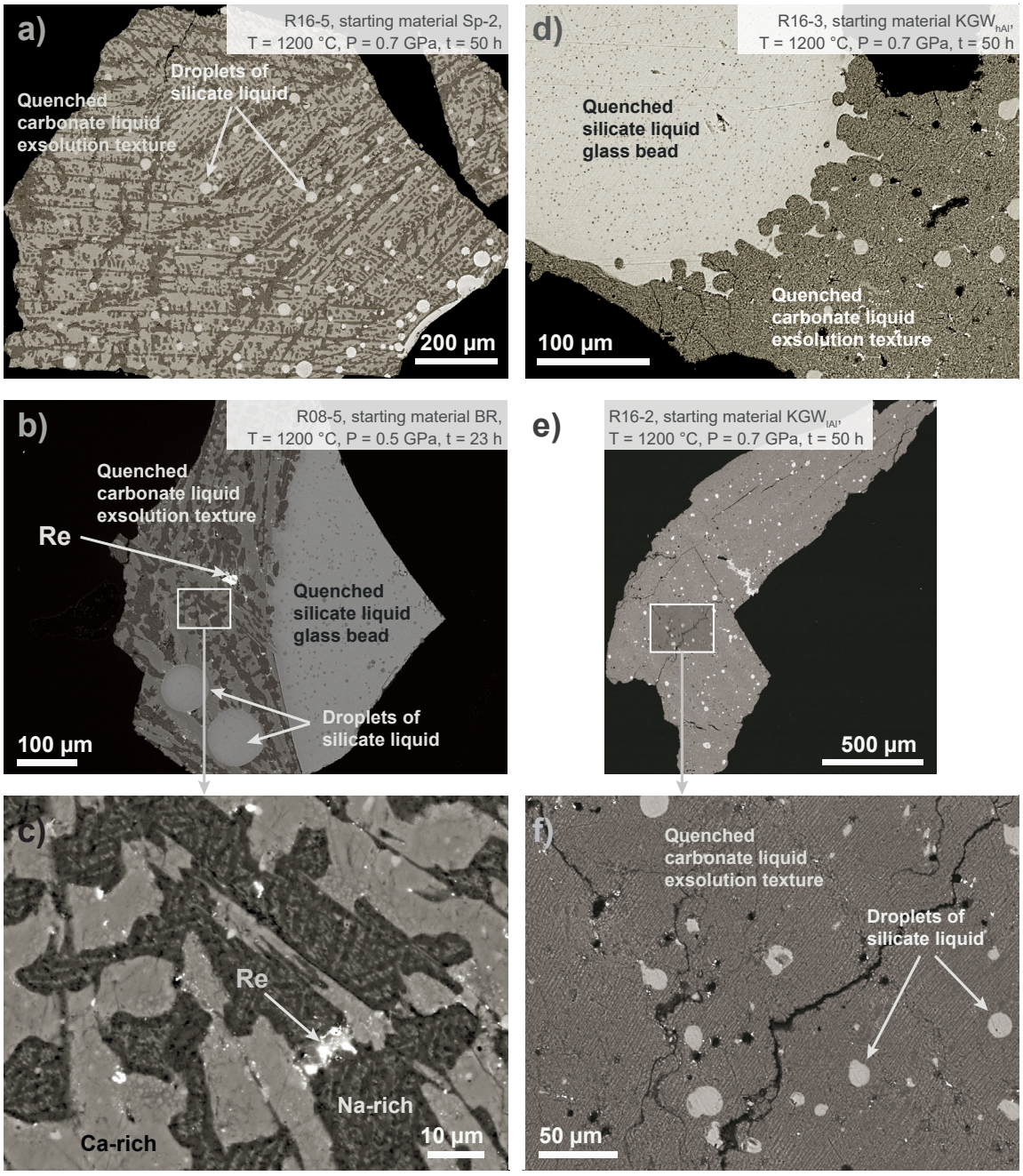

FIGURE 3.3: Representative BSE images of exsolution textures in samples of the BR- and Sp-series (left column) and of the KGW-series (right column). All micrographs show polished mounts. In the BR- and Sp-series, exsolution patterns are of dendritic shape, while exsolution patterns in the KGW-series consist of fine lamellae.

3.2 Characterization of the run products (kinetic and equilibration experiments)

The investigated carbonatite systems that produced immiscible silicate and carbonate melt plus a volatile phase were suitable for iron isotope analyses. Before iron isotope analyses, the run products of these systems (BR, Sp, KGW) were characterized in more detail to ensure the data quality and to investigate potential connections between chemistry, redox state and iron isotope fractionation.

The chemical compositions of the silicate melt quench products (i. e., the silicate glasses) were analyzed by SEM-EDX, EMP-WDX and ICP-OES, the chemical compositions of the carbonate melt quench products (i. e., the Na-Ca-carb$_{qu}$ phases) were analyzed by SEM-EDX and ICP-OES (subsection 3.2.1). The volatile phase could not be analyzed. To assess the oxidation state and coordination of iron in the silicate melt, three selected silicate glasses were characterized by Mössbauer spectroscopy (subsection 3.2.2). Since the carbonate melt does not quench to a glass, an equivalent analysis of the carbonate melt could not be done (subsection 2.3.3).

3.2.1 Results of the chemical analyses (WDX, EDX, ICP-OES)

The results of the chemical analyses of silicate glasses (EDX, WDX, ICP-OES) and Na-Ca-carb$_{qu}$ phases (EDX, ICP-OES) are presented in tables 3.4 to 3.9. In all experiments, the silicate melts are chemically clearly distinct from carbonate melts. This is illustrated in Figure 3.4, where the results of the chemical analyses are presented in a quasi-ternary plot projected from CO_2 (the so called 'Hamilton-plot', since this diagram was originally developed by Hamilton et al., 1979). The iron content is not represented in the Hamilton-plot for a better comparison with former experiments, and because (without knowing the oxidation state of iron) it is difficult to decide whether it should be counted with SiO_2 and Al_2O_3 or with CaO and MgO.

Iron contents are slightly higher in the silicate melt than in the carbonate melt, with the exception of system KGW$_{hAl}$, where iron is more enriched in the carbonate melt (Figure 3.5). The balanced distribution of iron facilitated the phase separation for iron isotope analyses. In all experiments, a free volatile phase was present, as concluded from gas release at capsule opening and large voids that left concave imprints in the capsule wall after decompression. Furthermore, CO_2 saturation of the experiments is indicated by homogeneously distributed bubbles in the silicate glass, which were interpreted as CO_2 exsolution upon cooling (see also subsection 3.1.2).

Depending on the chemical compositions of the investigated systems, the silicate melts have SiO_2 contents between 44.3 wt % (system Sp) and 63.3 wt % (system KGW$_{lAl}$) and ASI of 0.10 (systems KGW$_{lAl+Fe}$ and KGW$_{lAl+Ca}$) to 0.51 (system KGW$_{hAl}$). The

CO_2 content[1] in the silicate melt (estimated from missing totals in EMP-WDX analyses) are between 2.1 wt % (system KGW_{hAl}) and 6.6 wt % (system BR), which is in good agreement with observations in former studies in CO_2 saturated carbonate systems (e. g. Brooker, 1998). Since it is possible that missing totals comprise water as well, these are maximum estimates.

The carbonate melts are dominated by Na_2O (32.2 wt %, system Sp, to 52.1 wt %, system KGW_{lAl}) and CO_2. The CO_2 contents in the carbonate melt (estimated as stoichiometric carbonate for Fe-, Mg-, Ca- and Na-cations) are between 39.8 wt % (system BR) and 41.7 wt % (system KGW_{lAl+Ca}). SiO_2 and Al_2O_3 contents are very low ($\leqslant$ 3.8 wt %, system BR, and $\leqslant$ 0.9 wt %, system BR, resepectively). The low concentration of Si and Al may indicate a low water content in the carbonate melt, since the solubility of Si and Al in the carbonate melt is supposed to increase with water content (Veksler et al., 2012).

The ratios of silicate melt : carbonate melt were estimated from an iterative recalculation of the capsule contents bulk composition from the chemical analyses and were between 0.6 (system Sp) and 0.8 (system KGW_{hAl}).

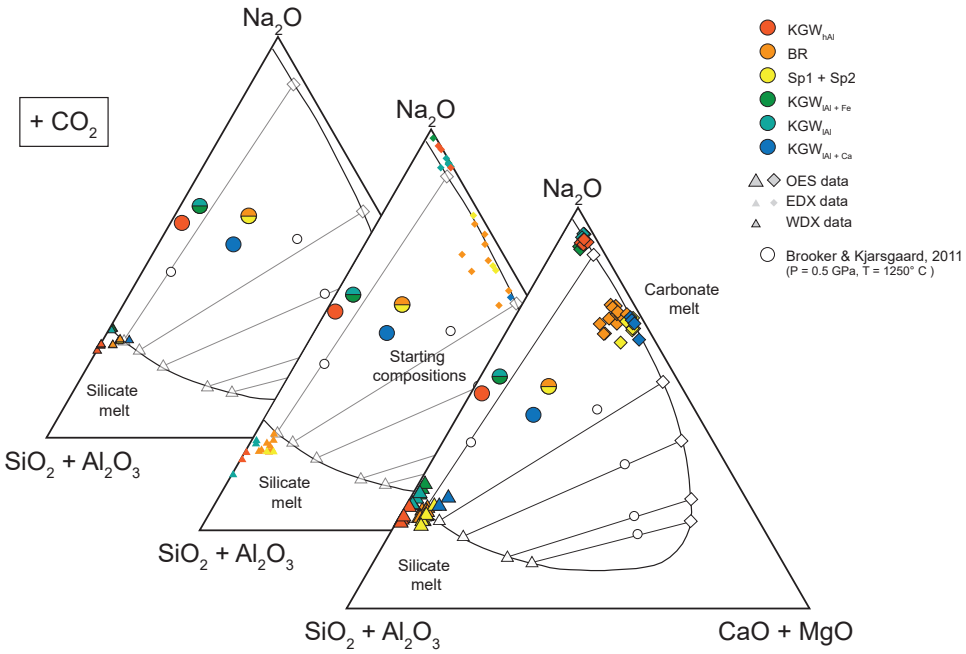

FIGURE 3.4: Results of WDX, EDX, and ICP-OES analyses of corresponding silicate glasses (triangles) and Na-Ca-$carb_{qu}$ phases (rhombs) in the Hamilton-projection, a quasi-ternary plot projected from CO_2. Round symbols indicate the starting compositions. The compositions of the run products are in good agreement with data from previous mostly iron-free experiments (white symbols) by Brooker and Kjarsgaard (2011). The iron content of the samples is not represented in this plot. The scatter in EDX data of the Na-Ca-$carb_{qu}$ phases is caused by the local inhomogeneity of the quench products.

[1] *CO_2* used here as notation of the chemical component – possible speciations of carbon in the silicate melt see in subsection 1.3.2.

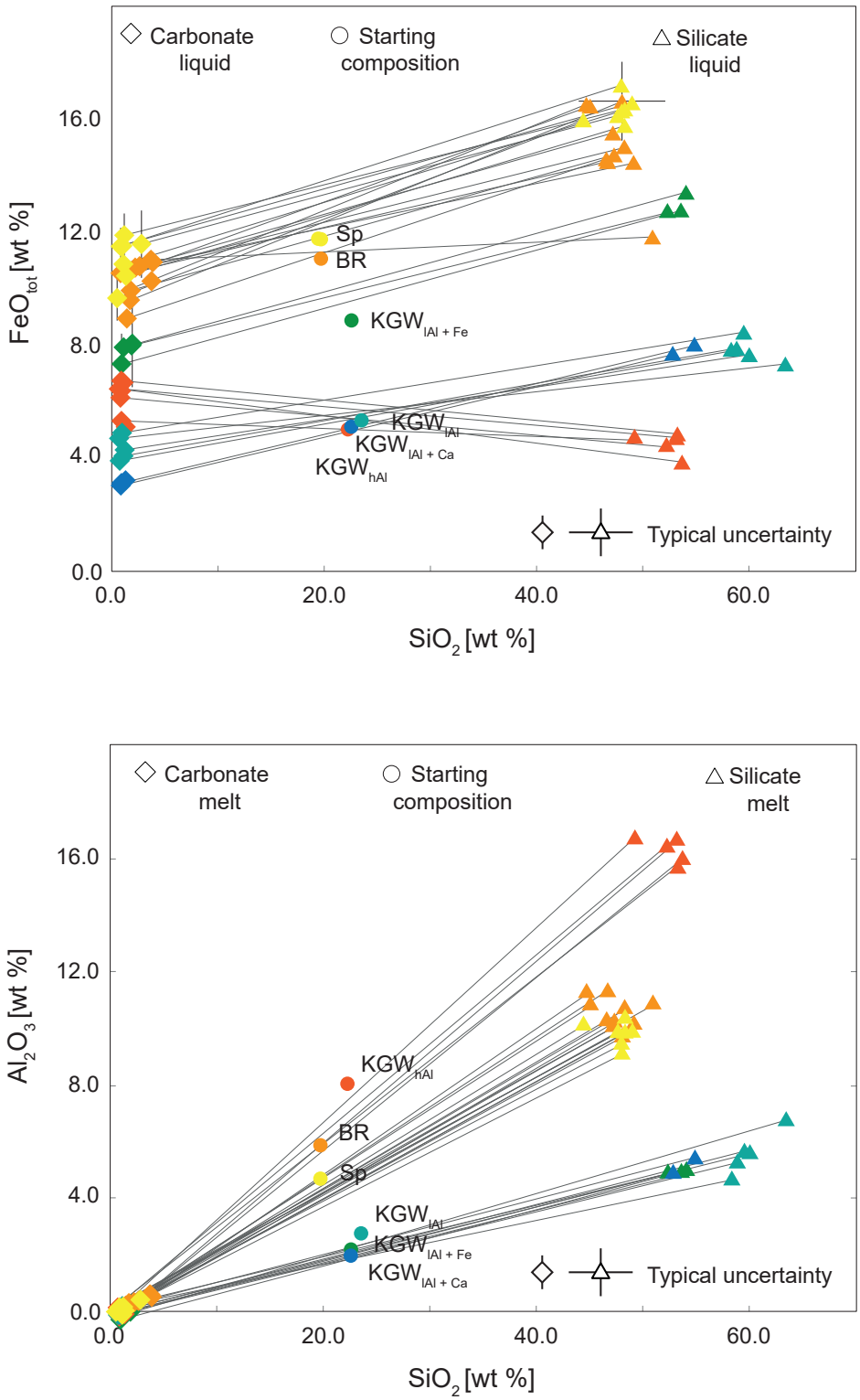

FIGURE 3.5: FeO_{tot} (above) and Al_2O_3 (below) concentrations in corresponding silicate glasses (triangles) and Na-Ca-$carb_{qu}$ phases (rhombs). Grey tie-lines indicate corresponding pairs of silicate and carbonate melt from the same experiment. In all systems, with the exception of KGW_{hAl}, iron is slightly more enriched in the silicate glass. SiO_2 and Al_2O_3 are concentrated in the silicate melt in all run products. Large error bars on some samples are related to very small sample weights, causing larger weighing uncertainties.

TABLE 3.4: Results of the chemical analyses and Mössbauer spectroscopy – BR-series *(1/3)*

Experiment no.	R14-1						R14-2						R18-1		
Temperature / Pressure / time	1200 °C / 0.7 GPa / 2 h						1200 °C / 0.7 GPa / 2 h						1200 °C / 0.7 GPa / 3 h		
	OES[a, *]	EDX	SD	WDX	SD	norm.[b]	OES[a]	EDX	SD	WDX	SD	norm.[b]	OES[a, *]	EDX	WDX
Silicate melt															
No. of analyses (EDX/WDX)		15		29						19					
SiO_2[c]	47.2	50.2	0.9	44.6	0.8	47.8	47.3			44.8	1.1	47.0	48.3		
Al_2O_3	13.0	12.3	0.4	12.6	0.3	13.1	13.1			13.0	0.4	13.6	13.7		
FeO	15.6	16.6	0.5	14.1	0.5	15.1	14.8			14.8	0.2	15.5	15.1		
MgO	1.3	1.1	0.1	1.3	0.1	1.3	1.2	n. a.		1.3	0.1	1.3	1.2	n. a.	n. a.
CaO	3.1	2.5	0.5	1.7	0.2	1.8	2.6			1.7	0.5	1.8	2.3		
Na_2O	19.7	17.2	0.5	19.2	0.4	20.5	21.0			19.8	0.5	20.0	19.3		
CO_2[d]	-	-		6.6		-	-			4.8		-	-		
Total	100.0	100.0		93.4	0.8	100.0	100.0			95.2	1.0	100.0	100.0		
$Fe^{3+}/\Sigma Fe$	n. a.						n. a.						n. a.		
Na/Al	2.5						2.7						2.3		
ASI[e]	0.22						0.22						0.24		
n_{mod}/n_{form}[f]	0.63						0.65						0.57		
Carbonate melt	light color	dark color					light color	dark color							
No. of analyses (EDX)			2						12						
SiO_2[c]	2.1	3.8	3.4	5.7			1.7	3.6	3.0	5.0			1.4		
Al_2O_3	0.5	0.9	0.9	0.2			0.4	0.9	0.1	0.5			0.3		
FeO	10.7	10.9	11.4	0.1			9.9	10.3	16.5	0.8			10.6		
MgO	1.9	1.8	2.0	0.4		n. a.	1.7	1.6	1.9	0.3		n. a.	1.8	n. a.	n. a.
CaO	9.2	8.6	11.0	1.1			8.1	7.9	14.1	1.9			8.6		
Na_2O	34.9	34.2	31.3	1.5			37.5	35.9	24.1	1.7			36.3		
CO_2[g]	40.7	39.7	40.0				40.8	39.8	40.3				41.0		
Total	100.0	100.0	100.0				100.0	100.0	100.0				100.0		
Volatile phase															
CO_2 (wt. %)[h]			1.8						1.3					1.4	
X_{H2O}[i]			0.2						0.5					0.1	

n.a. – not analyzed, SD – standard deviation, (a) the typical uncertainty resulting from weighing, dilution, and ICP-OES analyses is 6%, * mark higher uncertainties resulting from very small sample amounts, (b) normalized without CO_2 for a better comparison of the methods, (c) SiO_2 of the ICP-OES analyses was recalculated from the Si/Fe ratio in the silicate glass (Si/Al in carbonate quench phase, resepctively) determined by WDX and EDX (subsection 2.3.2), (d) estimate of CO_2 content derived from difference to 100 % total of silicate glass WDX analyses, (e) ASI calculated as molar $Al_2O_3/CaO + Na_2O + FeO$, (f) n_{mod}/n_{form} calculated as molar (Ca+Fe+Na-Al)/(Si+Al), (g) CO_2 content of the carb. melt was recalculated as stoichiometric carbonate for all Fe-, Mg-, Ca- and Na-cations, (h) amount of CO_2 released at capsule opening, here given as percentage of the weighed starting material (subsection 2.1.6), (i) X_{H2O} calculated as molar $H_2O/(CO_2 + H_2O)$ as determined at the capsule opening (subsection 2.1.6), (*) higher uncertainties on ICP-OES analyses: R14-1, silicate melt: 7 %, R18-1, carbonate melt: 8 %.

TABLE 3.4: Results of the chemical analyses and Mössbauer spectroscopy – BR-series *(continued, 2/3)*

Experiment no.	R09-1				R16-1						R15-1				R08-5			
Temperature / Pressure / time	1200 °C / 0.7 GPa / 42 h				1200 °C / 0.7 GPa / 50 h						1200 °C / 0.7 GPa / 92 h				1200 °C / 0.5 GPa / 23 h			
	OES[a]	EDX	SD	WDX	OES[a]	EDX	SD	WDX	SD	norm.[b]	OES[a]	EDX	SD	WDX	OES[a, *]	EDX	SD	WDX
Silicate melt																		
No. of analyses (EDX/WDX)		15				5		20				13				15		
SiO_2[c]	49.0	49.2	1.2		44.6	50.0	0.4	45.0	1.0	47.1	44.9	49.6	0.3		48.0	48.9	1.0	
Al_2O_3	13.2	12.7	0.3		14.5	11.9	0.4	13.0	0.2	13.6	14.0	11.7	0.3		12.6	12.1	0.4	
FeO	14.5	14.6	0.4		16.6	18.6	0.2	14.4	0.2	15.1	16.6	18.3	0.4		16.7	17.1	0.6	
MgO	1.1	1.0	0.1	n. a.	1.3	1.0	0.2	1.2	0.1	1.3	1.3	1.0	0.1	n. a.	1.4	1.2	0.2	n. a.
CaO	2.3	2.2	0.3		2.7	3.2	0.3	1.9	0.5	2.0	2.8	3.4	0.2		3.1	2.6	0.6	
Na_2O	19.8	20.2	1.4		20.2	15.4	0.1	20.0	0.6	21.0	20.2	16.0	0.3		18.3	18.2	0.7	
CO_2[d]	-	-			-	-		4.4			-	-			-	-		
Total	100.0	100.0			100.0	100.0		95.6	1.0	100.0	100.0	100.0			100.0	100.0		
Fe^{3+}/Σ Fe	n. a.				0.24						n. a.				n. a.			
Na/Al	2.5				2.3						2.4				2.4			
ASI[e]	0.23				0.23						0.23				0.21			
n_{mod}/n_{form}[f]	0.58				0.63						0.64				0.60			
Carbonate melt																		
No. of analyses (EDX)						18						7				16		
SiO_2[c]	2.5				*1.7*	1.3	0.4				0.7	1.7	2.9		1.6	0.5	0.8	
Al_2O_3	0.6				*0.4*	0.1	0.4				0.2	0.0	0.0		0.4	0.1	0.5	
FeO	10.8				*10.0*	14.4	0.2				10.6	12.8	1.6		9.6	9.3	1.7	
MgO	1.7	n. a.		n. a.	*1.5*	2.1	0.2		n. a.		1.9	2.0	0.5	n. a.	1.6	2.1	0.4	n. a.
CaO	8.3				*7.8*	14.5	0.3				9.6	11.4	2.5		9.1	10.2	2.4	
Na_2O	35.7				***37.8***	26.4	0.1				35.7	31.1	2.1		36.8	36.2	3.4	
CO_2[g]	40.3				*40.8*	41.2					41.4	41.0			40.9	41.7		
Total	100.0				100.0	100.0					100.0	100.0			100.0	100.0		
Volatile phase																		
CO_2 (wt. %)[h]		1.7					n. a.					1.8				3.3		
X_{H2O}[i]		0.1					n. a.					0.1				0.1		

n.a. – not analyzed, SD – standard deviation, ***italics*** – minimum estimate where element exceeded the calibration range in OES analyses, (a) the typical uncertainty resulting from weighing, dilution, and ICP-OES analyses is 6%, * mark higher uncertainties resulting from very small sample amounts, (b) normalized without CO_2 for a better comparison of the methods, (c) SiO_2 of the ICP-OES analyses was recalculated from the Si/Fe ratio in the silicate glass (Si/Al in carbonate quench phase, resepctively) determined by WDX and EDX (subsection 2.3.2), (d) estimate of CO_2 content derived from difference to 100 % total of silicate glass WDX analyses, (e) ASI calculated as molar $Al_2O_3/CaO + Na_2O + FeO$, (f) n_{mod}/n_{form} calculated as molar (Ca+Fe+Na-Al)/(Si+Al), (g) CO_2 content of the carb. melt was recalculated as stoichiometric carbonate for all Fe-, Mg-, Ca- and Na-cations, (h) amount of CO_2 released at capsule opening, here given as percentage of the weighed starting material (subsection 2.1.6), (i) X_{H2O} calculated as molar $H_2O/(CO_2 + H_2O)$ as determined at the capsule opening (subsection 2.1.6), (*) higher uncertainties of ICP-OES analysis: R08-5, silicate melt: 10 %.

TABLE 3.4: Results of the chemical analyses and Mössbauer spectroscopy – BR-series *(continued, 3/3)*

Experiment no.	R112				R131					R132				
Temperature / Pressure / time	1100 °C / 0.7 GPa / 45 h				1100 °C / 0.7 GPa / 90 h					1100 °C / 0.7 GPa / 90 h				
	OES[a]	EDX	SD	WDX	OES[a]	EDX	WDX	SD	norm.[b]	OES[a]	EDX	SD	WDX	SD	norm.[b]
Silicate melt															
No. of analyses (EDX/WDX)		18					40				21		40		
SiO_2[c]	46.5	51.0	0.7		46.6		46.7	0.6	49.7		52.6	0.8	46.4	0.6	49.7
Al_2O_3	13.2	12.2	0.4		14.4		12.9	0.2	13.8		12.8	0.5	12.8	0.3	13.8
FeO	14.7	16.1	0.5		14.6		13.2	0.3	14.1		15.4	0.6	13.1	0.3	14.1
MgO	1.3	0.8	0.4	n. a.	1.2	n. a.	1.0	0.1	1.1	n. a.	0.5	0.5	1.0	0.1	1.1
CaO	2.5	2.1	0.1		1.9		1.3	0.1	1.4		2.1	0.2	1.3	0.2	1.4
Na_2O	21.5	17.8	0.6		21.0		18.7	0.3	20.0		16.6	0.4	18.7	0.4	20.0
CO_2[d]	-	-			-		6.1	0.9	-		-		6.6	1.0	-
Total	100.0	100.0			100.0		93.9	0.9	100.0		100.0		93.4	1.0	100.0
Fe^{3+}/Σ Fe	n. a.				n. a.					n. a.					
Na/Al	2.7				2.4					n. a.					
ASI[e]	0.22				0.24					n. a.					
n_{mod}/n_{form}[f]	0.66				0.60					n. a.					
Carbonate melt															
No. of analyses (EDX)		13									12				
SiO_2[c]	1.3	1.3	1.4		1.4						1.1	1.9			
Al_2O_3	0.3	0.3	0.7		0.3						0.0	0.0			
FeO	9.0	9.0	1.7		10.6						12.4	2.6			
MgO	1.8	1.8	0.5	n. a.	1.8	n. a.		n. a.		n. a.	2.1	0.6		n. a.	
CaO	8.3	8.3	2.7		9.1						10.1	3.0			
Na_2O	38.2	38.2	3.7		35.8						33.0	4.0			
CO_2[g]	41.1	41.1			41.0						41.3				
Total		100.0			100.0						100.0				
Volatile phase															
CO_2 (wt. %)[h]		2.9					1.4					1.0			
X_{H2O}[i]		0.1					0.1					0.2			

n.a. – not analyzed, SD – standard deviation, (a) the typical uncertainty resulting from weighing, dilution, and ICP-OES analyses is 6%, (b) normalized without CO_2 for a better comparison of the methods, (c) SiO_2 of the ICP-OES analyses was recalculated from the Si/Fe ratio in the silicate glass (Si/Al in carbonate quench phase, resepctively) determined by WDX and EDX (subsection 2.3.2), (d) estimate of CO_2 content derived from difference to 100 % total of silicate glass WDX analyses, (e) ASI calculated as molar $Al_2O_3/CaO + Na_2O + FeO$, (f) n_{mod}/n_{form} calculated as molar (Ca+Fe+Na-Al)/(Si+Al), (g) CO_2 content of the carb. melt was recalculated as stoichiometric carbonate for all Fe-, Mg-, Ca- and Na-cations, (h) amount of CO_2 released at capsule opening, here given as percentage of the weighed starting material (subsection 2.1.6), (i) X_{H2O} calculated as molar $H_2O/(CO_2 + H_2O)$ as determined at the capsule opening (subsection 2.1.6).

TABLE 3.5: Results of the chemical analyses and Mössbauer spectroscopy – Sp-series *(1/2)*

Experiment no.	R14-5			R14-6				R18-6			R18-7			R16-6					
Temperature / Pressure / time	1200 °C / 0.7 GPa / 2 h			1200 °C / 0.7 GPa / 2 h				1200 °C / 0.7 GPa / 3 h			1200 °C / 0.7 GPa / 3 h			1200 °C / 0.7 GPa / 51 h					
	OES[a, *]	EDX	WDX	OES[a]	EDX	SD	WDX	OES[a, *]	EDX	WDX	OES[a, *]	EDX	WDX	OES[a]	EDX	SD	WDX	SD	norm.[b]
Silicate melt																			
No. of analyses (EDX/WDX)					37												39		
SiO_2[c]	48.8			48.1	52.1	3.8		47.5			48.2			47.9			45.7	0.8	47.7
Al_2O_3	12.7			13.2	11.1	1.2		12.7			12.8			11.8			12.5	0.2	13.0
FeO	16.7			15.9	17.2	1.7		16.2			16.4			16.3			15.6	0.5	16.3
MgO	1.3	n. a.	n. a.	1.2	0.8	0.4	n. a.	1.2	n. a.	n. a.	1.2	n. a.	n. a.	1.2	n. a.		1.2	0.1	1.2
CaO	3.2			3.0	2.9	1.1		2.8			2.8			3.1			1.9	0.2	2.0
Na_2O	17.4			18.6	15.9	1.1		19.5			18.5			19.7			18.9	0.4	19.8
CO_2[d]	-			-	-			-			-						4.1		-
Total	100.0				100.0			100.0			100.0						95.9	1.0	100.0
$Fe^{3+}/\Sigma Fe$	n. a.			n. a.				n. a.			n. a.			n. a.					
Na/Al	2.3			2.3				2.5			2.4			2.8					
ASI[e]	0.22			0.23				0.21			0.22			0.19					
n_{mod}/n_{form}[e]	0.57			0.58				0.63			0.59			0.67					
Carbonate melt																			
No. of analyses (EDX)					9										7				
SiO_2[c]	2.7			*1.2*	1.4	2.4		0.7			1.1			1.0	0.7	1.1			
Al_2O_3	0.6			*0.3*	0.2	0.6		0.2			0.3			0.3	0.0	0.0			
FeO	11.6			*10.5*	11.8	0.6		11.5			11.9			10.9	9.4	2.2			
MgO	1.7	n. a.	n. a.	*1.5*	1.7	0.4	n. a.	1.8	n. a.	n. a.	1.9	n. a.	n. a.	1.7	0.5	1.1		n. a.	
CaO	10.8			*10.4*	12.8	1.2		10.5			10.8			11.2	9.4	1.9			
Na_2O	32.2			***35.1***	31.0	0.9		33.9			32.9			33.7	38.8	5.0			
CO_2[f]	40.3			*41.1*	41.1			41.4			41.2			41.2	41.2				
Total	100.0				100.0			100.0			100.0			100.0	100.0				
Volatile phase																			
CO_2 (wt. %)[g]		1.7			2.2				2.1			1.8				2.5			
X_{H2O}[h]		0.4			0.2				0.1			0.2				0.2			

n.a. – not analyzed, SD – standard deviation, ***italics*** – minimum estimate where element exceeded the calibration range in OES analyses, (a) the typical uncertainty resulting from weighing, dilution, and ICP-OES analyses is 6%, * mark higher uncertainties resulting from very small sample amounts, (b) normalized without CO_2 for a better comparison of the methods, (c) SiO_2 of the ICP-OES analyses was recalculated from the Si/Fe ratio in the silicate glass (Si/Al in carbonate quench phase, resepctively) determined by WDX and EDX (subsection 2.3.2), (d) estimate of CO_2 content derived from difference to 100 % total of silicate glass WDX analyses, (e) ASI calculated as molar $Al_2O_3/CaO + Na_2O + FeO$, (f) CO_2 content of the carb. melt was recalculated as stoichiometric carbonate for all Fe-, Mg-, Ca- and Na-cations, (g) amount of CO_2 released at capsule opening, here given as percentage of the weighed starting material (subsection 2.1.6), (h) X_{H2O} calculated as molar $H_2O/(CO_2 + H_2O)$ as determined at the capsule opening (subsection 2.1.6), (*) higher uncertainties of ICP-OES analysis: R14-5, carb. melt: 12 %, R18-6, carb. melt: 8 %, R18-7, carb. melt: 9 %.

TABLE 3.5: Results of the chemical analyses and Mössbauer spectroscopy – Sp-series *(continued, 2/2)*

Experiment no.	R15-5				R15-6				
Temperature / Pressure / time	1200 °C / 0.7 GPa / 92 h				1200 °C / 0.7 GPa / 92 h				
	OES[a, *]	EDX	SD	WDX	OES[a]	EDX	WDX	SD	norm.[b]
Silicate melt									
No. of analyses (EDX/WDX)		7					20		
SiO_2[c]	44.3	50.2	0.3		47.8		44.7	1.4	46.6
Al_2O_3	13.0	11.2	0.4		12.2		12.4	0.3	13.0
FeO	16.1	18.2	0.3		17.3		16.1	0.4	16.9
MgO	1.3	0.9	0.1	n. a.	1.2	n. a.	1.2	0.1	1.2
CaO	3.5	3.9	0.2		3.1		2.1	0.6	2.2
Na_2O	21.7	15.6	0.4		18.3		19.2	0.7	20.1
CO_2[d]	-	-					4.2		-
Total		100.0					95.8	1.4	100.0
$Fe^{3+}/\Sigma Fe$	n. a.				n. a.				
Na/Al	2.8				2.5				
ASI[e]	0.20				0.20				
n_{mod}/n_{form}[e]	0.74				0.63				
Carbonate melt									
No. of analyses (EDX)		14							
SiO_2[c]	0.4	1.6	2.6		*0.9*				
Al_2O_3	0.1	0.0	0.0		*0.3*				
FeO	9.7	11.7	2.5		*11.5*				
MgO	1.7	1.6	0.3	n. a.	*1.7*	n. a.		n. a.	
CaO	10.8	13.5	3.7		*11.1*				
Na_2O	35.7	30.5	3.3		***33.3***				
CO_2[f]	41.6	41.2			*41.3*				
Total		100.0			100.0				
Volatile phase									
CO_2 (wt. %)[g]		3.3					2.9		
X_{H2O}[h]		0.0					0.1		

n.a. – not analyzed, SD – standard deviation, ***italics*** – minimum estimate where element exceeded the calibration range in OES analyses, (a) the typical uncertainty resulting from weighing, dilution, and ICP-OES analyses is 6%, * mark higher uncertainties resulting from very small sample amounts, (b) normalized without CO_2 for a better comparison of the methods, (c) SiO_2 of the ICP-OES analyses was recalculated from the Si/Fe ratio in the silicate glass (Si/Al in carbonate quench phase, reseptively) determined by WDX and EDX (subsection 2.3.2), (d) estimate of CO_2 content derived from difference to 100 % total of silicate glass WDX analyses, (e) ASI calculated as molar $Al_2O_3/CaO + Na_2O + FeO$, (f) CO_2 content of the carb. melt was recalculated as stoichiometric carbonate for all Fe-, Mg-, Ca- and Na-cations, (g) amount of CO_2 released at capsule opening, here given as percentage of the weighed starting material (subsection 2.1.6), (h) X_{H2O} calculated as molar $H_2O/(CO_2 + H_2O)$ as determined at the capsule opening (subsection 2.1.6), (*) higher uncertainties of ICP-OES analysis: R15-5, carb. melt: 10 %.

TABLE 3.6: Results of the chemical analyses and Mössbauer spectroscopy – KGW_{1Al}-series

Experiment no.	R14-3				R182			R16-2						R13-3				R17-1					
Temperature / Pressure / time	1200 °C / 0.7 GPa / 2 h				1200 °C / 0.7 GPa / 3 h			1200 °C / 0.7 GPa / 51 h						1100 °C / 0.7 GPa / 90 h				900 °C / 0.7 GPa / 91 h					
	OES[a]	EDX	SD	WDX	OES[a]	EDX	WDX	OES[a]	EDX	SD	WDX	SD	norm.[b]	OES[a,*]	EDX	SD	WDX	OES[a]	EDX	SD	EDX	SD	WDX
Silicate melt																							
No. of analyses (EDX/WDX)		32									20				24				12				
SiO_2[c]	59.4	63.8	1.1		*58.7*			*58.2*			56.5	1.0	58.4	59.9	64.1	0.6		*63.3*	72.0	0.4			
Al_2O_3	7.3	6.9	0.3		*7.0*			*6.3*			7.5	0.2	7.7	7.4	6.8	0.3		*8.8*	7.4	0.5			
FeO	8.5	9.1	0.7		*8.0*			*7.9*			8.1	0.2	8.4	7.7	8.2	0.6		*7.4*	8.4	0.4			
MgO	0.0	0.0	0.0	n. a.	*0.0*	n. a.	n. a.	*0.0*	n. a.		0.0	0.0	0.0	0.0	0.0	0.0	n. a.	*0.0*	0.0	0.0			n. a.
CaO	0.9	1.0	0.2		*0.8*			*0.8*			0.7	0.1	0.8	0.6	0.7	0.4		*0.3*	0.0	0.0			
Na_2O	23.9	19.1	0.6		***25.5***			***26.8***			23.8	0.7	24.6	24.2	20.1	0.5		***20.2***	12.2	0.6			
CO_2[d]	-	-			-			-			3.4		-	-	-			-	-				
Total	100.0	100.0			100.0			100.0			96.6	0.7	100.0	100.0	100.0			100.0	100.0				
$Fe^{3+}/\Sigma Fe$	n. a.				n. a.			n. a.						0.12				n. a.					
Na/Al	5.4				6.0			7.0						5.4				3.8					
ASI[e]	0.14				0.13			0.11						0.14				0.20					
n_{mod}/n_{form}[e]	0.67				0.73			0.79						0.66				0.48					
Carbonate melt																			light color		dark color		
No. of analyses (EDX)		29							7						8				7		28		
SiO_2[c]	0.9	1.0	1.7		1.0			*0.6*	0.2	0.3				1.1	0.0	0.0		*0.6*	0.0	0.0	0.1	0.1	
Al_2O_3	0.1	0.3	0.9		0.1			*0.1*	0.0	0.0				0.1	0.0	0.0		*0.1*	0.0	0.0	0.0	0.0	
FeO	4.9	6.0	1.1		4.1			*3.9*	6.9	1.6				4.3	5.8	1.6		*4.7*	0.0	0.0	9.5	1.7	
MgO	0.0	0.0	0.0	n. a.	0.0	n. a.	n. a.	*0.0*	0.0	0.0		n. a.		0.0	0.0	0.0	n. a.	*0.0*	0.0	0.0	0.0	0.0	n. a.
CaO	2.8	3.7	0.4		2.3			*2.2*	4.2	0.6				2.6	3.7	0.5		*2.3*	5.2	1.0	4.1	0.7	
Na_2O	50.4	48.2	2.5		51.6			***52.1***	47.5	1.4				51.0	49.2	1.7		***51.3***	53.0	1.0	45.3	1.5	
CO_2[f]	41.0	40.8			40.9			*41.1*	41.2					40.9	41.4			*41.1*	41.8		41.1		
Total	100.0	100.0			100.0			100.0	100.0					100.0	100.0			100.0	100.0		100.0		
Volatile phase																							
CO_2 (wt. %)[g]		3.2				3.3				3.7					3.2					1.4			
X_{H2O}[h]		0.1				0.1				0.1					0.1					0.2			

n.a. – not analyzed, SD – standard deviation, ***italics*** – minimum estimate where element exceeded the calibration range in OES analyses, (a) the typical uncertainty resulting from weighing, dilution, and ICP-OES analyses is 6%, * mark higher uncertainties resulting from very small sample amounts, (b) normalized without CO_2 for a better comparison of the methods, (c) SiO_2 of the ICP-OES analyses was recalculated from the Si/Fe ratio in the silicate glass (Si/Al in carbonate quench phase, resepctively) determined by WDX and EDX (subsection 2.3.2), (d) estimate of CO_2 content derived from difference to 100 % total of silicate glass WDX analyses, (e) ASI calculated as molar $Al_2O_3/CaO + Na_2O + FeO$, (f) CO_2 content of the carb. melt was recalculated as stoichiometric carbonate for all Fe-, Mg-, Ca- and Na-cations, (g) amount of CO_2 released at capsule opening, here given as percentage of the weighed starting material (subsection 2.1.6), (h) X_{H2O} calculated as molar $H_2O/(CO_2 + H_2O)$ as determined at the capsule opening (subsection 2.1.6), (*) higher uncertainties of ICP-OES analysis: R13-3, carb. melt: 7 %.

TABLE 3.7: Results of the chemical analyses and Mössbauer spectroscopy – KGW_{hAl}-series *(1/2)*

Experiment no.	R14-4					R18-3			R16-3					
Temperature / Pressure / time	1200 °C / 0.7 GPa / 2 h					1200 °C / 0.7 GPa / 3 h			1200 °C / 0.7 GPa / 50 h					
	OES[a]	EDX	WDX	SD	norm.[b]	OES[a, *]	EDX	WDX	OES[a, *]	EDX	SD	WDX	SD	norm.[b]
Silicate melt														
No. of analyses (EDX/WDX)			20							9		20		
SiO_2[c]	53.2		50.9	0.6	52.4	52.1			*49.2*	59.3	0.5	51.4	0.5	52.6
Al_2O_3	19.8		19.8	0.2	20.4	20.7			***21.3***	18.7	0.3	20.1	0.3	20.5
FeO	4.9		4.7	0.2	4.8	4.5			*4.8*	5.8	0.3	4.6	0.2	4.7
MgO	0.0	n. a.	0.0	0.0	0.0	0.0	n. a.	n. a.	*0.0*	0.0	0.0	0.0	0.0	0.0
CaO	0.4		0.3	0.1	0.3	0.3			*0.3*	0.1	0.2	0.2	0.0	0.2
Na_2O	21.5		21.5	0.5	22.2	22.1			***24.4***	16.2	0.2	21.5	0.4	22.0
CO_2[d]	-		2.8		-	-			-	-		2.1		-
Total	100.0		97.2	0.4	100.0	100.0			100.0	100.0		97.9	0.4	100.0
$Fe^{3+}/\Sigma Fe$	n. a.					n. a.			n. a.					
Na/Al	1.8					1.8			1.9					
ASI[e]	0.46					0.48			0.45					
n_{mod}/n_{form}[e]	0.30					0.29			0.36					
Carbonate melt						light color	dark color		upper part	lower part				
No. of analyses (EDX)											58			
SiO_2[c]	0.8					1.0	*0.7*		*0.8*	*1.2*	0.1	0.2		
Al_2O_3	0.3					0.4	*0.3*		*0.3*	*0.4*	0.0	0.0		
FeO	6.7					6.7	*6.1*		*5.3*	*5.1*	9.5	1.0		
MgO	0.0	n. a.		n. a.		0.0	*0.0*	n. a.	n. a.	*0.0*	*0.0*	0.0	0.0	n. a.
CaO	3.0					2.9	*2.6*		*2.6*	*2.5*	4.5	0.4		
Na_2O	48.3					48.4	***49.4***		***50.2***	***50.1***	44.8	1.0		
CO_2[f]	40.8					40.7	*40.9*		*40.9*	*40.7*	41.1			
Total	100.0					100.0	100.0		100.0	100.0	100.0			
Volatile phase														
CO_2 (wt. %)[g]			2.9				2.8				3.1			
X_{H2O}[h]			0.0				0.0				0.0			

n.a. – not analyzed, SD – standard deviation, ***italics*** – minimum estimate where element exceeded the calibration range in OES analyses, (a) the typical uncertainty resulting from weighing, dilution, and ICP-OES analyses is 6%, * mark higher uncertainties resulting from very small sample amounts, (b) normalized without CO_2 for a better comparison of the methods, (c) SiO_2 of the ICP-OES analyses was recalculated from the Si/Fe ratio in the silicate glass (Si/Al in carbonate quench phase, reseptively) determined by WDX and EDX (subsection 2.3.2), (d) estimate of CO_2 content derived from difference to 100 % total of silicate glass WDX analyses, (e) ASI calculated as molar $Al_2O_3/CaO + Na_2O + FeO$, (f) CO_2 content of the carb. melt was recalculated as stoichiometric carbonate for all Fe-, Mg-, Ca- and Na-cations, (g) amount of CO_2 released at capsule opening, here given as percentage of the weighed starting material (subsection 2.1.6), (h) X_{H2O} calculated as molar $H_2O/(CO_2 + H_2O)$ as determined at the capsule opening (subsection 2.1.6), (*) higher uncertainties of ICP-OES analysis: R18-3, carb. melt: 10 %, R16-3, carb. melt: 7 %.

TABLE 3.7: Results of the chemical analyses and Mössbauer spectroscopy – KGW_{hAl}-series *(continued, 2/2)*

Experiment no.	R15-3						R13-4					
Temperature / Pressure / time	1200 °C / 0.7 GPa / 92 h						1100 °C / 0.7 GPa / 90 h					
	OES[a]	EDX	SD	WDX	SD	norm.[b]	OES[a]	EDX	SD	WDX	SD	norm.[b]
Silicate melt												
No. of analyses (EDX/WDX)				20				22		30		
SiO_2[c]	53.1			51.5	0.6	52.6	53.6	58.2	0.9	51.3	0.7	54.4
Al_2O_3	21.1			20.1	0.3	20.5	20.4	19.2	0.4	19.3	0.4	20.4
FeO	4.7			4.6	0.1	4.7	3.9	4.2	0.3	4.0	0.4	4.3
MgO	0.0	n. a.		0.0	0.0	0.0	0.0	0.0	0.0	0.0	0.0	0.0
CaO	0.4			0.3	0.0	0.3	0.2	0.0	0.0	0.2	0.1	0.2
Na_2O	20.7			21.4	0.6	21.9	21.6	18.3	0.9	19.6	0.4	20.8
CO_2[d]	-			2.2		-	-	-		5.6		-
Total	100.0			97.8	0.7	100.0	100.0	100.0		94.4	0.7	100.0
$Fe^{3+}/\Sigma Fe$	0.16						n. a.					
Na/Al	1.6						1.7					
ASI[e]	0.51						0.49					
n_{mod}/n_{form}[e]	0.25						0.27					
Carbonate melt												
No. of analyses (EDX)		19						4				
SiO_2[c]	*0.5*	0.1	0.2				0.8	0.0	0.0			
Al_2O_3	*0.2*	0.0	0.0				0.3	0.0	0.0			
FeO	*6.4*	5.2	3.7				6.4	5.3	2.6			
MgO	*0.0*	0.0	0.0		n. a.		0.0	0.0	0.0		n. a.	
CaO	*3.1*	1.9	2.7				2.7	2.5	1.3			
Na_2O	***48.7***	51.5	6.2				49.0	50.8	3.8			
CO_2[f]	*41.0*	41.3					40.8	41.3				
Total	100.0	100.0					100.0	100.0				
Volatile phase												
CO_2 (wt. %)[g]				3.1						2.6		
X_{H2O}[h]				0.1						0.1		

n.a. – not analyzed, SD – standard deviation, ***italics*** – minimum estimate where element exceeded the calibration range in OES analyses, (a) the typical uncertainty resulting from weighing, dilution, and ICP-OES analyses is 6%, (b) normalized without CO_2 for a better comparison of the methods, (c) SiO_2 of the ICP-OES analyses was recalculated from the Si/Fe ratio in the silicate glass (Si/Al in carbonate quench phase, resepctively) determined by WDX and EDX (subsection 2.3.2), (d) estimate of CO_2 content derived from difference to 100 % total of silicate glass WDX analyses, (e) ASI calculated as molar $Al_2O_3/CaO + Na_2O + FeO$, (f) CO_2 content of the carb. melt was recalculated as stoichiometric carbonate for all Fe-, Mg-, Ca- and Na-cations, (g) amount of CO_2 released at capsule opening, here given as percentage of the weighed starting material (subsection 2.1.6), (h) X_{H2O} calculated as molar $H_2O/(CO_2 + H_2O)$ as determined at the capsule opening (subsection 2.1.6).

TABLE 3.8: Results of the chemical analyses and Mössbauer spectroscopy – KGW_{lAl+Fe}-series

Experiment no.	R18-4			R16-4						R15-4					
Temperature / Pressure / time	1200 °C / 0.7 GPa / 3 h			1200 °C / 0.7 GPa / 50 h						1200 °C / 0.7 GPa / 92 h					
	OES[a, *]	EDX	WDX	OES[a, *]	EDX	SD	WDX	SD	norm.[b]	OES[a]	EDX	SD	WDX	SD	norm.[b]
Silicate melt															
No. of analyses (EDX/WDX)							20						20		
SiO_2[c]	*52.3*			*53.5*			53.0	0.5	55.3	54.0			52.7	0.9	55.0
Al_2O_3	*6.6*			*6.5*			7.0	0.1	7.3	6.7			6.9	0.1	7.2
FeO	*12.8*			*12.9*			12.8	0.2	13.3	13.5			13.2	0.3	13.7
MgO	*0.0*	n. a.	n. a.	*0.0*	n. a.		0.0	0.0	0.0	0.0	n. a.		0.0	0.0	0.0
CaO	*0.8*			*0.8*			0.6	0.1	0.6	0.9			0.7	0.1	0.8
Na_2O	***27.4***			***26.2***			22.5	0.6	23.5	24.7			22.4	0.5	23.3
CO_2[d]	-			-			4.0		-	-			4.1		-
Total	100.0			100.0			96.0	0.4	100.0	100.0			95.9	0.7	100.0
$Fe^{3+}/\Sigma Fe$	n. a.			n. a.						n. a.					
Na/Al	6.8			6.6						6.1					
ASI[e]	0.10			0.10						0.11					
n_{mod}/n_{form}[e]	0.95			0.89						0.85					
Carbonate melt	upper part	lower part													
No. of analyses (EDX)					25						13				
SiO_2[c]	1.8	1.7		0.8	0.0	0.1				1.0	0.2	0.3			
Al_2O_3	0.2	0.2		0.1	0.0	0.0				0.1	0.0	0.0			
FeO	8.1	8.0		7.3	10.5	1.0				7.9	3.1	1.4			
MgO	0.0	0.0	n. a.	0.0	0.0	0.0		n. a.		0.0	0.0	0.0		n. a.	
CaO	2.7	2.4		2.6	3.9	0.4				2.7	0.8	1.0			
Na_2O	46.8	47.3		48.3	44.5	1.2				47.5	54.6	2.6			
CO_2[f]	40.3	40.4		40.8	41.1					40.7	41.3				
Total	100.0	100.0		100.0	100.0					100.0	100.0				
Volatile phase															
CO_2 (wt. %)[g]		2.2					2.7						2.6		
X_{H2O}[h]		0.3					0.0						0.0		

n.a. – not analyzed, SD – standard deviation, ***italics*** – minimum estimate where element exceeded the calibration range in OES analyses, (a) the typical uncertainty resulting from weighing, dilution, and ICP-OES analyses is 6%, * mark higher uncertainties resulting from very small sample amounts, (b) normalized without CO_2 for a better comparison of the methods, (c) SiO_2 of the ICP-OES analyses was recalculated from the Si/Fe ratio in the silicate glass (Si/Al in carbonate quench phase, resepctively) determined by WDX and EDX (subsection 2.3.2), (d) estimate of CO_2 content derived from difference to 100 % total of silicate glass WDX analyses, (e) ASI calculated as molar $Al_2O_3/CaO + Na_2O + FeO$, (f) CO_2 content of the carb. melt was recalculated as stoichiometric carbonate for all Fe-, Mg-, Ca- and Na-cations, (g) amount of CO_2 released at capsule opening, here given as percentage of the weighed starting material (subsection 2.1.6), (h) X_{H2O} calculated as molar $H_2O/(CO_2 + H_2O)$ as determined at the capsule opening (subsection 2.1.6), (*) higher uncertainties of ICP-OES analysis: R18-4, carb. melt upper part: 20 %, lower part: 9 %, R16-4, carb. melt: 16 %.

TABLE 3.9: Results of the chemical analyses and Mössbauer spectroscopy – KGW_{1Al+Ca}-series

Experiment no.	R185			R165					
Temperature / Pressure / time	1200 °C / 0.7 GPa / 3 h			1200 °C / 0.7 GPa / 50 h					
	OES[a]	EDX	WDX	OES[a]	EDX	SD	WDX	SD	norm.[b]
Silicate melt									
No. of analyses (EDX/WDX)							19		
SiO_2[c]	*54.8*			52.7			53.7	0.6	56.4
Al_2O_3	*7.2*			6.6			7.2	0.1	7.5
FeO	*8.1*			7.8			7.9	0.2	8.3
MgO	*0.0*	n. a.	n. a.	0.0	n. a.		0.0	0.0	0.0
CaO	*6.2*			7.1			5.1	0.3	5.3
Na_2O	***23.7***			25.8			21.4	0.5	22.4
CO_2[d]	-			-			4.7		-
Total	100.0			100.0			95.3	0.5	100.0
$Fe^{3+}/\Sigma Fe$	n. a.			n. a.					
Na/Al	5.4			6.5					
ASI[e]	0.12			0.10					
n_{mod}/n_{form}[e]	0.81			0.93					
Carbonate melt	light color	dark color		upper part	lower part				
No. of analyses (EDX)						10			
SiO_2[c]	*0.7*	*0.8*		*0.7*	1.2	1.9	3.2		
Al_2O_3	*0.1*	*0.1*		*0.1*	0.2	0.0	0.0		
FeO	*3.1*	*3.1*		*3.0*	3.2	4.3	0.7		
MgO	*0.0*	*0.0*	n. a.	n. a.	*0.0*	0.0	0.0	0.0	n. a.
CaO	*14.7*	*14.2*			*13.8*	16.4	21.0	1.4	
Na_2O	***39.8***	***40.3***			***40.7***	37.5	31.4	1.6	
CO_2[f]	*41.7*	*41.6*			*41.6*	41.5	41.4		
Total	100.0	100.0			100.0	100.0	100.0		
Volatile phase									
CO_2 (wt. %)[g]		3.3				1.3			
X_{H2O}[h]		0.2				0.8			

n.a. – not analyzed, SD – standard deviation, ***italics*** – minimum estimate where element exceeded the calibration range in OES analyses, (a) the typical uncertainty resulting from weighing, dilution, and ICP-OES analyses is 6%, (b) normalized without CO_2 for a better comparison of the methods, (c) SiO_2 of the ICP-OES analyses was recalculated from the Si/Fe ratio in the silicate glass (Si/Al in carbonate quench phase, resepctively) determined by WDX and EDX (subsection 2.3.2), (d) estimate of CO_2 content derived from difference to 100 % total of silicate glass WDX analyses, (e) ASI calculated as molar $Al_2O_3/CaO + Na_2O + FeO$, (f) CO_2 content of the carb. melt was recalculated as stoichiometric carbonate for all Fe-, Mg-, Ca- and Na-cations, (g) amount of CO_2 released at capsule opening, here given as percentage of the weighed starting material (subsection 2.1.6), (h) X_{H2O} calculated as molar $H_2O/(CO_2 + H_2O)$ as determined at the capsule opening (subsection 2.1.6).

3.2.2 Results of Mössbauer spectroscopy

Three samples of different chemical compositions (R16-1 BR, R13-3 KGW_{lAl}, R15-3 KGW_{hAl}) were selected for Mössbauer spectroscopy. From each of these samples, only the silicate glasses could be analyzed by Mössbauer spectroscopy. The cryptocrystalline quench products of the corresponding carbonate melts were not suitable for Mössbauer spectroscopy. The resulting $Fe^{3+}/\Sigma Fe$, hyperfine parameters, and site assignments made are presented in Table 3.10.

The silicate glasses of samples R13-3 (KGW_{lAl}) and R15-3 (KGW_{hAl}), similar in chemistry and f_{O2}, show rather similar Mössbauer spectra. The silicate glass of sample R16-1 (BR), of distinct composition and synthesized at more oxidizing conditions, has a distinct Mössbauer spectrum. The absorption spectra of all three samples are typical Mössbauer spectra of glasses (e. g. Borisov and McCammon, 2010) consisting of two broad main bands, with a shoulder attached to the band in the lower velocity region. In the spectra of samples R13-3 (KGW_{lAl}) and R15-3 (KGW_{hAl}) weak additional absorption occurs in the higher velocity region. The spectrum of sample R16-1 (BR) could be fitted by two doublets with a larger and a smaller quadrupole splitting, assigned to Fe^{2+} and Fe^{3+}, respectively (Figure 3.6, a). To fit the spectra of the samples R13-3 (KGW_{lAl}) and R15-3 (KGW_{hAl}), a third doublet was added and assigned to Fe^{2+}, due to its large quadrupole splitting (Figure 3.6, b). $Fe^{3+}/\Sigma Fe$ of all three glasses was determined from the relative areas, values are given in Table 3.10. The ferrous iron content is higher in the silicate glasses synthesized under more reducing conditions, which corresponds with observations on silicate glasses by e. g. McCanta et al. (2004).

TABLE 3.10: Hyperfine parameters and $Fe^{3+}/\Sigma Fe$ in silicate glasses determined from Mössbauer spectroscopy measurements

Sample	Assigned iron species	Quadrupol splitting [mm/s]	error	Centre shift [mm/s]	error	Site assignments	FWHM [mm/s]	error	$Fe^{3+}/\Sigma Fe$
BR	Fe^{3+}	0.810	0.621	0.339	0.323	IV	0.657	0.053	0.24 ± 0.03
R16-1	Fe^{2+}	1.995	0.223	1.008	0.115	V/VI	0.194	-	
KGW_{lAl}	Fe^{3+}	0.801	0.135	0.278	0.081	IV	0.460	0.181	0.12 ± 0.05
R13-3	Fe^{2+}	1.276	0.635	0.916	0.204	IV/V	0.981	0.480	
	Fe^{2+}	2.072	0.051	1.032	0.025	V/VI	0.194	-	
KGW_{hAl}	Fe^{3+}	0.927	0.276	0.335	0.136	IV	0.492	0.144	0.16 ± 0.05
R15-3	Fe^{2+}	1.009	0.214	0.932	0.069	IV/V	0.439	0.182	
	Fe^{2+}	2.009	0.276	1.002	0.023	V/VI	0.194	-	

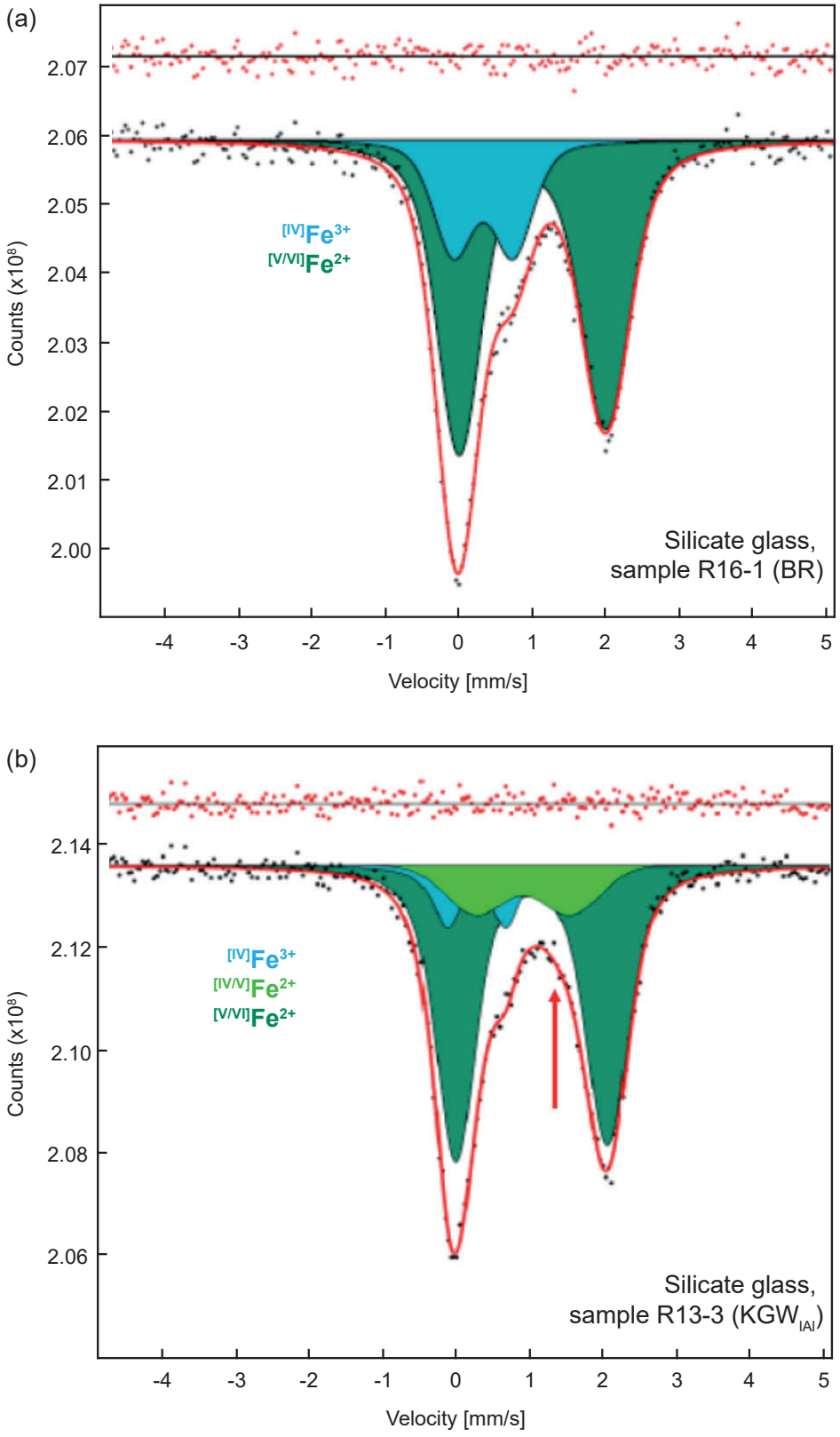

FIGURE 3.6: Mössbauer spectra of the silicate glasses of a) sample R16-1 (BR, more oxidizing conditions) and b) sample R13-3 (KGW_{IAI}, more reducing). The spectra have similar shapes. In sample R13-3 a weak additional absorption occurs in the high velocity region (red arrow). The fitted doublets are assigned as Fe^{3+} (blue), $^{[VI/V]}Fe^{2+}$ (dark green), and $^{[V/VI]}Fe^{2+}$ (light green).

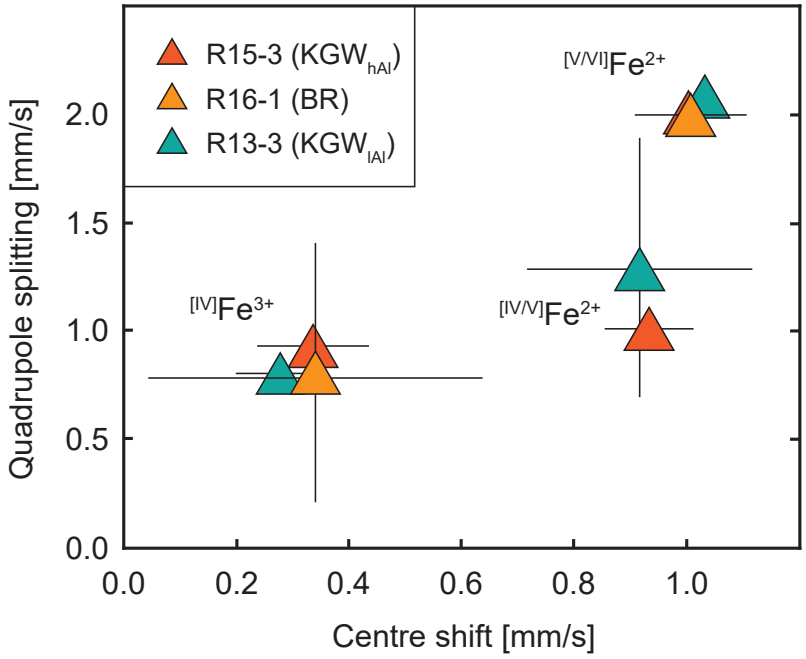

FIGURE 3.7: Overview of hyperfine parameters provided by quadrupole splitting vs. centre shift derived from Mössbauer spectra of silicate glass run products. The site assignments made are based on the centre shift values (see Table 3.11).

Site assignments were made based on centre shift values (Dyar, 1985, see Table 3.11). As illustrated in Figure 3.6, ferric iron in all three glasses is accommodated in similar environments with a predominantly 4-fold coordination, ferrous iron is 5- to 6-fold coordinated. In samples R13-3 (KGW$_{lAl}$) and R15-3 (KGW$_{hAl}$) an additional Fe^{2+} environment with a lower 4- to 5-fold coordination occurs.

TABLE 3.11: Range of centre shifts in Mössbauerspectra of phosphate, borate, and silicate glasses (from Dyar, 1985)

Iron environment	Centre shift* [mm/s]
$^{[VIII]}Fe^{2+}$	1.20 - 1.30
$^{[VI]}Fe^{2+}$	1.05 - 1.10
$^{[IV]}Fe^{2+}$	0.90 - 0.95
$^{[VI]}Fe^{3+}$	0.35 - 0.55
$^{[IV]}Fe^{3+}$	0.20 - 0.32

* relative to alpha-Fe

3.3 Iron isotope analyses of the kinetic and equilibration experiments

Time series equilibration experiments with different chemical compositions in the carbonatite system Na_2O-SiO_2-Al_2O_3-CaO-(MgO)-Fe_2O_3-(FeO)-CO_2 were performed to investigate the iron isotope fractionation between silicate and carbonate immiscible melts and to determine the correspondent equilibrium iron isotope fractionation between silicate melt and carbonate melt.

First it was evaluated whether chemical and iron isotopic equilibria were achieved during experimental runs. This was assessed not only by time series and analyses of δ^{56}Fe of the equilibration experiments, but also by additional experiments employing a silicate glass, artificially enriched in ^{58}Fe. This allows to monitor the kinetics of iron isotope exchange between the two phases (as described in subsection 2.1.2). The results of the kinetic experiments (δ^{58}Fe) are reported in subsection 3.3.1, the results of the time series equilibration experiments (δ^{56}Fe) are reported in subsection 3.3.2.

Evidence for chemical and isotopic equilibria is discussed in section 4.2. The conclusion that chemical and isotopic equilibria are reached in experiments with $\geq$ three hours run time is used here to calculate the mean $\Delta^{56}Fe_{\text{sil. m.-carb. m.}}$ of the equilibration experiments (subsection 3.3.1, subsection 3.3.2).

3.3.1 Results of the kinetic experiments (Sp-series)

The results of the kinetic experiments are presented in Table 3.12, Figure 3.8 (δ^{58}Fe values), and Figure 3.9 (δ^{56}Fe values), respectively. Figure 3.8 shows the fast decrease of δ^{58}Fe in the silicate phase due to iron isotopic exchange with the carbonate phase. In the carbonate phase the δ^{58}Fe increases correspondingly. Within three hours, both phases reach the equilibrium isotopic value of the system (δ^{58}Fe = 209 ‰). The equilibrium isotopic value of the system is defined by the calculated bulk isotope value of both the silicate and the carbonate melt, where any mass-dependent isotope fractionation is negligible in this system artificially enriched in ^{58}Fe. The approach of the system to isotopic equilibrium can be described by

$$F(\delta) = \frac{\delta^{58}Fe_{runtime} - \delta^{58}Fe_{initial}}{\delta^{58}Fe_{equilibrium} - \delta^{58}Fe_{initial}} \tag{3.1}$$

where $\delta^{58}Fe_{\text{initial}}$ and $\delta^{58}Fe_{\text{equilibrium}}$ are isotopic compositions of one starting material and of the same phase after full equilibration of the system, and $\delta^{58}Fe_{\text{runtime}}$ is the isotopic composition of the phase measured after a given runtime of the experiment (e. g. Johnson et al., 2004 and references therein). In this expression, $F = 0$ at the beginning of the

reaction, and $F = 1$ when the iron isotopic equilibrium value of the system is reached. In the investigated carbonatite system, iron isotopic equilibrium ($F \approx 1$) is reached after a runtime of 3 hours.

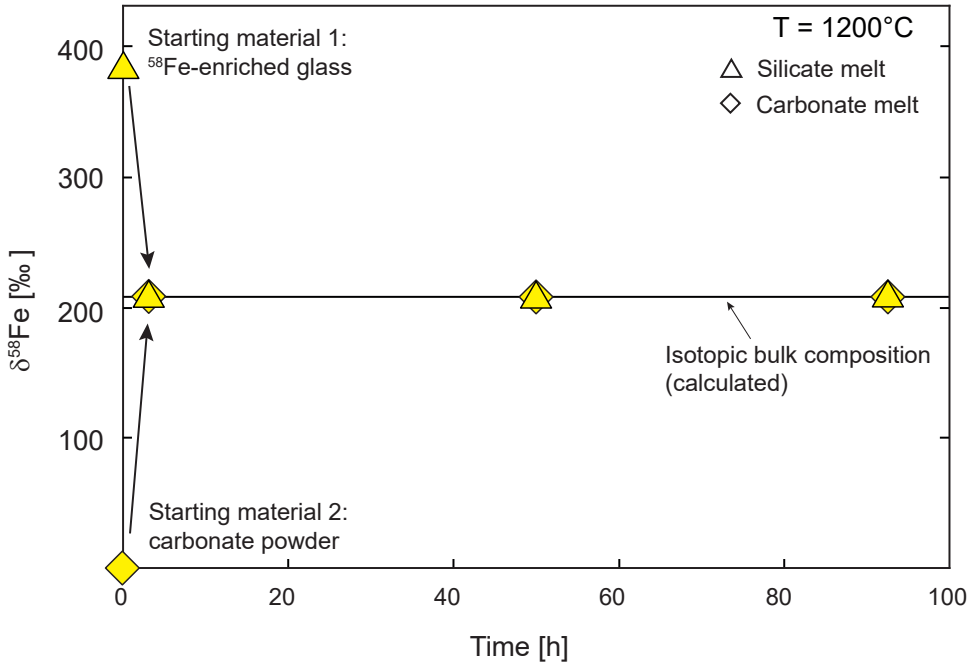

FIGURE 3.8: Results of the kinetic iron isotope exchange experiments show a fast approach toward the equilibrium iron isotopic value of the system (horizontal line) from both sides.

TABLE 3.12: Results of the kinetic iron isotope exchange experiments – Sp-series

Experiment no.	Temperature [C°]	Pressure [GPa]	Duration [h]	Analyzed iron bearing phase	δ^{56}Fe [‰]	2SD	δ^{57}Fe [‰]	2SD	δ^{58}Fe [‰]	2SD	n_{meas}	$\Delta^{56}Fe_{sil.\,m.-carb.\,m.}$ [‰]	± *1	$\Delta^{56}Fe_{sil.\,m.-carb.\,m.}$ (mean) [‰]*2	2SD	F
Starting material Sp1														*Run time ≥ 3 hours*		
R14-5	1200	0.7	2	Sil. melt	0.07	0.04	0.10	0.08	n. d.		4			0.09	0.04	
				Carb. melt	0.01	0.04	0.02	0.12	n. d.		4	0.06	0.07	(n_{exp} = 5)		
R14-6	1200	0.7	2	Sil. melt	0.10	0.07	0.15	0.11	n. d.		4					
				Carb. melt	0.05	0.04	0.06	0.06	n. d.		4	0.05	0.08			
Starting material Sp2/3																
R18-6	1200	0.7	3	Sil. melt	0.05	0.03	0.11	0.07	209.37	0.62	4					
				Carb. melt	-0.06	0.05	-0.05	0.05	209.07	0.09	4	0.11	0.07			1.00
R18-7	1200	0.7	3	Sil. melt	0.07	0.02	0.14	0.01	207.73	0.08	4					
				Carb. melt	0.00	0.02	0.01	0.04	208.25	0.29	4	0.07	0.07			1.01
R16-6	1200	0.7	51	Sil. melt	0.13	0.04	0.22	0.10	209.50	1.25	3					
				Carb. melt	0.03	0.02	0.08	0.06	209.02	1.11	4	0.10	0.07			1.00
R15-5	1200	0.7	93	Sil. melt	0.28	0.04	0.45	0.07	209.37	0.87	4					
				Carb. melt	0.19	0.05	0.32	0.08	209.07	0.12	4	0.09	0.07			1.00
R15-6	1200	0.7	93	Sil. melt	0.07	0.04	0.14	0.09	208.10	0.51	4					
				Carb. melt	0.01	0.04	0.03	0.06	208.32	0.40	4	0.07	0.07			1.01

n. d. – not determined, n_{meas} – measurement replicates, n_{exp} – replicates of the experiment (as described in subsection 3.3.2). (*1) Uncertainties on $\Delta^{56}Fe_{sil.\,m.-carb.\,m.}$ are the error propagated analytical uncertainties of the method on δ^{56}Fe (s. subsection 2.3.4), exept for samples with exceptionally high (>0.07) measurement uncertainties. For these, uncertainties on $\Delta^{56}Fe_{sil.\,m.-carb.\,m.}$ are the error propagated measurement uncertainties. (*2) See subsection 3.3.2.

3.3.2 Results of iron isotope analyses of the equilibration experiments

Iron isotope fractionation between silicate and carbonate immiscible melts was investigated by equilibration experiments, mostly performed at a temperature of 1200 °C and a pressure of 0.7 GPa. Run times in these experiments were between 2 and ~ 90 hours, to monitor the phases reaching and remaining in chemical and isotopic equilibrium. Additional information was gained from runs at temperatures of 1100 °C and 900 °C and from one run at a lower pressure (0.5 GPa). At 1100 °C and 900 °C no kinetic experiments were performed, hence the timescale for isotopic equilibration remains unknown. However, at runtimes of ≥ 24 hours, isotopic equilibrium is likely attained, based on the fast exchange kinetics observed at 1200 °C. The equilibrium iron isotope fractionation factor between silicate and carbonate melts $\alpha_{\text{sil. m.-carb. m.}}$ could thus be approximated conveniently as

$$\alpha_{\text{sil. m.-carb. m.}} \approx \Delta^{56}Fe_{\text{sil. m.-carb. m.}} = \delta^{56}Fe_{\text{sil. m.}} - \delta^{56}Fe_{\text{carb. m.}} \quad (3.2)$$

The results of iron isotope analyses of the experiments are reported in Table 3.13 (equilibration experiments) and Table 3.12 (kinetic experiments, in subsection 3.3.1).

In Figure 3.9, δ^{56}Fe of both silicate and carbonate melt and $\Delta^{56}\text{Fe}_{\text{sil. m.-carb. m.}}$ are plotted against run durations. Within the analytical uncertainty of the method (± 0.05 ‰ 2SD), $\Delta^{56}\text{Fe}_{\text{sil. m.-carb. m.}}$ remained stable at runtimes from 2 to ~ 90 hours in all of the systems. All $\Delta^{56}\text{Fe}_{\text{sil. m.-carb. m.}}$ of experiments with run durations longer than two hours are assumed to represent equilibrium isotope fractionation (as discussed in section 4.2). The two key observations from experiments in iron isotopic equilibrium are:

- Iron isotope fractionations in the temperature range of 900 °C to 1200 °C between silicate and carbonate melts in the investigated systems are at the limit of being analytically resolvable. Since the analytical uncertainty of the iron isotope analyses is ± 0.05 ‰ (2 SD) on δ^{56}Fe, a difference in iron isotopic composition between silicate and carbonate melt can only be resolved if $\Delta^{56}\text{Fe}_{\text{sil. m.-carb. m.}} > 0.1$ ‰. This is the case in the three systems with strongly peralkaline compositions of the silicate melts (ASI of 0.19 to 0.51), yet not in each sample (see Figure 3.9). The strongest fractionation at 1200 °C occurred in the system BR ($\Delta^{56}\text{Fe}_{\text{sil. m.-carb. m.}}$ ranging from 0.10 to 0.15 ‰), while $\Delta^{56}\text{Fe}_{\text{sil. m.-carb. m.}}$ varied between 0.02 ‰ (analytically not resolvable) and 0.12 ‰ in system KGW_{hAl} and 0.07 ‰ (analytically not resolvable) and 0.11 ‰ in system Sp, respectively. In the three extremely peralkaline systems (ASI of 0.11 to 0.14), iron isotope fractionation cannot be analytically resolved ($\Delta^{56}\text{Fe}_{\text{sil. m.-carb. m.}}$ between – 0.02 ‰ and + 0.08 ‰).

- In all systems that showed fractionation, the carbonate melt was enriched in light iron isotopes.

Quality of the experimental data

Iron isotopic bulk compositions of the samples were re-calculated from the measured δ^{56}Fe of the silicate and the carbonate melt, respectively. Usually these calculated bulk compositions agreed with the measured iron isotopic bulk compositions of the starting materials within analytical uncertainty. In samples R16-3 and R15-3 (system hAl) and samples R16-6 and R15-5 (system Sp), the re-calculated bulk compositions are heavier than the starting material, implying a loss of light iron isotopes, most likely due to small cracks in the Re-foil. The main concern about iron loss to a third reservoir is an unmonitored kinetic reaction that would disturb the iron isotopic equilibration. Yet, all affected samples still reproduce the $\Delta^{56}Fe_{sil.m.\text{-}carb.m.}$ measured in equilibrated samples of the same time series. Taking into account that $\Delta^{56}Fe_{sil.m.\text{-}carb.m.}$ is independent of the absolute values, all values were considered reliable for further evaluation.

In some samples, the carbonate melt was sampled multiple times at different positions in the capsule, distinguishing between the upper and the lower part of carbonate melt, or between lighter and darker colored sections. In all cases, the measured δ^{56}Fe were the same within analytical uncertainty, hence no isotopic heterogeneity within the carbonate phase in a given capsule was detected. Still, a tendency to larger iron isotopic fractionations between the sampled spots of the carbonate melt for shorter run time and especially in the 2 hour runs was observed. The silicate melt was not probed for iron isotopic heterogeneity within the phase.

Mean $\Delta^{56}Fe_{sil.m.\text{-}carb.m.}$, standard deviation (SD), and standard error of the mean (SE) were calculated from $\Delta^{56}Fe_{sil.m.\text{-}carb.m.}$ of experiments of the same P-T-conditions (P = 0.7 GPa, T = 1200 °C) and are given in Table 3.13 (equilibration experiments) and Table 3.12 (kinetic experiments, in subsection 3.3.1), respectively. Very short runs of two hours run time were excluded from this calculation due to possible local inhomogeneities when equilibrium was not yet achieved. In cases where two samples were taken from one carbonate melt, an unweighted average of the two $\Delta^{56}Fe_{sil.m.\text{-}carb.m.}$ of each sample was used in the calculation. The overall repeatability of the experimental procedure from preparing the capsules to iron isotope analyses of the run products was between ± 0.04 ‰ (2 SD) and ± 0.09 ‰ (2 SD).

TABLE 3.13: Results of the equilibration iron isotope exchange experiments *1/4*

Experiment No.	Temperature [C°]	Pressure [GPa]	Duration [h]	Analyzed iron bearing phase	δ^{56}Fe [‰]	2SD	δ^{57}Fe [‰]	2SD	n_{meas}	$\Delta^{56}Fe_{sil.\,m.\text{-}carb.\,m.}$ [‰]	± *1	$\Delta^{56}Fe_{sil.\,m.\text{-}carb.\,m.}$ mean [‰]*2	2SD
Starting material BR												*Run time ≥ 3 hours*	
R14-1	1200	0.7	2	Sil. m.	-0.21	0.04	-0.31	0.06	8				
				Carb. $m._{dark}$	-0.34	0.02	-0.51	0.05	4	0.13	0.07	0.13	0.04
				Carb. $m._{light}$	-0.33	0.03	-0.50	0.08	4	0.12	0.07	(n_{exp} = 3)	
R14-2	1200	0.7	2	Sil. m.	-0.25	0.03	-0.37	0.06	4				
				Carb. $m._{dark}$	-0.28	0.07	-0.41	0.10	4	0.03	0.08		
				Carb. $m._{light}$	-0.36	0.03	-0.54	0.09	4	0.11	0.07		
R80-5	1200	0.5	23	Sil. m.	-0.24	0.04	-0.30	0.31	3	0.07	0.07		
				Carb. m.	-0.31	0.03	-0.45	0.03	4				
R09-1	1200	0.7	42	Sil. m.	-0.24	0.03	-0.37	0.05	2	0.14	0.07		
				Carb. m.	-0.37	0.03	-0.57	0.07	4				
R16-1	1200	0.7	51	Sil. m.	-0.22	0.03	-0.33	0.06	4	0.15	0.07		
				Carb. m.	-0.37	0.05	-0.54	0.04	4				
R15-1	1200	0.7	93	Sil. m.	-0.29	0.05	-0.44	0.08	4	0.10	0.07		
				Carb. m.	-0.39	0.02	-0.59	0.10	4				
R11-2	1100	0.7	45	Sil. m.	-0.20	0.03	-0.30	0.06	4	0.08	0.07		
				Carb. m.	-0.28	0.02	-0.42	0.02	4				
R13-1	1100	0.7	91	Sil. m.	-0.18	0.04	-0.26	0.07	4	0.22	0.07		
				Carb. m.	-0.40	0.04	-0.57	0.03	4				

n_{meas} – measurement replicates, n_{exp} – replicates of the experiment (as described in subsection 3.3.2). (*1) Uncertainties on $\Delta^{56}Fe_{sil.\,m.\text{-}carb.\,m.}$ are the error propagated analytical uncertainties of the method on δ^{56}Fe (s. subsection 2.3.4), exept for samples with exceptionally high (> 0.07 ‰) measurement uncertainties. For these, uncertainties on $\Delta^{56}Fe_{sil.\,m.\text{-}carb.\,m.}$ are the error propagated measurement uncertainties. (*2) See subsection 3.3.2.

TABLE 3.13: Results of the equilibration iron isotope exchange experiments (*continued, 2/4*)

Experiment No.	Temperature [C°]	Pressure [GPa]	Duration [h]	Analyzed iron bearing phase	δ^{56}Fe [‰]	2SD	δ^{57}Fe [‰]	2SD	n_{meas}	$\Delta^{56}Fe_{sil.\,m.\text{-}carb.\,m.}$ [‰]	± *1	$\Delta^{56}Fe_{sil.\,m.\text{-}carb.\,m.}$ mean [‰]*2	2SD
Starting material KGW lAl												*Run time ≥ 3 hours*	
R14-3	1200	0.7	2	Sil. m.	-0.28	0.03	-0.42	0.06	4	-0.01	0.07	0.05	0.09
				Carb. $m._{upper\ part}$	-0.27	0.05	-0.42	0.09	4			(n_{exp}=2)	
R18-2	1200	0.7	3	Sil. m.	-0.27	0.04	-0.41	0.05	4	0.02	0.07		
				Carb. m.	-0.29	0.01	-0.43	0.06	4				
R16-2	1200	0.71	50.5	Sil. m.	-0.24	0.02	-0.38	0.13	4	0.08	0.07		
				Carb. m.	-0.33	0.05	-0.52	0.06	4				
R13-3	1100	0.7	90.5	Sil. m.	-0.29	0.04	-0.44	0.08	4	-0.01	0.07		
				Carb. m.	-0.28	0.04	-0.45	0.03	4				
R17-1	900	0.7	91	Sil. m.	-0.23	0.03	-0.31	0.10	4	0.09	0.07		
				Carb. m.	-0.32	0.03	-0.48	0.03	4				

n_{meas} – measurement replicates, n_{exp} – replicates of the experiment (as described in subsection 3.3.2). (*1) Uncertainties on $\Delta^{56}Fe_{sil.\,m.\text{-}carb.\,m.}$ are the error propagated analytical uncertainties of the method on δ^{56}Fe (s. subsection 2.3.4), exept for samples with exceptionally high (>0.07‰) measurement uncertainties. For these, uncertainties on $\Delta^{56}Fe_{sil.\,m.\text{-}carb.\,m.}$ are the error propagated measurement uncertainties. (*2) See subsection 3.3.2.

TABLE 3.13: Results of the equilibration iron isotope exchange experiments (*continued, 3/4*)

Experiment No.	Temperature [C°]	Pressure [GPa]	Duration [h]	Analyzed iron bearing phase	δ^{56}Fe [‰]	2SD	δ^{57}Fe [‰]	2SD	n_{meas}	$\Delta^{56}Fe_{sil.\,m.\text{-}carb.\,m.}$ [‰]	±*1	$\Delta^{56}Fe_{sil.\,m.\text{-}carb.\,m.}$ mean [‰]*2	2SD
Starting material KGW hAl												*Run time ≥ 3 hours*	
R14-4	1200	0.7	2	Sil. m.	-0.24	0.05	-0.36	0.11	4			0.08	0.06
				Carb. m.	-0.24	0.01	-0.32	0.06	3	-0.01	0.07	(n_{exp} = 3)	
R18-3	1200	0.7	3	Sil. m.	-0.26	0.04	-0.39	0.09	4				
				$Carb.\,m._{dark}$	-0.34	0.04	-0.50	0.07	4	0.08	0.07		
				$Carb.\,m._{light}$	-0.28	0.05	-0.41	0.06	4	0.02	0.07		
R16-3	1200	0.71	50.5	Sil. m.	-0.12	0.01	-0.21	0.04	4				
				$Carb.\,m._{upper\,part}$	-0.22	0.03	-0.32	0.01	4	0.09	0.07		
				$Carb.\,m._{lower\,part}$	-0.19	0.03	-0.26	0.07	4	0.06	0.07		
R15-3	1200	0.71	92.5	Sil. m.	-0.11	0.04	-0.20	0.06	4				
				Carb. m.	-0.23	0.03	-0.39	0.07	4	0.12	0.07		
R13-4	1100	0.7	90.5	Sil. m.	-0.20	0.06	-0.30	0.11	4				
				Carb. m.	-0.32	0.02	-0.50	0.03	4	0.12	0.07		

n_{meas} – measurement replicates, n_{exp} – replicates of the experiment (as described in subsection 3.3.2). (*1) Uncertainties on $\Delta^{56}Fe_{sil.\,m.\text{-}carb.\,m.}$ are the error propagated analytical uncertainties of the method on δ^{56}Fe (s. subsection 2.3.4), exept for samples with exceptionally high (>0.07‰) measurement uncertainties. For these, uncertainties on $\Delta^{56}Fe_{sil.\,m.\text{-}carb.\,m.}$ are the error propagated measurement uncertainties. (*2) See subsection 3.3.2.

TABLE 3.13: Results of the equilibration iron isotope exchange experiments (*continued, 4/4*)

Experiment No.	Temperature [C°]	Pressure [GPa]	Duration [h]	Analyzed iron bearing phase	$\delta^{56}Fe$ [‰]	2SD	$\delta^{57}Fe$ [‰]	2SD	n_{meas}	$\Delta^{56}Fe_{sil.\,m.\text{-}carb.\,m.}$ [‰]	± *1	$\Delta^{56}Fe_{sil.\,m.\text{-}carb.\,m.}$ mean [‰]*2	2SD
Starting material $KGW_{lAl + Fe}$												*Run time ≥ 3 hours*	
R18-4	1200	0.7	3	Sil. m.	-0.26	0.03	- 0.39	0.07	4			0.01	0.08
				Carb. $m._{upper\ part}$	-0.33	0.00	- 0.50	0.05	4	0.08	0.07	(n_{exp} = 3)	
				Carb. $m._{lower\ part}$	-0.28	0.05	- 0.41	0.08	4	0.02	0.07		
R16-4	1200	0.71	50.5	Sil. m.	-0.25	0.03	- 0.38	0.05	4				
				Carb. m.	-0.23	0.06	- 0.32	0.08	4	-0.02	0.07		
R15-4	1200	0.71	92.5	Sil. m.	-0.26	0.04	- 0.45	0.08	4				
				Carb. m.	-0.25	0.07	- 0.39	0.13	4	-0.01	0.08		
Starting material $KGW_{lAl + Ca}$												*Run time ≥ 3 hours*	
R18-5	1200	0.7	3	Sil. m.	-0.23	0.01	-0.34	0.02	4			0.03	0.04
				Carb. $m._{dark}$	-0.27	0.02	-0.40	0.07	4	0.04	0.07	(n_{exp} = 2)	
				Carb. $m._{light}$	-0.28	0.04	-0.40	0.03	4	0.04	0.07		
R16-5	1200	0.71	50.5	Sil. m.	-0.25	0.02	-0.37	0.07	4				
				Carb. $m._{upper\ part}$	-0.27	0.04	-0.43	0.02	4	0.02	0.07		
				Carb. $m._{lower\ part}$	-0.25	0.03	-0.38	0.10	4	0.00	0.07		

n_{meas} – measurement replicates, n_{exp} – replicates of the experiment (as described in subsection 3.3.2). (*1) Uncertainties on $\Delta^{56}Fe_{sil.\,m.\text{-}carb.\,m.}$ are the error propagated analytical uncertainties of the method on $\delta^{56}Fe$ (s. subsection 2.3.4), exept for samples with exceptionally high (>0.07‰) measurement uncertainties. For these, uncertainties on $\Delta^{56}Fe_{sil.\,m.\text{-}carb.\,m.}$ are the error propagated measurement uncertainties. (*2) See subsection 3.3.2.

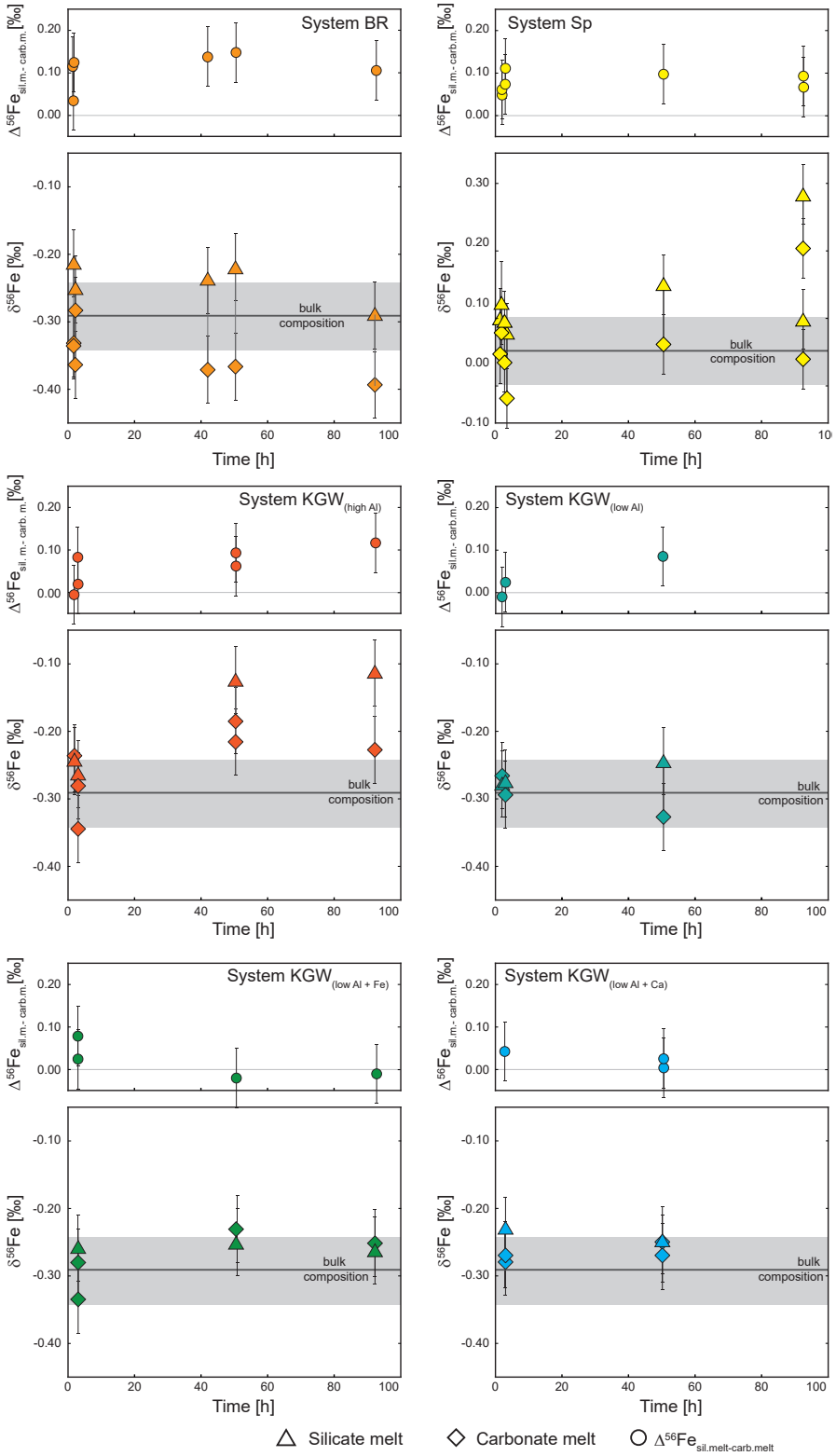

FIGURE 3.9: Results of iron isotope analyses of the equilibration experiments at $T = 1200\,°C$ and $P = 0.7\,GPa$, plotted as time series of $\delta^{56}Fe$ and $\Delta^{56}Fe$. Horizontal lines in the plots of $\delta^{56}Fe$ indicate the bulk isotopic composition of the system, (starting composition), the grey bars indicate the analytical uncertainty of 0.05 ‰. Uncertainties on the $\Delta^{56}Fe$ are the error propagated analytical uncertainties of the method on $\delta^{56}Fe$, except for samples with measurement uncertainties > 0.07 ‰. For these, uncertainties on $\Delta^{56}Fe_{sil.\,m.\text{-}carb.\,m.}$ are the error propagated measurement uncertainties.

Pressure and temperature

An influence of pressure (0.5 GPa and 0.7 GPa) or temperature (in the range of 900 °C to 1200 °C at 0.7 GPa) on iron isotope fractionation could not be resolved in this study. At a pressure of 0.5 GPa a fratiionation of $\Delta^{56}Fe_{sil.m.-carb.m.}$ = 0.08 ‰ (± 0.07 ‰, 2 SD) was measured in system BR (Table 3.13, Figure 3.10), which is, within the analytical uncertainty, the same as at 0.7 GPa. $\Delta^{56}Fe_{sil.m.-carb.m.}$ measured at lower temperatures (1100 °C in the systems BR, KGW_{lAl} and KGW_{hAl} and 900 °C in system KGW_{lAl}) were also indistinguishable from $\Delta^{56}Fe_{sil.m.-carb.m.}$ at 1200 °C within analytical uncertainty (Table 3.13, Figure 3.11). The highest value of $\Delta^{56}Fe_{sil.m.-carb.m.}$ measured in this study was 0.22 ‰ (± 0.07 ‰, 2 SD) in system BR at 1100 °C.

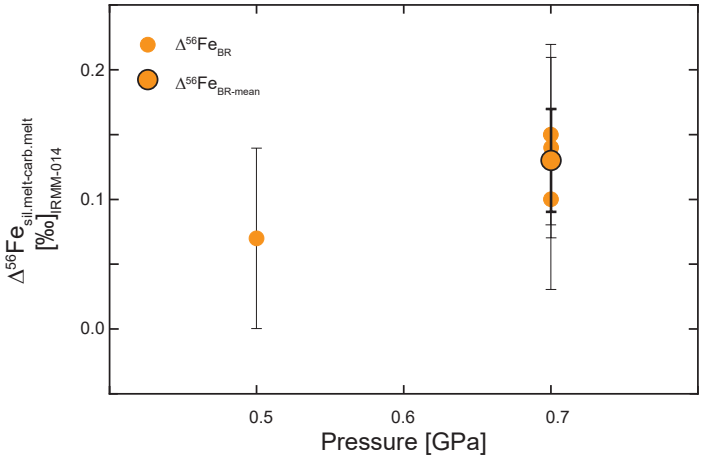

FIGURE 3.10: $\Delta^{56}Fe$ vs. P at a temperature of 1200 °C, system BR. Within analytical uncertainty the magnitude of iron isotope fractionation is the same. Circles without rim represent single experiments, while the rimmed circle represents the mean $\Delta^{56}Fe$ of the experiments at 0.7 GPa.

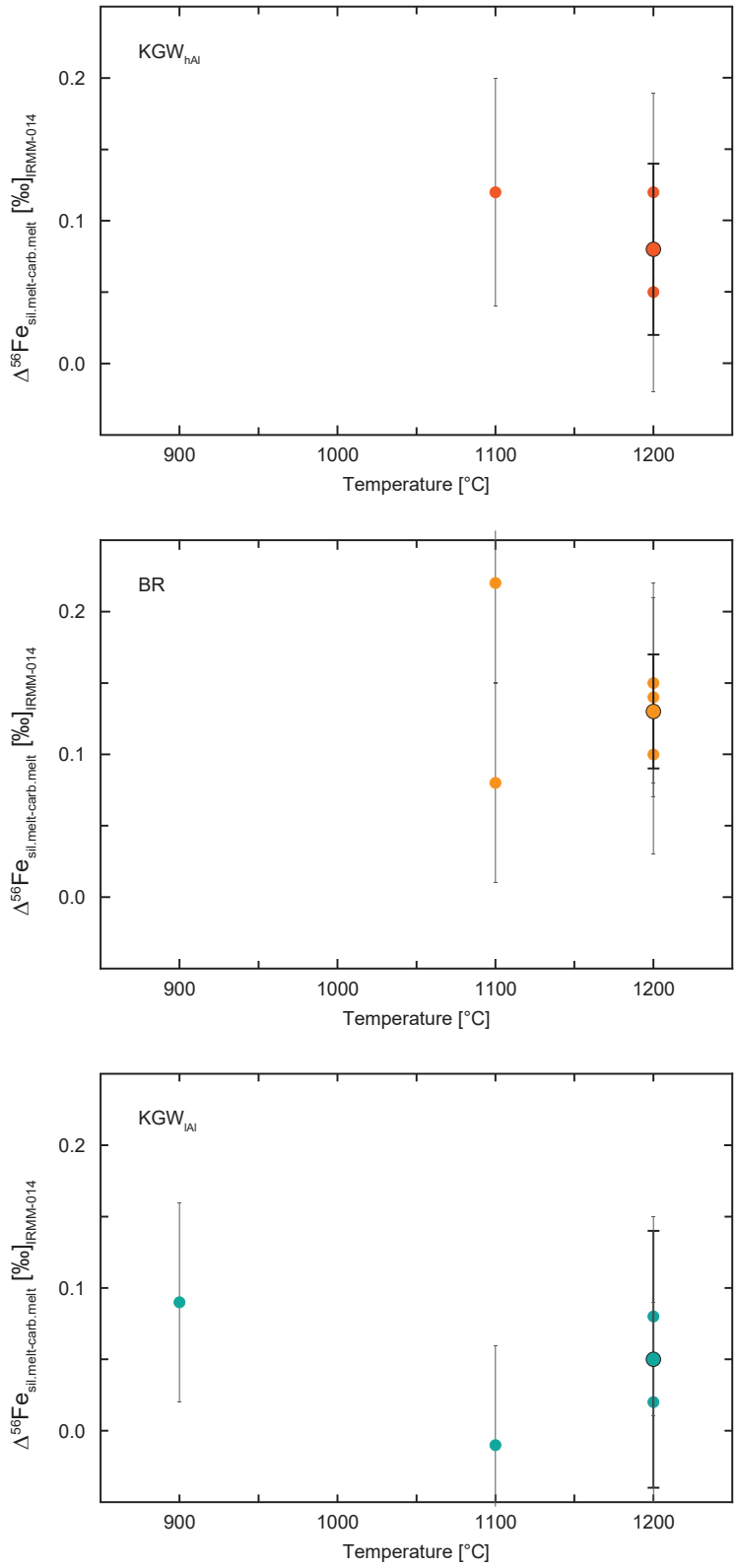

FIGURE 3.11: Δ^{56}Fe vs. T at a pressure of 0.7 GPa, systems KGW$_{highAl}$, BR, and KGW$_{lowAl}$. Circles without rim represent single experiments, while the rimmed circles represent the mean Δ^{56}Fe of the experiments at 0.7 GPa.

Redox and composition

In Figure 3.12, the $\Delta^{56}Fe_{sil.m.-carb.m.}$ of the three silicate glasses investigated by Mössbauer spectroscopy are plotted against the determined $Fe^{3+}/\Sigma Fe$. Iron isotope fractionation between silicate and carbonate melt correlates with $Fe^{3+}/\Sigma Fe$ in the silicate glasses: $\Delta^{56}Fe_{sil.m.-carb.m.}$ increases with increasing Fe^{3+} content.

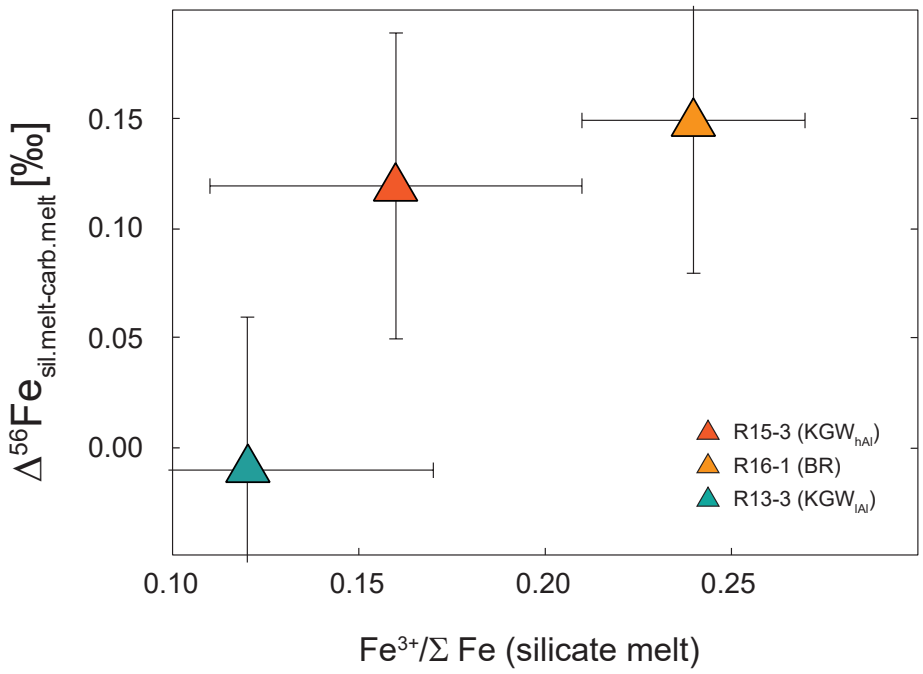

FIGURE 3.12: $\Delta^{56}Fe$ vs. $Fe^{3+}/\Sigma Fe$ determined by Mössbauer spectroscopy. Uncertainties on the $\Delta^{56}Fe$ are the error propagated analytical uncertainties of the method on $\delta^{56}Fe$

In Figure 3.13 a) to c), the $\Delta^{56}Fe_{sil.m.-carb.m.}$ as well as the mean $\Delta^{56}Fe_{sil.m.-carb.m.}$ of isotopically equilibrated samples (T = 1200 °C, P = 0.7 GPa, t $\geq$ three hours) are plotted against compositional (Na/Al) and structural parameters (ASI and n_{mod}/n_{form}) derived from the chemical analyses of the silicate glasses. The iron isotope fractionation between silicate and carbonate melt can be analytically resolved in the three systems BR, Sp, and KGW_{hAl} with a higher degree of polymerization of the silicate melt (comparatively low Na/Al between 1.6 and 2.8, ASI between 0.19 and 0.51, n_{mod}/n_{form} between 0.25 in system KGW_{hAl} and 0.74 in system Sp). Comparing $\Delta^{56}Fe_{sil.m.-carb.m.}$ to the Si/Al ratios shows two distinct groups, where at low Na content, iron isotope fractionation is analytically resolvable, whereas at high Na contents it is not. Comparing the $\Delta^{56}Fe_{sil.m.-carb.m.}$ both to ASI and n_{mod}/n_{form} indicates a trend in which $\Delta^{56}Fe_{sil.m.-carb.m.}$ increases with increasing degree of polymerization of the silicate melt. The samples KGW_{hAl} with an exceptionally high aluminum concentration deviate from this trend.

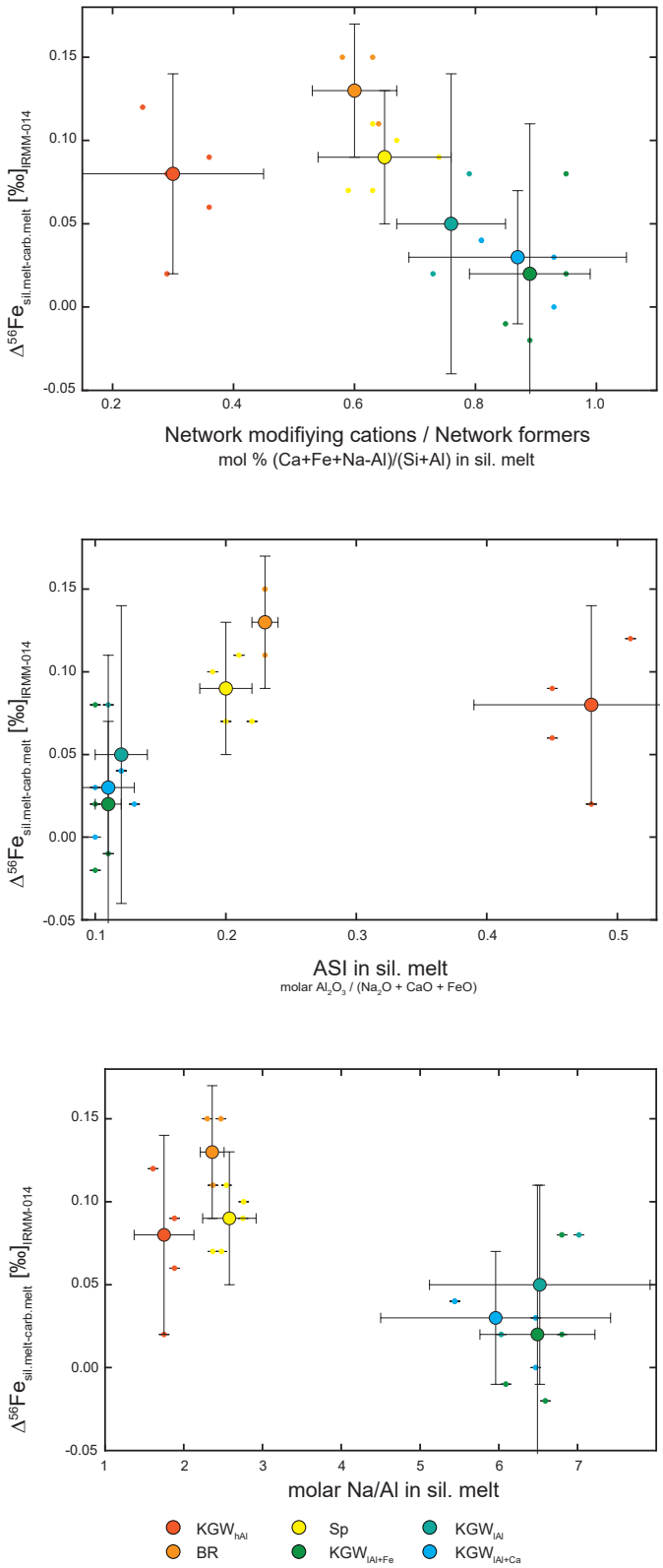

FIGURE 3.13: Δ^{56}Fe vs. n_{mod}/n_{form}, ASI, and Na/Al. Rimmed circles represent calulated mean values, unrimmed circles the results of the single experiments at T = 1200 °C, P = 0.7 GPa, and $t \geq 3$h. The color scale indicates the ASI in the silicate glasses (red = high ASI, blue = low ASI). The error bars on the mean values are the 2 SD calculated from the experimental replicates.

3.4 Inter-mineral iron isotope variability in a melilitite bomb

The iron isotope compositions of different minerals were analyzed at the micro scale in a thin section of a melilitite bomb that is assumed to be representing the interaction of carbonatites with silicates in the mantle. The results of iron isotope in situ analyses on magnetite and olivine grains are presented in Table 3.14. Compared to magnetite, olivine grains span a larger range in iron isotope ratios (Figure 3.14). Both mineral groups are heterogeneous in their iron isotope composition.

The variability of δ^{56}Fe in magnetite reaches from $-0.17\,‰$ ($\pm 0.11\,‰$, $n_{cycles} = 39$) and $+0.08\,‰$ ($\pm 0.09\,‰$, $n_{cycles} = 43$). Most magnetite grains have negative δ^{56}Fe. Note that one magnetite analysis with exceptionally high δ^{56}Fe of $+0.49\,‰$ is associated with an uncertainty of $\pm 0.51\,‰$ and thus within uncertainty not distinguishable from the other magnetite grains. A relation of iron isotopic composition and the chemical composition of the magnetite core (Al- and Cr-rich or not) was not observed.

δ^{56}Fe in olivine range from $-0.66\,‰$ ($\pm 0.11\,‰$, $n_{cycles} = 37$) to $+0.10\,‰$ ($\pm 0.13\,‰$, $n_{cycles} = 36$). Isotopic differences within single olivine grains could not be resolved, with one exception. The iron isotopic composition of olivine grains was not correlated with belonging to one of the identified olivine populations, nor to grainsize. Observations related to spatial resolution are illustrated in Figure 3.15, where iron isotope variabilities are plotted along a profile A-B. Since the sample is not oriented, the profile was randomly chosen. The data show an accumulation of light olivine grains in the upper right corner of the thin section. This is illustrated in a contour plot in Figure 3.15.

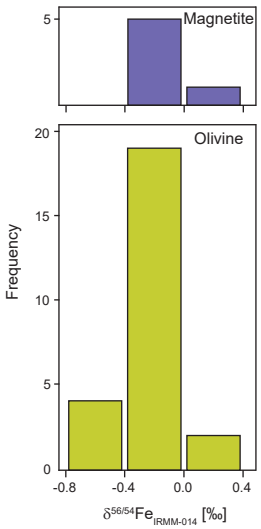

FIGURE 3.14: Histogram of the δ^{56}Fe values for magnetite and olivine grains measured in the melilitite bomb.

TABLE 3.14: Results of UV fs laser ablation

Session	Sample name (order of LA measurement)	Sample name in profile	$\delta^{56/54}$Fe [‰] (measuerd, blank corrected)	± *1	$\delta^{56/54}$Fe [‰] (calculated)	± *2	$\delta^{57/56}$Fe [‰] (measuerd, blank corrected)	± *1	^{54}Cr/^{54}Fe * 10^{-4}	n_{cycles}
Magnetite										
LA-3	Mt-2	M1	-0.84	0.13	-0.17	0.11	-0.09	0.05	0.93	39
LA-3	Mt-3	M5	-2.80	0.15	-0.12	0.12	-0.06	0.06	3.56	44
LA-3	Mt-4	M8	-0.14	0.06	-0.02	0.12	-0.01	0.06	0.15	40
LA-3	Mt-5	M7	-0.44	0.08	0.08	0.09	0.04	0.05	0.64	43
LA-3	Mt-6	M9	-0.77	0.11	-0.03	0.10	-0.01	0.05	0.88	41
LA-3	Mt-13	M4	-4.61	0.44	-0.10	0.10	-0.05	0.05	5.89	40
LA-5	Mt-20	M2	-0.28	0.22	0.03	0.30	0.02	0.15	11.51	31
LA-5	Mt-21	M3	-0.61	0.30	0.49	0.51	0.25	0.25	0.76	22
LA-5	Mt-23	M6	-0.32	0.40	-0.01	0.38	-0.01	0.19	39.64	34
Olivine										
LA-3	Ol-3 near rim	Ol 4-2	-0.04	0.06	-0.07	0.11	-0.04	0.06	0.01	32
LA-3	Ol-3 near center	Ol 4-1	-0.60	0.09	-0.22	0.18	-0.11	0.09	0.47	28
LA-3	Ol-4 near rim	Ol 2	-0.43	0.09	0.00	0.14	0.00	0.07	0.55	45
LA-3	Ol-5-1 near center	Ol 1-2	-1.22	0.15	-0.28	0.14	-0.14	0.07	1.41	40
LA-3	Ol-5-2 near center	Ol 1-1	-0.70	0.09	0.03	0.17	0.01	0.08	0.76	34
LA-3	Ol-6-1 near rim	Ol 7-1	-0.27	0.06	-0.23	0.14	-0.11	0.07	0.01	37
LA-3	Ol-6-2 near rim	Ol 7-2	-0.63	0.08	-0.08	0.14	-0.04	0.07	0.60	43
LA-3	Ol-7 near rim	Ol 12	-0.20	0.06	-0.10	0.14	-0.05	0.07	0.09	38
LA-3	Ol-8 near centre	Ol 10	-0.80	0.08	-0.08	0.15	-0.04	0.07	0.93	40
LA-3	Ol-9 near rim	Ol 8	-0.18	0.06	-0.11	0.10	-0.06	0.05	0.04	39
LA-3	Ol-10-1 near rim	Ol 9-2	-0.08	0.06	0.10	0.13	0.05	0.07	0.02	36
LA-3	Ol-10-2 near rim	Ol 9-1	-0.25	0.05	-0.21	0.11	-0.11	0.06	0.14	48
LA-4	Ol-11	Ol 5	-0.52	0.12	-0.20	0.21	-0.10	0.11	0.27	26
LA-4	Ol-12	Ol 6	-0.24	0.13	-0.30	0.19	-0.15	0.09	0.01	38
LA-4	Ol-13	Ol 13	-0.47	0.08	-0.54	0.16	-0.27	0.08	0.00	31
LA-4	Ol-14	Ol 18	-0.66	0.11	-0.66	0.14	-0.33	0.07	0.26	37
LA-4	Ol-15	Ol 15	-0.49	0.09	-0.45	0.18	-0.23	0.09	0.15	30
LA-4	Ol-5-3	Ol 1-3	-0.38	0.15	-0.07	0.21	-0.04	0.11	0.27	30
LA-4	Ol-16	Ol 3	-0.64	0.14	-0.33	0.27	-0.16	0.13	0.55	27
LA-4	Ol-17	Ol 16	-0.47	0.10	-0.34	0.17	-0.17	0.09	0.21	32
LA-4	Ol-18	Ol 17	-0.82	0.09	-0.48	0.14	-0.24	0.07	0.61	37
LA-4	Ol-19	Ol 14	-1.00	0.12	-0.15	0.21	-0.07	0.10	1.10	35
LA-4	Ol-20	Ol 19	-0.27	0.07	-0.28	0.17	-0.14	0.08	0.05	38
LA-4	Ol-21	Ol 20	-0.14	0.18	-0.36	0.29	-0.18	0.14	0.06	35
LA-4	Ol-22	Ol 11	-0.19	0.07	-0.16	0.14	-0.08	0.07	0.04	42

(*1) The reported uncertainties are error propagations from the internal standard error of the mean at 95 % confidence level of the measured isotope ratios of the individual measurements. (*2) The uncertainties of the calculated $\delta^{56/54}$Fe are the uncertainties of the $\delta^{57/56}$Fe scaled with the factor of 1.99 used for calculating the $\delta^{56/54}$Fe. For samples with a high chromium content (^{54}Cr/^{54}Fe ratio > 0.0001, Steinhoefel et al., 2009) $\delta^{56/54}$Fe were calculated from the interference-free $\delta^{57/56}$Fe (c. f. subsection 2.3.5).

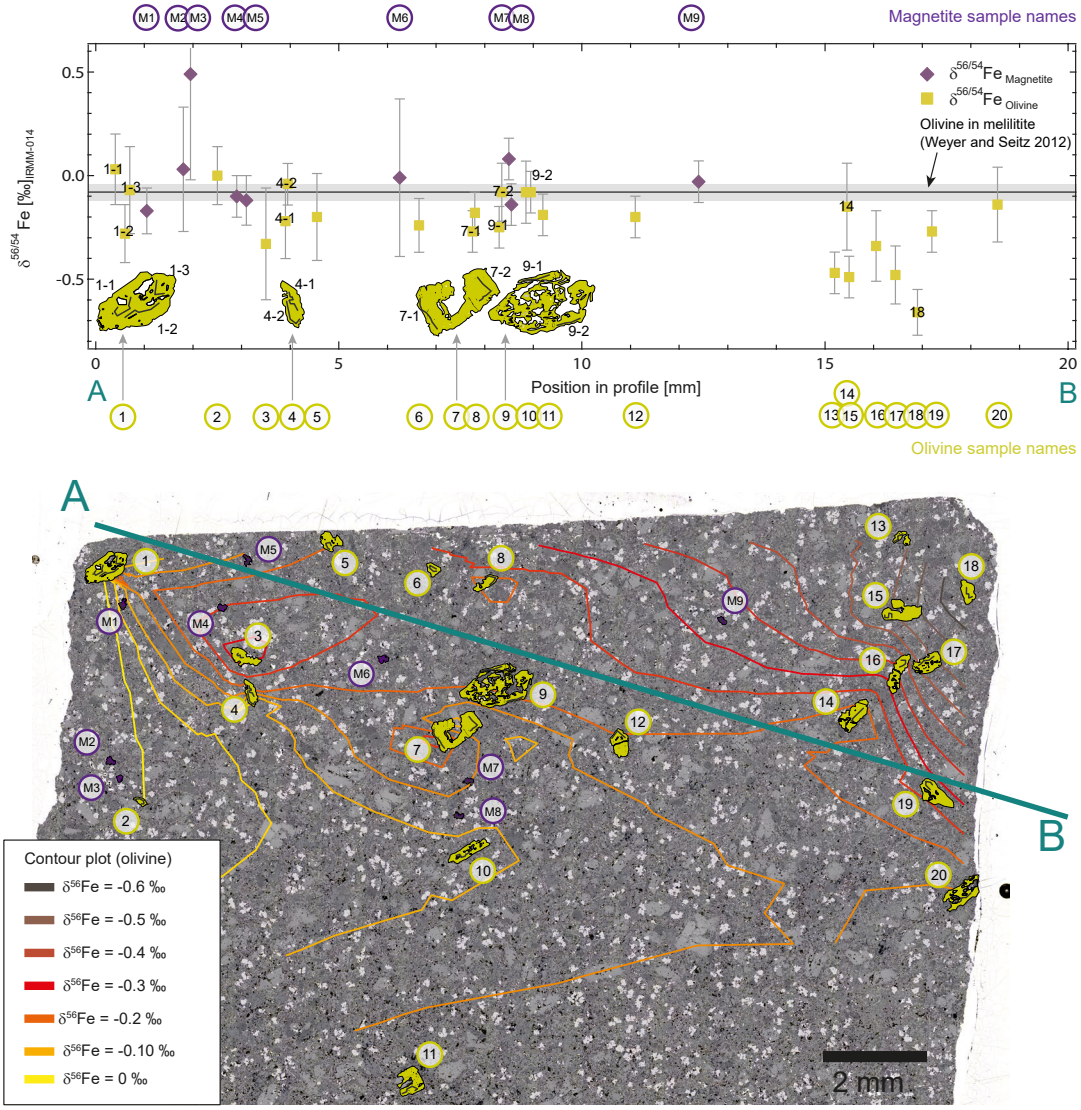

FIGURE 3.15: Variations of δ^{56}Fe of olivine and magnetite grains in the melilitite bomb. The analysed olivine and magnetite grains are highlighted in the reflected light photomicrograph. The corresponding δ^{56}Fe values are shown above along the profile A–B.

4 Discussion

The experimental investigations of iron isotope fractionation between silicate and carbonate immiscible melts provide a new piece in the puzzle of iron isotope signatures derived from the mantle. At the end of this chapter (in section 4.4), the experimental results and the results of in situ iron isotope analyses of the Hawaiian melilitite bomb are compared to existing data and discussed in the context of the main mechanisms of carbonatite genesis, i. e. partial melting of the mantle and fractionation of a carbonated silicate melt.

Prior to this, the technical challenges of the equilibration experiments are discussed in section 4.1 and section 4.2. Then controls on iron isotope fractionation between carbonate and silicate melt are explored using the experimental results and informations from literature (section 4.3). The most important findings of this work are summarized in the following and last chapter Conclusion and outlook.

4.1 Implications from the phase relation experiments

Phase relation experiments were performed in the IHPV and CSPV in carbonatite systems of different composition. The aims of the phase relation experiments were

- to find a capsule design preventing iron loss to the Pt capsule and to gain information about iron bearing carbonatite systems
- to find phase relations suitable for iron isotope analyses

4.1.1 Applicability of the Re-inlay capsule design to investigate phase relations in iron-bearing carbonatite systems

The Re-inlay capsule design by Matsukage and Kubo (2003) was successfully transferred to iron bearing carbonatite systems. Within the pressure and temperature range investigated in this study, the phase assemblages (section 3.1) remain essentially the same as observed in experiments with no or little iron content (e. g. Koster van Groos and Wyllie, 1973; Brooker and Kjarsgaard, 2011 and others) with magnetite as an additional phase. The Re-inlay capsule design can be used in further experiments to investigate element partitioning and phase relations in iron bearing carbonatite systems in more detail. For experiments performed at the intrinsic redox conditions of the IHPV this approach is limited to water-free experiments. Water-bearing charges shift the f_{O2} in the capsules above the Re–ReO_2 buffer, which causes Re to readily dissolve.

4.1.2 Sample selection for iron isotope analyses

To perform iron isotope analyses the investigated system should contain at least two iron bearing phases, which need to be physically or chemically separable. The larger the difference in iron content between the phases the higher the required purity in separation. A successfull phase separation was therefore only possible in the systems producing immiscible carbonate and silicate melts (BR, Sp, KGW). After capsule opening, these two phases could be separated easily by manual picking (subsection 2.3.4). The phase separation was facilitated by a rather even iron distribution between silicate and carbonate melt (Figure 3.5 in section 3.2), minimizing the demand for purity in the separation. Contamination of the carbonate melt with small bubbles of silicate melt could be assessed by the Al-content in ICP-OES analyses of the carbonate melt (subsection 2.3.4).

In the run products of the KB- and CaNa-series, the iron-bearing phases were magnetite, carbonate melt, and, additionally, silicate minerals in the case of KB-samples. While magnetite could be separated chemically from silicate minerals by selective dissolution with HCl, a separation of magnetite from the carbonate quench phase was impossible for two reasons:

- The presence of an additional iron-oxide phase with a dentritic quench texture (found within the carbonate quench product) hampered a chemical phase separation, since a dissolution step dissolving only one of the two oxide phases (either magnetite or the quench-derived oxide) was required.
- A physical phase separation by picking manually or by the use of a magnet was hampered by the small grainsizes of magnetite (down to a few µm) and its finely dispersed appearance thoughout the sample. The very high purity in separation required due to the low iron contents of < 1 wt % (FeO) in the Na-rich carbonate quench phase could not be achieved.

Further attempts to analyze the carbonate quench phase in situ by fs LA were not successful, since the carbonate quench phase was too inhomogeneous. Laser ablation in liquid, as developed by Okabayashi et al. (2011), could not be applied due to the fast dissolution of the sample material in water droplets and the release of CO_2, which formed bubbles dispersing the laser beam. Since no way of phase seperation could be found for the systems KB and CaNa, the following discussion only concerns the systems BR, Sp, and KGW, in which the iron isotope fractionation between carbonate and silicate immiscible melts was successfully determined.

4.2 Chemical and isotopic equilibration of the investigated systems

In any experiment designed to investigate equilibrium isotope fractionation it is necessary to ensure that chemical and isotopic equilibria were actually achieved and maintained in the experiments. The occurence of kinetic effects during iron isotope fractionation must be ruled out, since kinetic isotope fractionation along chemical and thermal gradients may exceed equilibrium isotope fractionation by several orders of magnitude (e. g. Teng et al., 2008; Weyer and Seitz, 2012).

Kinetic effects may occur whenever the experimental conditions (pressure and temperature) are changing, which is mainly during heating at the beginning and cooling at the end of the experimental runs. Due to the changing conditions, phase transformations and the redistribution of elements along thermal and chemical gradients may take place. Isotopic equilibration can only be accomplished after phase transformations and chemical equilibration are completed.

In most isotope equilibration experiments described in literature chemical and isotopic equilibration after heating is recognized as a critical point. Several experimental techniques were developed to ensure isotopic equilibration of the samples (summarized in Shahar et al., 2017). In this thesis, the exchange kinetics between silicate and carbonate melt were monitored in kinetic experiments employing a Fe-58 tracer, and with a time series of equilibration experiments, as discussed in the following. The investigated carbonatite systems proved to be very fast reacting at temperatures of 900 °C and higher and were isotopically and chemically equilibrated after 3 hours run duration already. In such a fast reacting system, also the kinetics during cooling need to be considered.

4.2.1 Phase transformations and reaction kinetics during heating

Until the experimental conditions are reached, phase transformations take place while the starting materials evolve from carbonate and oxide powders into silicate and carbonate melts. These phase transformations cannot be directly observed. Yet, remnant phases from heating may be found in experimental runs too short for completing the equilibration at run temperature. Some indicators for incomplete phase equilibration were found by SEM-EDX analyses in the samples of the two-hour experiments:

- Small amounts of iron bearing minerals (most likely aenigmatite and clinopyroxene, see Table 3.3 in subsection 3.1.2) were interpreted as remnants from heating.
- The heterogeneous bubble size distribution and streaks only observed in the silicate glasses of the two-hour runs are also pointing to a non-equilibrated system.

In the experiments with durations of 20 hours or more (SEM analyses of the 3 hour runs are lacking) none of these indicators could be observed. This suggests that the minerals dissolved after longer annealing at run temperature.

The presence of fast grown crystalline phases might cause local inhomogeneities in iron isotopic composition. Yet, the impact of these non-equilibrium phases on chemical and iron isotope compositions measured in silicate and carbonate melts of the two-hour runs was analytically not resolvable, suggesting only minor amounts of silicate and oxide minerals were left after two hours. To be on the safe side, only samples with run durations >3 hours were used to calculate the mean iron isotope equilibrium fractionation. Further evidence that iron isotopic equilibrium is reached after 3 hours is given by the kinetic experiments, which are discussed in the following, subsection 4.2.2.

4.2.2 Equilibration at run temperature

Chemical equilibrium

As former experimental studies have shown, (natro-) carbonatite systems chemically equilibrate rather fast (i. e. within 24 hours, e. g. Koster van Groos and Wyllie, 1973; Brooker, 1998; Veksler et al., 1998). Therefore, chemical diffusion in silicate and carbonate melts at ≥ 900 °C can be expected to be fast.

An indication that after two hours the samples are already very close to chemical equilibrium comes from the ICP-OES analyses of the silicate glasses. In a plot of the molar ratio Ca/(Ca + Mg + Fe) of the silicate glass against temperature (Figure 4.1, upper plot), Ca/(Ca + Mg + Fe) increases with temperature. In reverse, Ca/(Ca + Mg + Fe) should remain constant in a time series of one run temperature in a chemically equilibrated experiment. This is exactly, what can be observed in a plot of Ca/(Ca + Mg + Fe) from the experimental runs at 1200 °C against run duration (Figure 4.1, lower plot), even in experiments of only two-hour run duration.

Another indicator that chemical equilibrium is achieved are the sharp menisci separating the silicate from the carbonate melts (e. g. Freestone and Hamilton, 1980), which are observed already after two hours runtime (Table 3.3 in subsection 3.1.2).

Iron isotopic equilibration

The approach of the system to iron isotopic equilibrium was monitored by kinetic experiments and by time series. In the kinetic experiments, the iron isotopic equilibrium value of the system is reached after 3 hours. The kinetic experiments start from two phases that are supposed to resemble the run products (a silicate glass resembling the silicate melt, and siderite resembling the carbonate melt). This is a contrast to the equilibration experiments,

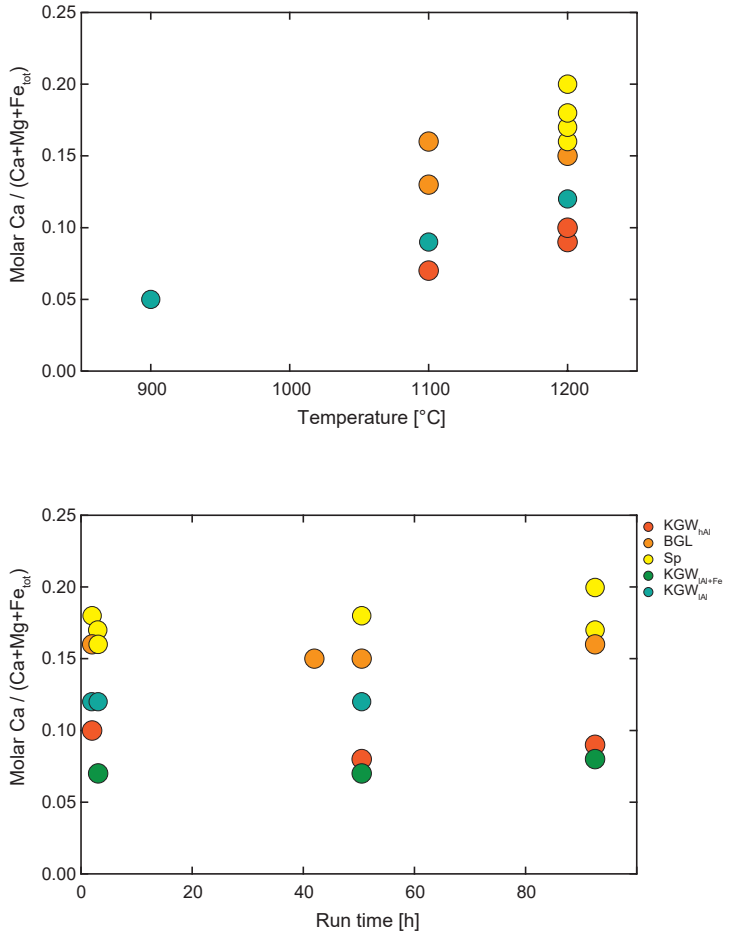

FIGURE 4.1: Molar Ca/(Ca + Mg + Fe) vs. temperature (above) and vs. time (below) in the silicate glasses of experimental run products. In the silicate glasses, the molar Ca/(Ca + Fe + Mg) changes with temperature, but remains stable within run times at a constant temperature of 1200 °C.

in which silicate melt and carbonate melt are formed from the same starting powder. Since in the kinetic experiments the starting phases resemble the run products, little or no phase transformations during heating are expected. Accordingly, there should be no remnant phases from heating.

Additional evidence for a fast isotopic equilibration is obtained by the time series experiments on iron isotope fractionation between the two melts at 1200 °C and 0.7 GPa. Within analytical uncertainty, iron isotope fractionation between silicate and carbonate melts remained the same in experiments of 2 to 90 hours run times, which indicates that isotopic equilibrium is achieved and maintained in all experiments.

In summary, iron isotopic equilibrium is achieved after a few hours of runtime. Although local inhomogeneities exist in samples of only two hours runtime, these are already so close to chemical and iron isotopic equilibrium, that they are indistinguishable within analytical uncertainty. Yet, since data from the two-hour runs are of higher heterogeneity,

only samples of runtimes ≥ 3 hours are used in the further discussion.

4.2.3 Kinetic effects during quenching

At the end of the high temperature experiments, the samples were quenched isobarically, which provided an initial cooling rate of 200 °C in the first 60 seconds. This cooling rate was high enough to prevent the phase assemblages from chemical and isotopic equilibration at decreasing temperatures.

Fe diffusion in the melts was estimated to be a critical process that might induce a kinetic isotope effect in the quench products. Using diffusion coefficients of iron in silicate melts compiled by Zhang et al. (2010), the maximum distance iron could cover during cooling was estimated to be 100 µm in melts of the BR-series. However, by SEM-EDX analyses no zoning was observed at the rims of the silicate glasses. Furthermore, while picking the sample shards for isotope analyses the rims of the glass beads were avoided when possible.

Another concern were the dendritic exsolution textures of the carbonate melts indicating melt exsolution within the carbonate melt and the nucleation of carbonate minerals from the carbonate melt. The inhomogeneous appearance of the carbonate quench products suggests that signatures of kinetic effects are more likely to be found in the carbonate melt than in homogeneous the silicate glasses. Therefore, some of the carbonate quench products were sampled multiple times at different positions in the capsule. However, the inhomogeneities of the carbonate quench products visible in SEM-EDX analyses were analytically not resolvable in ICP-OES or iron isotope analyses. It is concluded, that the chemically homogeneous silicate glasses are homogeneous in iron isotopic composition as well. Furthermore, a representative sampling of each of the quenched phases should average out possible local inhomogeneities resulting from quenching.

To safely exclude the influence of quenching on the results in future experiments it is recommended to perform experiments of different quench rates to monitor a possible influence.

4.3 Controls on iron isotope fractionation between silicate and carbonate melts

Iron isotope fractionation depends on the bond strength iron achieves in a phase. The iron bond strength is dependent on temperature, pressure, composition, iron oxidation state and coordination, and so is iron isotope fractionation. Whether and how these factors influence iron isotope fractionation in these experiments is discussed in the following.

4.3.1 Pressure

In the investigated carbonatite systems, pressure might affect iron isotope fractionation directly via volume changes of the phases or the Fe-site, or indirectly by controling the CO_2 solubility in both silicate and carbonate melts. At the investigated conditions an effect of pressure on iron isotope fractionation was not detected (Figure 3.10, subsection 3.3.2).

Volume changes with pressure would affect bond distances and consequently iron isotopic fractionation. Since silicate and carbonate melts differ in their compressibility (Jones et al., 2013, and references therein), this might have an impact on iron isotope fractionation at mantle pressures. Yet, in the investigated pressure range < 1 GPa, only very small volume changes in the phases are expected. Thus, bond distances and consequently iron isotopic fractionation virtually remain the same (e. g. Young et al., 2015, and references therein).

In the investigated carbonatite systems, pressure controls the CO_2 solubility in both silicate and carbonate melts. With higher pressure, the solubility of CO_2 in the silicate and carbonate melt increases (e. g. Brooker et al., 2001a; Brooker, 1998). At CO_2-undersaturated conditions, the extent of the immiscibility field can be affected by relatively small changes in p_{CO2}. Resulting compositional and structural changes in the melts might influence iron isotope fractionation. By employing CO_2 saturated compositions in this study, the effect of small pressure changes on the extent of the two-liquid field was minimized. This is a further parameter explaining the insensitivity of iron isotope fractionation regarding pressure.

4.3.2 Temperature and redox dependence

In Figure 4.2 $\Delta^{56}Fe_{A\text{-}B}$ is plotted against $1/T^2$ to illustrate its dependence on temperature and oxidation state: The magnitude of iron isotope fractionation decreases with increasing temperature ($\Delta^{56}Fe_{A\text{-}B} \sim 1/T^2$, e. g. Bigeleisen and Goeppert-Mayer, 1947).

To be able to compare the new and first data set of experimentally determined $\Delta^{56}Fe_{sil.\,m.\text{-}carb.\,m.}$ to literature data, the $\Delta^{56}Fe_{A\text{-}B}$ in Figure 4.2 were calculated from β-factors of phases that represent the immiscible silicate and carbonate melts as close as possible. To my knowledge, β-factors of high alkaline, CO_2-rich silicate melts and of carbonate melts have not yet been determined, so a direct comparison was not possible. Hence, the carbonate melt was approximated using the β-factor of siderite, which was determined by ab initio calculations by Blanchard et al. (2009). The silicate melt was approximated using β-factors of basic glasses determined by Dauphas et al. (2014). The calculated fractionation lines provide an estimate, which magnitude of $\Delta^{56}Fe_{sil.\,m.\text{-}carb.\,m.}$ to expect in the investigated temperature range of 900 to 1200 °C, and whether changes in $\Delta^{56}Fe_{sil.m.\text{-}carb.m.}$ with temperature are analytically resolvable.

In Figure 4.2 not only the temperature dependence of $\Delta^{56}Fe_{A\text{-}B}$, but also the dependence on $Fe^{3+}/\Sigma Fe$ is illustrated. Dauphas et al. (2014) detemined the β-factors of basic glasses with $Fe^{3+}/\Sigma Fe$ of 0.57, 0.32 and < 0.02 (in the following $basalt_{0.57}$, $basalt_{0.32}$, and $basalt_{0.02}$). To illustrate the redox dependence of $\Delta^{56}Fe_{A\text{-}B}$, the fractionation lines of these three glasses and siderite are ploted in Figure 4.2. While the $Fe^{3+}/\Sigma Fe$ of $basalt_{0.32}$ and $basalt_{0.02}$ frame the $Fe^{3+}/\Sigma Fe$ measured in the silicate glasses of this study ($Fe^{3+}/\Sigma Fe$ between 0.12 and 0.24, subsection 3.2.2), $basalt_{0.57}$ represents a maximum estimate of oxidation state, which is unlikely to be reached in any of the samples.

Figure 4.2 shows, that whether $\Delta^{56}Fe_{A\text{-}B}$ is large enough to be analytically resolvable is not only temperature, but also redox dependent. Assuming that

- Fe speciation and coordination in the carbonate melt or siderite, respectively, remain more or less similar, and
- no significant changes in the structure of Fe^{2+} and Fe^{3+} in the silicate melts occur,

$Fe^{3+}/\Sigma Fe$ in the silicate melts determines the magnitude of $\Delta^{56}Fe_{A\text{-}B}$ at a given temperature. A higher Fe^{3+} content leads to a larger $\Delta^{56}Fe_{A\text{-}B}$, due to the difference in the vibrational force constants of Fe^{2+} and Fe^{3+} (Dauphas et al., 2014). Hence, the iron isotope fractionation between basalt and siderite is expected to be analytically resolvable even at temperatures of 1200 °C for glass compositions with $Fe^{3+}/\Sigma Fe$ of 0.57 and 0.32, but not for the highly reduced $basalt_{0.02}$. Yet, temperature related differences in $\Delta^{56}Fe_{basalt\text{-}siderite}$ between 900 and 1200 °C are not expected to be resolvable, even for a relatively large iron isotope fractionation between a basalt melt with high Fe^{3+} content ($basalt_{0.57}$) and siderite. These estimates from literature data match exactly what is observed in the three selected silicate glasses investigated with Mössbauer spectroscopy, where $\Delta^{56}Fe_{sil.\,m.\text{-}carb.\,m.}$ is larger at higher Fe^{3+} contents (Figure 3.12 in subsection 3.3.2). Furthermore, the experimental data agree with the predictions by Dauphas et al. (2014), in that a temperature dependence of $\Delta^{56}Fe_{sil.\,m.\text{-}carb.\,m.}$ was not observed in the experiments (Figure 3.11 in subsection 3.3.2).

While Figure 4.2 shows the redox dependence of $\Delta^{56}Fe_{sil.\,m.\text{-}carb.\,m.}$, it may also indicate a dependence on composition and structure of the silicate melt. Where $\Delta^{56}Fe_{sil.m.\text{-}carb.m.}$ were resolvable in the experiments (compositions KGW_{hAl}, BR, and Sp), they plot within analytical uncertainty in the range defined by the fractionation lines of $basalt_{0.32}$ – siderite and $basalt_{0.02}$ – siderite, respectively. The samples of extremely peralkaline compositions (KGW_{lAl} , KGW_{lAl+Fe}, and KGW_{lAl+Ca}), in which $\Delta^{56}Fe_{sil.m.\text{-}carb.m.}$ was not resolvable, plot on or below the fractionation line of $basalt_{0.02}$ – siderite. The samples of KGW_{lAl} ($Fe^{3+}/\Sigma Fe$ of 0.12) are within uncertainty on this line.

Yet, given that most likely all silicate melts of these compositions have a higher Fe^{3+} content than the highly reduced $basalt_{0.02}$, a larger fractionation should be expected. The

samples of KGW_{lAl+Fe} and KGW_{lAl+Ca} (of unknown $Fe^{3+}/\Sigma Fe$) plot clearly below this line. Since these samples are representing the most depolymerized compositions, this may indicate an additional structural dependence of the $\Delta^{56}Fe_{sil.\,m.\text{-}carb.\,m.}$, which is discussed in more detail in the following.

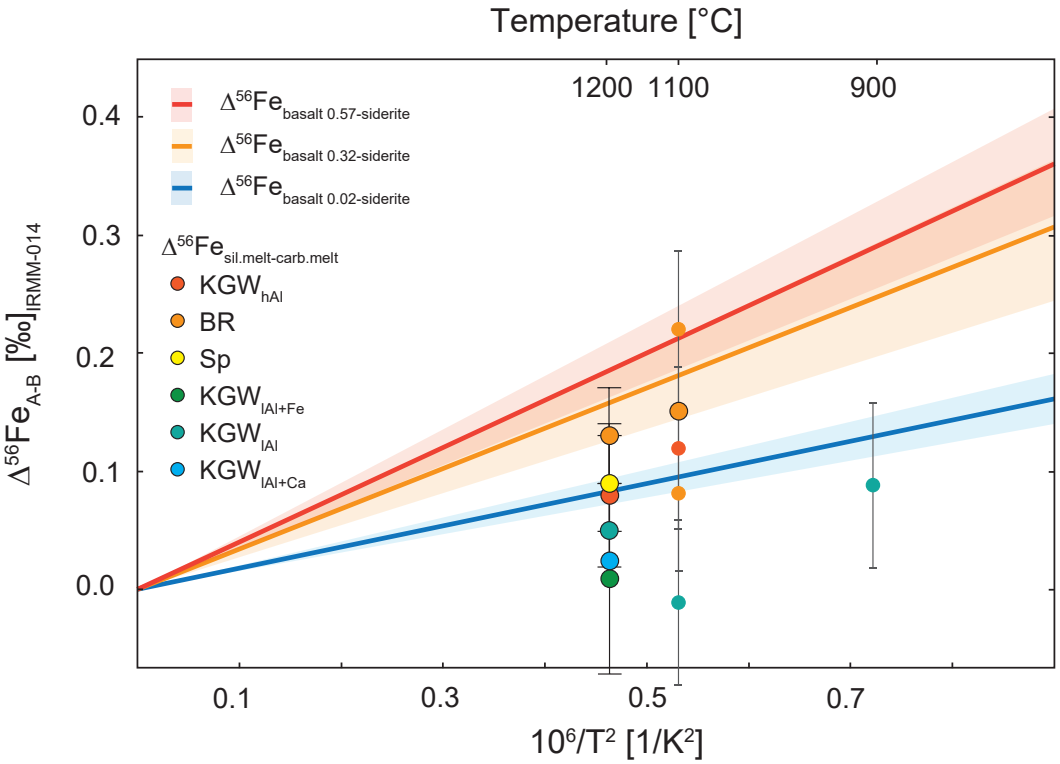

FIGURE 4.2: $\Delta^{56}Fe$ vs. $10^6/T^2$. The $\Delta^{56}Fe_{sil.\,melt\text{–}carb.\,melt}$ of the experiments are compared to $\Delta^{56}Fe$ expected between basalt and siderite (Dauphas et al., 2014). Rimmed circles represent the calculated mean $\Delta^{56}Fe$ values as presented in section 3.3, Table 3.12 and Table 3.13. Unrimmed circles represent single experiments. For clarity the $\Delta^{56}Fe$ values of single experiments are shown only for T = 1100 °C and T = 900 °C, at which only a few experiments were performed.

4.3.3 Controls of melt composition and structure on iron bond strength

The low $\Delta^{56}Fe_{sil.m.\text{-}carb.m.}$ in the series with the lowest degree of polymerization indicate that in these samples, iron bond strength in silicate and carbonate melt are no longer distinct. This can be achieved by an increase of iron bond strength in the carbonate melt or a decrease of bond strength in the silicate melt (or both). Neither literature nor the investigations of this study do provide sufficient information to discuss changes of iron bond strength in the carbonate melt. (Yet, intuitively, an increase of bond strength in the

carbonate melt seems rather unlikely.) A decrease of bond strength in the silicate melt in dependence of composition, coordination environment, and silicate melt structure is discussed in more detail in the following.

Silicate melt composition and coordination environment of iron

The bond strengths of iron in a silicate melt is not only dependent of its oxidation state, but also of its coordination environment. Dauphas et al. (2014) found that iron force constants of basalt, andesite, and dacite glasses at variable $Fe^{3+}/\Sigma Fe$ define a common linear correlation, while the rhyolite glasses plot on a different trend. This observation of Dauphas et al. (2014) was complemented by Sossi and O'Neill (2017, see Figure 1.1 in subsection 1.2.2), showing that a lower coordination of iron in a silicate phase leads to a higher force constant (see also Table 4.1 in subsection 4.4.3). This is in good agreement with the expectation that the bonds between cations and oxygen in a 4-fold coordination are of a more covalent character and thus stronger than bonds in higher coordinations (Hudon and Baker, 2002a).

Transferring these observations to the investigated carbonatite system implicates that the decrease of bond strength in the silicate melt was caused by the appearance of iron in a coordination environment higher than 6-fold. This is not observed by Mössbauer spectroscopy. On the opposite, in the KGW-melts, where lower force constants of iron are expected, a second lower (likely 4-fold) coordinated environment of Fe^{2+} occurs in addition to the high-coordinated environment of Fe^{2+} and the lower coordinated environment of Fe^{3+} observed in the BR-glasses.

The additional coordination environment of Fe^{2+} cannot explain the observed iron isotope fractionation, but its occurrence is in good agreement with observations by Knipping et al. (2015), who investigated the effect of oxygen fugacity on oxidation state and coordination of iron in alkali silicate glasses. Knipping et al. (2015) suggested a change of the iron dissolution mechanism in alkali silicate melts at very reducing conditions, enabling a 4-fold coordinated environment of Fe^{2+} as observed in the samples of this study. Since it is highly unlikely, that the appearance of an additional lower coordinated environment of iron is responsible for the decrease of iron bond strength and thus of the iron force constant, a closer look into further stuctural changes of the silicate melt is needed.

Silicate melt composition and degree of polymerization

To reduce the bond strength of iron in the systems with extremely alkaline silicate melts, substantial structural changes between the highly alkaline silicate melts (BR, Sp, and KGW_{hAl}) and the extremely alkaline silicate melts (KGW_{lAl}, KGW_{lAl+Fe}, and KGW_{lAl+Ca}) are required. The systems KGW_{lAl}, KGW_{lAl+Fe}, and KGW_{lAl+Ca}, in which $\Delta^{56}Fe_{sil.m.-carb.m.}$

was not resolvable, are characterized by extremely peralkaline silicate melt compositions with high ratios of network modifying to network forming cations. This corresponds to relatively low degrees of polymerization. Furthermore, they all have remarkably high Na/Al ratios in the silicate melt.

In highly polymerized silicate melts, oxygen atoms are polarized towards the silicon. This leaves little electric charge to network modifying cations. Hence, modifier cations prefer less polymerized environments, where they can bond with a sufficient number of NBO to neutralize their coulombic repulsions. This behaviour may lead to the microsegregation of network modifiers from the silicate network and the formation of subnetworks that are separated from the silicate network by NBO-rich regions (Henderson, 1995; Hudon and Baker, 2002b). In carbonated systems, the formation of subnetworks within the silicate network has been observed before in the form of subnetworks of free ionic carbonate groups (FIC, e. g. Morizet et al., 2017; Moussallam et al., 2016, cf. subsection 1.3.2). Not only the carbonate content, but also a high sodium content may contribute to the microsegregation of silicate networks. Pohlenz et al. (2018) suggested that microsegregations driven by a high sodium content might be responsible for the highly flexible structural environments they observed in silicate melts of carbonatite systems.

In a binary silicate system, the segregation of subnetworks starts at sodium contents >30 mol % Na_2O (Henderson, 2005), which are not reached in the experiments (contents between 24 and 26 mol % Na_2O in the less polymerized series). Still, together with CO_2-saturation and a high content of other network modifying cations, an overall depolymerization of the silicate 3d-network by the formation of microsegregated subnetworks seems possible. The microsegregated subnetworks would be formed by network modifying cations and FIC groups bound to metal cations (predominantly sodium and calcium).

In this scenario, there a two ways, how iron bond strength could be decreased compared to a more polymerized silicate melt:

- In general, a depolymerized silicate network would provide larger interstitial spaces, resulting in higher bond length of network modifiers accommodated in these interstitial spaces. Higher bond length again would result in weaker bonds.

- In the segregated subnetworks, ferrous iron possibly bonds to FIC groups. Such a type of bonding would be similar in bond strength to iron bonds in a carbonate melt, and thus reduce the iron isotope fractionation between silicate and carbonate immiscible melts.

4.4 Iron isotope fractionation in natural carbonatites and carbonated systems

In the following chapter I discuss the findings of my investigation in the context of natural systems, with emphasis on carbonatite genesis and carbon in the Earth's mantle. First I will adress how and how far the results of the experiments can be transferred to natural systems. Then the observations of the in situ iron isotope analyses on the melilitite bomb from the SLC are discussed and compared to literature data. In the final section, I will discuss the existing models of carbonatite genesis taking into account the new information from the investigations of this thesis.

4.4.1 The transfer of the experimental data to natural systems

For a comparison of the relative iron isotope fractionation between a silicate and a carbonate melt measured in the experiments with existing data, one of the investigated phases was to function as a benchmark on the scale of "absolute" iron isotope fractionation (β-factors). For this purpose the silicate glass of the BR series was chosen, following the assumption that it falls on the same linear correlation between force constants and $Fe^{3+}/\Sigma Fe$ as basalt, andesite, and dacite glasses (Dauphas et al., 2014, cf. subsection 1.2.2 and subsection 4.3.3), which represents a mixture of four- to sixfold coordinated iron. Using the correlation determined by Dauphas et al. (2014), the force constant of the silicate glass BR was estimated from the determined $Fe^{3+}/\Sigma Fe$ as $F_{BR} = 0.24 * (351 - 199) + 199$. Then the β-factor was calculated from the force constant at the experimental equilibration temperature (1200 °C) between carbonate and silicate melt as $1000 \ln \beta_{^{56}Fe/^{54}Fe} \approx 2904\, F/T^2$ (Dauphas et al., 2012, see also Equation 1.4, subsection 1.2.1). Knowing the β-factor of the silicate melt produced in the experiments allows the comparison to other phases with determined β-factors and the approximation of the equilibrium fractionation factor between the silicate melt and mineral phases as

$$1000(\ \ln \beta_{\text{sil.m.}} - ln\ \beta_{\text{min.}}) = \Delta^{56}Fe_{\text{sil. m.-min.}} \approx \delta^{56}Fe_{\text{sil. m.}} - \delta^{56}Fe_{\text{min.}} \tag{4.1}$$

Since the fractionation between silicate melt and carbonate melt at 1200 °C

$$\Delta^{56}Fe_{\text{sil. m.-carb.m.}} = \delta^{56}Fe_{\text{sil. m.}} - \delta^{56}Fe_{\text{carb.m.}} \tag{4.2}$$

is known from the experiments, the equilibrium iron isotope fractionation between mineral phases and the carbonate melt,

$$\Delta^{56}Fe_{\text{min.-carb.m.}} = \delta^{56}Fe_{\text{min.}} - \delta^{56}Fe_{\text{carb.m.}} \tag{4.3}$$

can be estimated by rearranging Equation 4.1 and Equation 4.2 and inserting them in Equation 4.3:

$$\Delta^{56}Fe_{min.\text{-}carb.m.} = \Delta^{56}Fe_{sil.m.\text{-}carb.m.} - \Delta^{56}Fe_{sil.m.\text{-}min.} \quad (4.4)$$

The calculated $\Delta^{56}Fe_{min.\text{-}carb.\,m.}$ and $\Delta^{56}Fe_{sil.\,m.\text{-}min.}$ are presented in Table 4.1 in subsection 4.4.3. This data set allows to discuss carbonatite genesis for the first time in context with experimentally determined Δ^{56}Fe between silicate and carbonate melts. This perspective provides new insights into the direction and magnitude of iron isotope fractionation in the carbonatite system. These first data bring along uncertainties and limitations, which will be adressed in section 5.1, where outstanding questions for further research are summarized.

Before taking up the discussion about carbonatite genesis, the findings from the investigation of iron isotope fractionation between olivine and magnetite grains in the Hawaiian melilitite bomb are discussed in subsection 4.4.2.

4.4.2 The melilitite bomb

To interpret the δ^{56}Fe observed in olivine and magnetite grains of the Hawaiian melilitite bomb I will compare my findings to the iron isotope variability found in a melilitite invesitigated by Weyer and Seitz (2012). To my knowledge, this is the only reported data on iron isotope ratios in a melilitite. The data are used to estimate the $\Delta^{56}Fe_{melilitite\ melt\text{-}mineral}$ for olivine and magnetite, respectively. Then I will evaluate, wether the influence of magma mixing with a carbonatite melt is visible in the iron isotope ratios, and which other steps in magma evolution may have caused the δ^{56}Fe signatures.

Melilitite magmas are assumed to be generated by low degree melting of carbonated peridotite (e. g. Brey and Green, 1975; Hirose, 1997; Dasgupta et al., 2007). For lack of a better comparison, the force constants of Fe-O in basalt melts were used to estimate the Δ^{56}Fe between a melilitite melt and minerals. The observations of Weyer and Seitz (2012) on a melilitite from the Hegau volcanic region, Germany, fit this assumption. They investigated the whole rock sample, an olivine mineral separate, and the matrix, and found a bulk rock composition of $\delta^{56}Fe = 0.13\,‰$ ($\pm 0.06\,‰$, 2SD), which is similar to MORB compositions. Assuming that this sample was derived from low degree partial melting of a mantle peridotite of average isotopic composition ($\delta^{56}Fe_{mantle} = 0.03\,‰ \pm 0.03\,‰$, Sossi et al., 2016), the direction and magnitude of the iron isotope fraction is the same as observed for partial melting of common basalt melts (e. g. Dauphas et al., 2014, and references therein).

Carbonatite magmas are assumed to be enriched in light iron isotopes already at mantle depths (Johnson et al., 2010, cf. subsection 1.2.3). Thus, it seems most likely, that magma mixing with a carbonatite magma may shift the δ^{56}Fe of a melilitite bulk magma to an

iron isotopic composition lighter than expected from literature consideration. Since the composition of the matrix was not investigated in this study, the imprint of a carbonatite magma might only become visible, if the overall isotopic composition of the investigated minerals was shifted to significantly light δ^{56}Fe. In the analyzed SLC melilitite bomb neither olivine nor magnetite grains were homogeneous in their isotopic composition. This indicates isotopic disequilibrium conditions before (or after) entrainment. Due to the iron isotopic disequilibrium, the composition of the melilitite matrix could not be estimated as equilibrium iron isotope fractionation between minerals and a melilitite magma.

Olivine

The span of δ^{56}Fe ranging from $-0.66\,‰$ ($\pm 0.11\,‰$ 2SE) to $+0.10\,‰$ ($\pm 0.13\,‰$ 2SE) found in olivine grains in the here investigated SLC melilitite bomb has the magnitude of kinetic isotope fractionation (e. g. Teng et al., 2011; Weyer and Seitz, 2012; Oeser et al., 2015). Most likely, in the SLC melilitite bomb olivine reacted with a Ca-rich and Fe-bearing or Fe-rich carbonatite magma. This led to the transformation of forsterite to monticellite and required a re-distribution of Ca, Mg, and Fe between mineral and melt.

The extremely light δ^{56}Fe found in some olivine grains can be well explained by Fe-Mg interdiffusion in olivine during chemical equilibration with an evolving melt or during magma mixing, in which iron was enriched in olivine in exchange for magnesium. Since light isotopes diffuse slightly faster than heavy isotopes, this would concentrate light isotopes in the olivine and produce large iron isotope fractionation (e. g. Richter et al., 2003)[1]. Thus, the extremely light δ^{56}Fe fit the petrographical observation of olivine Fe-Mg zoning. Similarly, Fe-Ca interdiffusion can lead to kinetic iron isotope fractionation, as observed by Zhao et al. (2017b) in clinopyroxene. Although uncommon in olivine, this possibly happened during the alteration of olivine to monticellite at the mineral rims (section 2.2), which is interpreted as a petrographic indicator for magma mixing with a carbonatite magma.

Since the kinetic effects of Fe-Mg (or Fe-Ca) interdiffusion shift the δ^{56}Fe to lighter values, only the heaviest δ^{56}Fe measured in olivine of the Hawaiian sample might reflect a former equilibrium with a melilitite magma. The respective equilibrium isotopic signature should be preserved most likely in olivine cores (except for olivines with a skeletal habit), even if the rims were affected by Fe-Mg interdiffusion. Yet, a correlation between distance from core and δ^{56}Fe could not be observed and resolved. The random connection of δ^{56}Fe and the location of the laserablation path within the olivine grain may add to the evidence

[1] As studies by Oeser et al. (2015, 2018); Sio et al. (2013) have shown, combined Fe and Mg isotope and chemical analyses can be used to distinguish crystal growth from magma mixing, and to estimate timescales of magmatic processes. This was not possible in my investigation, due to small grainsizes and multiple inclusions, which hampered isotope analyses resolving the zoning (subsection 2.3.5).

for isotopic disequilibrium as a consequence of magma mixing. Further investigations should examine, if different δ^{56}Fe in olivine are linked to olivine populations with distinct compositions. The isotopically heavier olivine grains in the here investigated Hawaiian melilitite are similar (within uncertainty) in their iron isotopic composition to the olivine mineral seperate reported by Weyer and Seitz (2012), which has a δ^{56}Fe of $-0.08\,‰$ ($\pm 0.04\,‰$, 2SD, Figure 4.3). According to the assumptions made above, olivine grains in equilibrium with a melilitite melt should be enriched in light isotopes (analog to equilibration with a basalt melt, Table 4.1), while the melilitite matrix would become heavier. The melilitite matrix investigated by Weyer and Seitz (2012) has an iron isotopic composition of $0.16\,‰$ ($\pm 0.05\,‰$, 2SD), which would fit this assumption. Yet, the resulting apparent $\Delta^{56}Fe_{\text{matrix-olivine}}$ = -0.25 ‰ detected by Weyer and Seitz (2012) not necessarily reflects equilibrium fractionation, but may contain significant contributions from kinetic fractionation. With this small base of data, interpretations of δ^{56}Fe regarding magma evolution in either of the two melilitite samples remain speculative.

Magma mixing with a carbonatite magma cannot be inferred from the iron isotope signature of olivine grains. Without more information on the chemical composition and transport direction of the involved elements, it is not possible to distinguish between Fe-Mg and Fe-Ca interdiffusion. For further investigations, EMPA mappings along the laserablation paths (cf. Oeser et al., 2018) might complement existing data and enable more detailed interpretations.

Magnetite

The magnetite grains in the melilitite bomb fall in a significantly smaller range of δ^{56}Fe (between $-0.17\,‰$, ± 0.11 2SE and $0.08\,‰$, ± 0.09 2SE) than the olivine grains (between $-0.66\,‰$, $\pm 0.11\,‰$ 2SE to $+0.10\,‰$, $\pm 0.13\,‰$ 2SE). This may be due to the smaller grainsizes and rather high self-diffusion coefficients D_{Fe} of iron in magnetite compared to the diffusion coefficients for Fe-Mg interdiffusion $D_{\text{Fe-Mg}}$ in olivine, allowing for a much faster re-equilibration of the magnetite grains with a magma. At conditions and timescales required to cause the large kinetic iron isotope fractionation by Fe-Mg interdiffusion observed in the olivine grains of the SLC melilitite bomb, magnetite is expected to completely re-equilibrate with a silicate magma. This can be estimated employing the respective diffusion coefficients D and the distance to be covered by diffusion L. The timescales for isotopic re-equilibration can then be calculated as $t = L^2/D$. Depending on redox conditions, self-diffusion coefficients D_{Fe} of iron in magnetite range between 10^{-15} m^2/s at 900 °C and 10^{-11} m^2/s at 1400 °C (Van Orman and Crispin, 2010; Dieckmann and Schmalzried, 1977), the diffusion coefficients for Fe-Mg interdiffusion $D_{\text{Fe-Mg}}$ in olivine are between 10^{-20} m^2/s at 900 °C and 10^{-16} m^2/s at 1200 °C (Dohmen and Chakraborty, 2007). As an example, at a temperature of 1100 °C, magnetite grains with a diameter

of 30 µm would equilibrate within one day or faster, depending on redox conditions. At the same temperature and length-scale, isotopic re-equilibration by Fe-Mg interdiffusion would require at least ten days or more, depending on redox conditions.

Most magnetite grains in the SLC melilitite bomb have $\delta^{56}\text{Fe} \leq 0.00\,‰$. This is an unexpectedly light composition, if magnetite was in equilibrium with a melilitite magma. As described above, a melilitite magma derived from low degree partial melting of a mantle peridotite with average iron isotope composition ($0.03\,‰ \pm 0.03\,‰$, Sossi et al., 2016) should be enriched in heavy istotopes. Using the fractionation factor between a Fe^{2+}-basaltic silicate melt and magnetite (Dauphas et al., 2014; Sossi and O'Neill, 2017) $\Delta^{56}\text{Fe}_{\text{magnetite} - Fe^{2+}\text{-basaltic sil. melt}}$ is $0.14\,‰$ or larger, meaning compared to the melilitite melt magnetite should be enriched in the heavy isotope. With higher $Fe^{3+}/\Sigma\,\text{Fe}$ in the melilitite melt the fractionation would become smaller. Yet, magnetite would become isotopically lighter than the melilitite melt only above a $Fe^{3+}/\Sigma\,\text{Fe}$ of 0.55, which seems exceptionally high for the rather reducing conditions expected in the mantle. At $Fe^{3+}/\Sigma\,\text{Fe}$ below 0.55, magnetite grains in equilibrium with an average melilitite melt are likely to have $\delta^{56}\text{Fe} \geq 0.10\,‰$. With one exception, all analysed magnetite grains of the SLC melilitite bomb are lighter than $0.10\,‰$, three of the nine analyzed grains are significantly lighter. Magma mixing with an isotopically light carbonatite magma would be one explanation, how the light δ^{56}Fe in magnetite could be achieved. Yet, this isotopic signature can also be explained otherwise:

- The melilitite magma may be derived from an previously altered mantle already depleted in heavy iron isotopes.
- Kinetic iron isotope fractionation in magnetite possibly took place at very low temperatures, when iron diffusion in olivine was already hampered – maybe even during cooling after the eruption.

Thus, the relatively light signatures observed in the magnetite grains are possibly, but not necessarily, indicative of magma mixing with a carbonatite magma. The two heavy magnetite grains found in the SLC melilitite bomb indicate that iron isotope equilibrium between magnetite and the melilitite matrix is not ubiquitously reached. Whether these are exceptions, while most of the magnetite grains reached equilibrium, or whether these grains indicate an overall disequilibrium of δ^{56}Fe in magnetite cannot be answered here. In further investigations, the δ^{56}Fe of the melilitite matrix should be analyzed by a suitable in situ method, to test whether and where isotopic equilibrium was established.

[2]Weyer et al. (2005); Williams et al. (2005); Teng et al. (2008); Heimann et al. (2008); Zhao et al. (2010, 2012); Johnson et al. (2010); Huang et al. (2011); Sossi et al. (2012); Weyer and Seitz (2012); Williams and Bizimis (2014); Chen et al. (2015, 2014); Xiao et al. (2016); Wu et al. (2017); An et al. (2017).

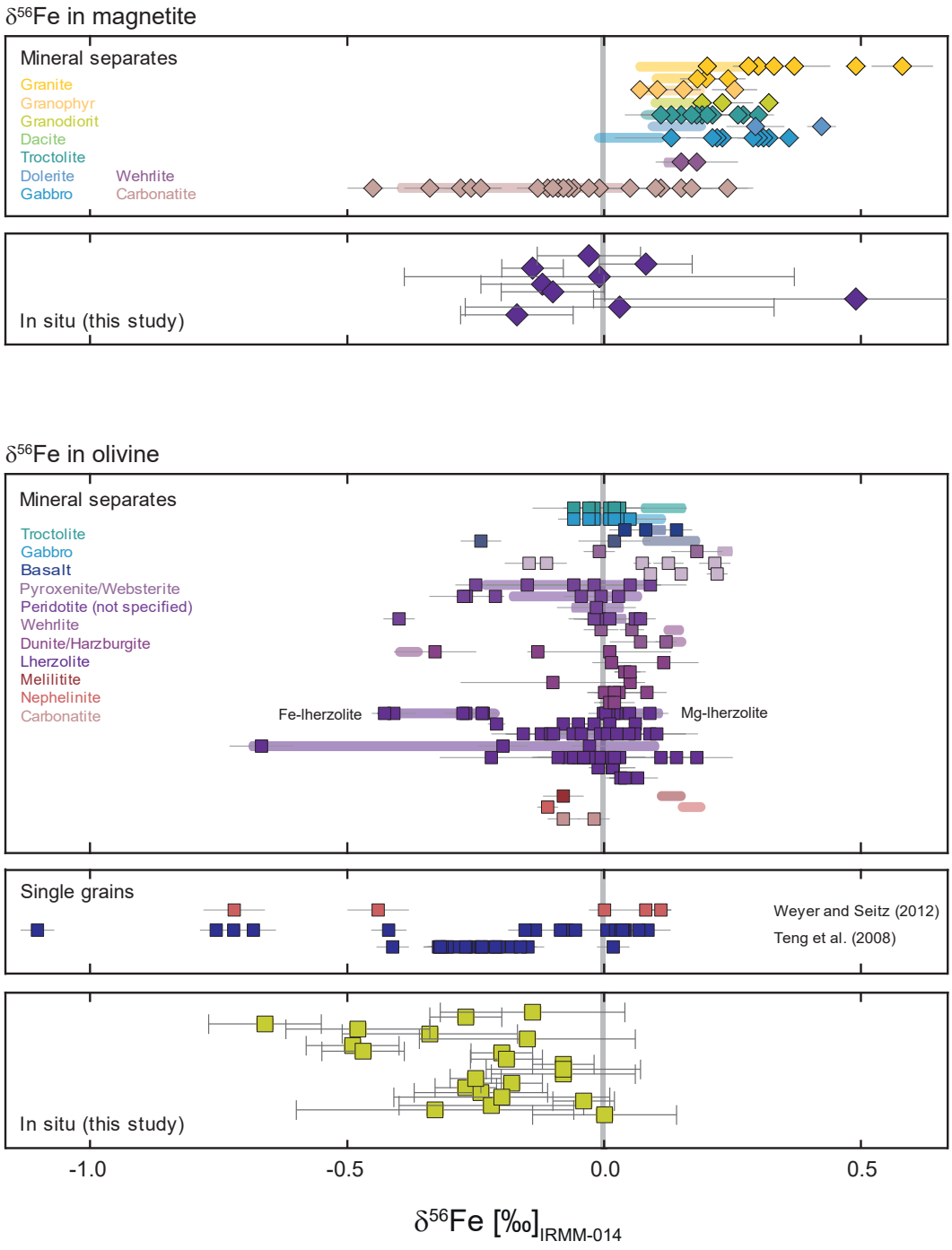

FIGURE 4.3: Comparison of the δ^{56}Fe measured in situ with fs-LA on olivine and magnetite grains with data of mineral separate analyses compiled from literature[2]. The large span in δ^{56}Fe in olivine minerals was observed before in carbonatites and mantle xenoliths. The light iron isotopic signatures observed in this study in the melilitite bomb resemble the observation of isotopically light magnetite grains in carbonatites made by Johnson et al. (2010).

4.4.3 Iron isotope fractionation during carbonatite genesis

Carbonatites are usually of "cumulate nature" (Johnson et al., 2010, pg. 91), meaning that they are the product of multiple steps of magma evolution and magma mixing (see also e. g. Schmidt and Weidendorfer, 2018; Weidendorfer et al., 2016; Gittins, 1989). The most prominent processes that play a role in carbonatite genesis are low-degree partial melting of a carbonated mantle, and differentiation from a carbonated alkaline silicate melt by immiscibility or crystal fractionation (e. g. Brooker and Kjarsgaard, 2011, cf. section 1.1). Carbonatites may originate in various geological settings and undergo rather individual steps of magma evolution[3]. The focus of the following chapter is on iron isotope fractionation that may result from the main mechanisms generating carbonatite melts (Figure 4.4 after Hammouda and Keshav, 2015; Johnson et al., 2010; Weyer, 2008). The first (and to my knowledge only) authors to discuss carbonatite genesis in the context with iron isotope fractionation are Johnson et al. (2010), concluding that most steps in carbonatite genesis contribute to the light isotopic composition they observed in carbonatites. In the following discussion I will revisit their model of carbonatite genesis and combine it with the results of my experiments and findings in recent literature.

Low-degree partial melting

A comprehensive review on "melting in the mantle in the presence of carbon" was written by Hammouda and Keshav (2015), taking into account numerous studies concerned with the origin of carbonatites. In their model, primary carbonatite melts derived from low-degree partial melting of the mantle are unlikely to reach crustal levels. Instead, these primary carbonatite melts are transported at very low degrees of melting (≤ 0.1 %, Minarik and Watson, 1995; Hammouda and Laporte, 2000), which enables them to disseminate into the surrounding mantle. Carbonatitic magmatism in continental areas would then "be caused by thermal perturbation of regions that were subject to prior metasomatism by carbonated melts" (Hammouda and Keshav, 2015, pg. 14). The magnitude of iron isotope fractionation during low-degree partial melting of the mantle is dependent

- on the equilibrium iron isotope fractionation factor between mantle minerals and the carbonatite melt determining the minimum expected iron isotope fractionation, and
- on the underlying mechanism: Kinetic iron isotope fractionation would result in much larger fractionations than expected from equilibrium isotope fractionation.

The possible range of equilibrium iron isotope fractionation is illustrated in Table 4.1, where Δ^{56}Fe for the respective Fe^{2+} and Fe^{3+} endmembers of silicate phases involved in

[3]For a recent review on "CO_2-rich melts in Earth" see also Yaxley et al. (2019).

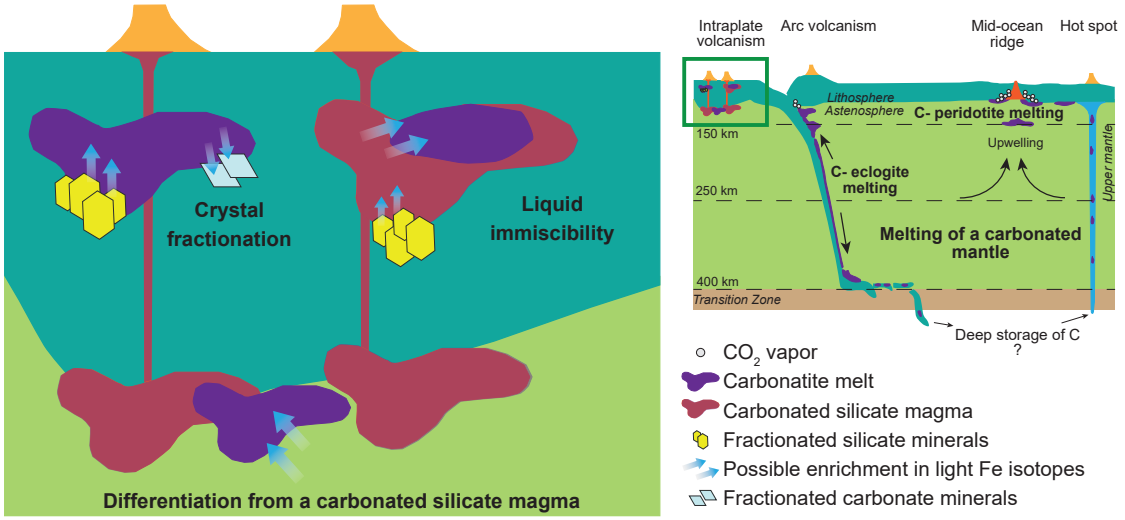

FIGURE 4.4: Left: iron isotope fractionation during carbonatite genesis; right: melting of a carbonated mantle (not to scale; after Hammouda and Keshav, 2015; Johnson et al., 2010; Weyer, 2008). During low-degree melting and by further differentiation of a carbonated silicate melt, light iron isotopes may be enriched in the melt. The equilibrium fractionation factor strongly depends on the redox conditions and on the melt structure. To produce the extremely light δ^{56}Fe in carbonatite rocks observed by Johnson et al. (2010), several steps of equilibrium fractionation or other mechanisms of iron isotope fractionation, e. g. kinetic fractionation, would be necessary. Recent research (e. g. Stagno et al., 2019; Yaxley et al., 2019) has shown that the mobilization of carbon in the mantle is also strongly redox dependent. A better understanding of iron isotope fractionation between silicate and C-bearing phases may therefore help to decipher information preserved in rocks derived from the mantle such as mantle xenoliths and carbonatites.

carbonatite genesis are estimated. While the magnitude of kinetic iron isotope fractionation is dependent on iron transport rates, equilibrium iron isotope fractionation is strongly dependent on redox conditions and $Fe^{3+}/\Sigma Fe$ ratios and thus different in various geological settings. Melts generated by low-degree partial melting in the mantle are usually of dolomitic or calcic composition (e. g. Hammouda and Keshav, 2015, and references therein). This limits the applicability of the experimental results of this thesis to predict iron isotope fractionation during partial melting, since the difference in chemistry to the here investigated natro-carbonatite system may not only affect the magnitude of iron isotope fractionation, but also the iron distribution coefficients between melt and residue, which remain unknown. In lack of data of a calcic or dolomitic carbonatite melt, the β-factor of calcite will be used to approximate the equilibrium fractionation between carbonatite melts and the mantle (Johnson et al., 2010). This should be a valid assumption, since local structural units in melts may be analog to mineral structures of the same chemistry, as it is known from silicate melts (e. g. Dauphas et al., 2014; Sossi and O'Neill, 2017) and was suggested by Pohlenz et al. (2018) for a Na-carbonate melt. In Table 4.1 Δ^{56}Fe are calculated between mantle minerals such as olivine, pyroxene, and garnet and both

calcic (approximated by calcite) and natro-carbonatite melts. At temperatures of 1200 °C, a fractionation of $\Delta^{56}Fe_{min.\text{-}Ca\text{-}carb.\,m.}$ of 0.21 ‰ can be reached. The fractionation between a natro-carbonatite melt and mantle minerals is smaller ($\Delta^{56}Fe_{min.\text{-}Na\text{-}carb.\,m.} \geq 0.05$ ‰), but still light isotopes would be enriched in the carbonatite melt. In the temperature range assumed for mantle melting, equilibration between a carbonatite melt and the average mantle alone is too small to explain $\delta^{56}Fe < -0.2$ ‰. To explain the isotopically extremely light iron isotope signatures found in carbonatites by equilibrium isotope fractionation, a succession of equilibrium fractionation processes is needed, as discussed below.

Johnson et al. (2010) discussed the formation of carbonatite melts in the mantle as an equilibrium process. Yet, considering the high mobility of carbonatite melts at very low melt/rock ratios, a re-equilibration between melt and rock seems unlikely. Carbonatite melts can move as interconnected grain-edge melt-networks (Minarik and Watson, 1995; Gervasoni et al., 2017) and by dissolution-precipitation reactions (Hammouda and Laporte, 2000) and remove rapidly soluble species (like iron) from their source. Hammouda and Laporte (2000) found carbonatite infiltration rates to be as high as D = 1.8 * 10^{-9} m^2s^{-1} at 1300 °C, 1 GPa. Thus, carbonatite melts move faster than iron transport in mantle minerals takes place, e. g. by Fe-Mg interdiffusion in olivine ($D_{Fe\text{-}Mg} = 10^{-16}$ m^2/s at 1200 °C Dohmen and Chakraborty, 2007, cf. subsection 4.4.2). When iron containing carbonatite melts are transported faster than iron isotopic equilibration with the mantle is possible, kinetic isotope fractionation may enrich light iron isotopes in the direction of the transport whereever carbonatite melts and mantle minerals interact.

Low-degree partial carbonatite melts may efficiently redistribute and fractionate iron (isotopes) in the mantle (Beard and Johnson, 2004; Williams et al., 2005; Williams and Bizimis, 2014; Weyer and Ionov, 2007; Zhao et al., 2010, 2015; Poitrasson et al., 2013). Yet, in the model of Hammouda and Keshav (2015) the primary carbonatite melts do not reach surface levels (Figure 4.4, see also Gaillard et al., 2019). This suggests that in addition to low-degree partial melting in the upper mantle, further mechanisms of iron isotope fractionation take effect on the way to the crust. As such, the contribution of liquid immiscibility and crystal fractionation to the light iron isotope compositions of carbonatite rocks are discussed in the next section.

Liquid immiscibility and crystal fractionation

Carbonatite melts can be formed by exsolution from a carbonated silicate melt (Brooker and Kjarsgaard, 2011 and references therein). As the experiments of this thesis have shown, liquid immiscibility between carbonate and silicate melt would result in $\Delta^{56}Fe_{sil.melt\text{-}carb.melt} = 0.13$ ‰, which is too small to generate the negative $\delta^{56}Fe$ observed by Johnson et al. (2010) in carbonatite whole rock samples (e. g. $\delta^{56}Fe$ between – 0.53 ‰ to

and – 0.33 ‰ at Oldoinyo Lengai, Tanzania). Yet, to generate a carbonatite melt by exsolution from a silicate melt, any primary silicate melt needs to pass through several steps of magma evolution to reach the high amount of alkalis required for silicate – carbonate melt immiscibility (Figure 4.4). This can be achieved in alkaline magma suites by fractionation of low-alkali minerals without increasing SiO_2 in the primitive melt (Weidendorfer et al., 2016). The first minerals to fractionate would be olivine and augitic clinopyroxene, followed by oxides like titano-magnetite. With ongoing fractionation, pyroxene will become higher in aegirine content. These steps of magma evolution proposed by Weidendorfer et al. (2016) may already enrich light isotopes in the alkaline silicate melt. Assuming equilibrium isotope fractionation, the formation of olivine and Fe^{2+}-pyroxene would have no effect or shift the melt composition to slightly positive δ^{56}Fe, depending on $Fe^{3+}/\Sigma Fe$ in the melt, but the consequent fractionation of pyroxene with an increasing Fe^{3+} component and the fractionation of magnetite would deprive the melt of heavy isotopes (Table 4.1). Depending on iron distribution between these phases, carbonatites generated by liquid immiscibility may accumulate light δ^{56}Fe as result of several steps of magma differentiation, starting even before the actual step of carbonatite melt exsolution.

Not only crystal fractionation preceding liquid immiscibility of a carbonatite melt from a silicate melt would accumulate light isotopes in the carbonatite melt. Also further crystal fractionation of Fe^{3+}- silicate and oxide minerals would enrich light isotopes in the carbonatite magma. Finally, crystallizing carbonate minerals would enrich light iron isostopes in the carbonate minerals. This would generate an isotopically light carbonatite rock, and possibly leave a fluid with heavy iron isotope composition.

Furthermore, kinetic iron isotope fractionation during the exsolution of a carbonatite melt from a silicate melt needs to be considered as a mechanism to enrich light isotopes in the carbonatite melt. Yet, its contribution is expected to be minor. To produce a kinetic isotope fractionation, transport processes are needed. The experimental results of this thesis support the assumption that the exsolution of a carbonate melt from a silicate melt starts with the formation of microsegregated subnetworks, which are already distributed throughout the silicate melt (Henderson, 1995; Morizet et al., 2017; Moussallam et al., 2016, cf. subsection 4.3.3). Thus only minor transport distances of iron are required to nucleate and grow melt bubbles, minimizing kinetic iron isotope fractionation during melt segregation.

Both low-degree partial melting of the mantle and fractionation of a carbonated silicate melt may enrich light iron isotopes in carbonatite melts. Yet, none of these mechanisms alone can explain the light iron isotope signatures of carbonatites. As carbonatites are generated by several steps of magma evolution, so are their iron isotope signatures.

TABLE 4.1: Estimates of $\Delta^{56}Fe_{min.\text{-}carb.\,melt}$ and $\Delta^{56}Fe_{basaltic\ sil.\ melt–min.}$

Phase	Method	Reference	Force constant [N/m]	$10^3 \ln \beta$ at 1200 °C	$\Delta^{56}Fe_{min.\text{-}carb.\,m.}$ [‰]		$\Delta^{56}Fe_{basaltic\ sil.\ m.–min.}$ [‰]		
					natro-carbonatite	calcic composition	Fe^{2+} endmember	$Fe^{3+}/\Sigma Fe = 0.25$	Fe^{3+} endmember
Forsterite	NRIXS	Dauphas et al. (2014)		0.26	0.08	0.21	0.00	0.05	0.20
Fayalite	NRIXS	Sossi and O'Neill (2017)	178	0.23	0.05	0.18	0.03	0.08	0.23
Enstatite (as Fe^{2+} endmember)	NRIXS	Dauphas et al. (2012)		0.23	0.05	0.18	0.03	0.08	0.23
Aegirine (as Fe^{3+} endmember)	Mössbauer	Polyakov and Mineev (2000)		0.36	0.18	0.31	-0.10	-0.05	0.10
Almandine	NRIXS	Sossi and O'Neill (2017)	147	0.19	0.01	0.14	0.07	0.12	0.27
MgFeAl spinel (Fe^{2+} endmember)	NRIXS	Roskosz et al. (2015)		0.25	0.07	0.20	0.01	0.06	0.21
MgFeAl spinel (Fe^{3+} endmember)	NRIXS	Roskosz et al. (2015)		0.40	0.22	0.35	-0.14	-0.09	0.06
Magnetite	NRIXS	Sossi and O'Neill (2017)	292	0.38	0.20	0.33	-0.12	-0.07	0.08
Siderite	Mössbauer	Polyakov and Mineev (2000)		0.17	-0.01	(0.12)	-	-	-
Ankerite	Mössbauer	Polyakov and Mineev (2000)		0.11	-0.07	(0.06)	-	-	-
Calcite	estimated *	Johnson et al. (2010)		0.05	-0.13	(0.00)	-	-	-
Basalt, andesite, dacite (Fe^{2+} endmember)	NRIXS	Dauphas et al. (2014)	199	0.26	-	-	-	-	-
Basalt, andesite, dacite (Fe^{3+} endmember)	NRIXS	Dauphas et al. (2014)	351	0.46	-	-	-	-	-

*calculated under the assumtion that iron isotope fractionation between magnetite and calcite varies linearly with iron content

5 Conclusion and outlook

The experimental studies of iron isotope partitioning between immiscible silicate and carbonate melts at magmatic conditions (at pressures of 0.5 and 0.7 GPa and temperatures between 900 and 1200 °C) have shown that light isotopes are enriched in the carbonatite melt. The highest $\Delta^{56}Fe_{\text{sil.m.-carb.m. (mean)}}$ of 0.13 ‰ was determined in system BR (ASI $\geq$ 0.21, Na/Al $\leq$ 2.7), the lowest $\Delta^{56}Fe_{\text{sil.m.-carb.m. (mean)}}$ of 0.02 ‰ was determined in system KGW_{lAl+Fe} (ASI $\leq$ 0.11 , Na/Al $\geq$ 6.1). Iron isotope fractionation between carbonatite and silicate melts falls in the expected range (c. f. Table 4.1) in the systems BR, Sp, and KGW_{highAl}. Most likely this behaviour is governed by the redox conditions of the system, which strongly influence iron isotope fractionation (Dauphas et al., 2014; Roskosz et al., 2015; Sossi and O'Neill, 2017, and others).

No significant iron isotope fractionation occurs in systems with extremely high sodium contents (systems KGW_{lowAl}, KGW_{lAl+Fe}, KGW_{lAl+Ca}). This may indicate structural differences in the silicate melt, i. e. the formation of microsegregated subnetworks (c. f. Henderson, 1995; Morizet et al., 2017; Moussallam et al., 2016; Pohlenz et al., 2018) and possibly the accomodation of iron in free ionic carbonate groups (FIC). This study indicates that structural differences induced by compositional changes may overrule the influence of redox conditions and thus need to be considered in the interpretation of iron isotope data. Therefore, the iron isotope system holds the potential to be useful not only for exploring redox conditions in magmatic systems, but also for discovering structural changes in a melt.

The in situ iron isotope analyses of olivine and magnetite grains of a melilitite bomb from the SLC show that olivine and magnetite grains hold different informations regarding kinetic and equilibrium fractionation due to their different Fe diffusion coefficients. Furthermore, this study shows once more that a large variability of δ^{56}Fe may be found even on a small scale, which emphasizes the importance of in situ iron isotope analyses.

The observations made in the experiments and in the in situ iron isotope analyses suggest that the extremely light iron isotope signatures found in carbonatites can not be explained by one step of equilibrium isotope fractionation. The light iron isotopic signatures are rather genereated by several steps of isotope fractionation during carbonatite genesis, which may involve equilibrium and kinetic fractionation. Since iron isotopic signatures in natural systems are generated by a combination of multiple factors (pressure, temperature, redox conditions, phase composition and structure, time scale), multi tracer approaches

are needed to explain signatures found in natural rocks. The complexity of the iron isotope fractionation mechanisms requires more experimental investigations to understand the interaction of the multitude of factors. This thesis has provided one more piece in this puzzle.

5.1 Outstanding questions

The most important questions left open by this thesis as well as the most promising starting points for further research are summarized in the following:

- The capsule design employing a Re-inlay allows the investigation of carbonatite systems including iron.
- As the experiments have shown, the magnitude of iron isotope fractionation is strongly related to chemical and redox composition and melt structure. The presence of additional components such as halogenides or phosphorus, abundant in natural carbonatite systems, may have a strong influence on the structure of silicate and carbonate melts and thus on iron isotope fractionation.
- The assumption that the carbon- and alkali-rich silicate melt falls on the same iron isotope fractionation line as the basalt glasses investigated by Dauphas et al. (2014) may be incorrect. It would be interesting to measure the force constants of iron in the BR glasses directly by NRIXS and to determine the $Fe^{3+}/\Sigma Fe$ by Mössbauer spectroscopy.
- In this thesis $\Delta^{56}Fe_{\text{min.-carb. m.}}$ of natro-carbonatite systems were determined. Natro-carbonatite melts are not representative for melts generated by low-degree melting of a carbonated mantle, which would be of dolomitic or calcic carbonatite composition (Hammouda and Keshav, 2015 and references therein). Further research should include these systems. Furthermore, carbon plays an important role in transport processes throughout the mantle, which are linked to observations of "large heterogeneities in mantle redox state, both vertically and laterally" (Stagno et al., 2019, p. 79). To be able to explore the influence of these processes on the iron isotopic composition of the mantle, iron isotope fractionation in further carbon bearing phases should be investigated.
- The in situ analyses of iron isotope ratios in mantle xenoliths should be investigated systematically and include a possibly large variety of minerals.

Bibliography

Alberto, H., Da Cunha, J. P., Mysen, B., Gil, J., and De Campos, N. A. (1996). Analysis of Mössbauer spectra of silicate glasses using a two-dimensional Gaussian distribution of hyperfine parameters. *Journal of Non-Crystalline Solids*, 194(1):48–57.

An, Y., Huang, J.-X., Griffin, W., Liu, C., and Huang, F. (2017). Isotopic composition of Mg and Fe in garnet peridotites from the Kaapvaal and Siberian cratons. *Geochimica et Cosmochimica Acta*, 200:167–185.

Beard, B. L. and Johnson, C. M. (2004). Inter-mineral Fe isotope variations in mantle-derived rocks and implications for the Fe geochemical cycle. *Geochimica et Cosmochimica Acta*, 68(22):4727–4743.

Bell, K., editor (1989). *Carbonatites: genesis and evolution*. Unwin Hyman Ltd.

Bell, K., Kjarsgaard, B. A., and Simonetti, A. (1998). Carbonatites – Into the Twenty-First Century. *Journal of Petrology*, 39(11):1839–1845.

Bell, K. and Simonetti, A. (2010). Source of parental melts to carbonatites – critical isotopic constraints. *Mineralogy and Petrology*, 98(1):77–89.

Bell, K. and Tilton, G. R. (2001). Nd, Pb and Sr Isotopic Compositions of East African Carbonatites: Evidence for Mantle Mixing and Plume Inhomogeneity. *Journal of Petrology*, 42(10):1927–1945.

Bigeleisen, J. and Goeppert-Mayer, M. (1947). Calculation of Equilibrium Constants for Isotopic Exchange Reaktions. *Journal of Chemical Physics*, 15:261–267.

Blanchard, M., Poitrasson, F., Méheut, M., Lazzeri, M., Mauri, F., and Balan, E. (2009). Iron isotope fractionation between pyrite (FeS_2), hematite (Fe_2O_3) and siderite ($FeCO_3$): A first-principles density functional theory study. *Geochimica et Cosmochimica Acta*, 73(21):6565–6578.

Bodeving, S., Williams-Jones, A. E., and Swinden, S. (2017). Carbonate-silicate melt immiscibility, REE mineralising fluids, and the evolution of the Lofdal Intrusive Suite, Namibia. *Lithos*, 268:383–398.

Borchert, M., Wilke, M., Schmidt, C., and Rickers, K. (2010). Rb and Sr partitioning between haplogranitic melts and aqueous solutions. *Geochimica et Cosmochimica Acta*, 74(3):1057–1076.

Borisov, A., Behrens, H., and Holtz, F. (2017). Effects of strong network modifiers on Fe^{3+}/Fe^{2+} in silicate melts: an experimental study. *Contributions to Mineralogy and Petrology*, 172(5):34.

Borisov, A. and Jones, J. H. (1999). An evaluation of Re, as an alternative to Pt, for the 1 bar loop technique: An experimental study at 1400 °C. *American Mineralogist*, 84:1528–1534.

Borisov, A. and McCammon, C. (2010). The effect of silica on ferric/ferrous ratio in silicate melts: An experimental study using Mössbauer spectroscopy. *American Mineralogist*, 95(4):545–555.

Brey, G. and Green, D. H. (1975). The role of CO_2 in the genesis of olivine melilitite. *Contributions to Mineralogy and Petrology*, 49(2):93–103.

Brooker, R., Kohn, S., Holloway, J., and McMillan, P. (2001a). Structural controls on the solubility of CO_2 in silicate melts: Part I: bulk solubility data. *Chemical Geology*, 174(1):225–239. 6th International Silicate Melt Workshop.

Brooker, R., Kohn, S., Holloway, J., and McMillan, P. (2001b). Structural controls on the solubility of CO_2 in silicate melts: Part II: IR characteristics of carbonate groups in silicate glasses. *Chemical Geology*, 174(1):241–254. 6th International Silicate Melt Workshop.

Brooker, R. A. (1998). The Effect of CO_2 Saturation on Immiscibility between Silicate and Carbonate Liquids: an Experimental Study. *Journal of Petrology*, 39(11-12):1905–1915.

Brooker, R. A. and Kjarsgaard, B. A. (2011). Silicate-Carbonate Liquid Immiscibility and Phase Relations in the System SiO_2-Na_2O-Al_2O_3-CaO-CO_2 at 0.1-2.5 GPa with Applications to Carbonatite Genesis. *Journal of Petrology*, 52:1281–1305.

Chen, C., Su, B.-X., Uysal, I., Avcı, E., Zhang, P.-F., Xiao, Y., and He, Y.-S. (2015). Iron isotopic constraints on the origin of peridotite and chromitite in the Kızıldağ ophiolite, southern Turkey. *Chemical Geology*, 417:115–124.

Chen, L.-M., Song, X.-Y., Zhu, X.-K., Zhang, X.-Q., Yu, S.-Y., and Yi, J.-N. (2014). Iron isotope fractionation during crystallization and sub-solidus re-equilibration: Constraints from the Baima mafic layered intrusion, SW China. *Chemical Geology*, 380:97–109.

Chou, I.-M. (1986). Permeability of precious metals to hydrogen at 2 kb total pressure and elevated temperatures. *American Journal of Science*, 286(8):638–658.

Churakov, S. and Gottschalk, M. (2003a). Perturbation theory based equation of state for polar molecular fluids: I. Pure fluids. *Geochimica et Cosmochimica Acta*, 67(13):2397–2414.

Churakov, S. and Gottschalk, M. (2003b). Perturbation theory based equation of state for polar molecular fluids: II. Fluid mixtures. *Geochimica et Cosmochimica Acta*, 67(13):2415–2425.

Craddock, P. R., Warren, J. M., and Dauphas, N. (2013). Abyssal peridotites reveal the near-chondritic Fe isotopic composition of the Earth. *Earth and Planetary Science Letters*, 365:63–76.

Criss, R. (1999). *Principles of Stable Isotope Distribution*. Oxford University Press.

Criss, R., Gregory, R., and Taylor, H. (1987). Kinetic theory of oxygen isotopic exchange between minerals and water. *Geochimica et Cosmochimica Acta*, 51(5):1099–1108.

Dasgupta, R., Hirschmann, M. M., and Smith, N. D. (2007). Partial melting experiments of peridotite + CO_2 at 3 GPa and genesis of alkalic ocean island basalts. *Journal of Petrology*, 48(11):2093–2124.

Dauphas, N., Craddock, P. R., Asimow, P. D., Bennett, V. C., Nutman, A. P., and Ohnenstetter, D. (2009). Iron isotopes may reveal the redox conditions of mantle melting from Archean to Present. *Earth and Planetary Science Letters*, 288(1–2):255–267.

Dauphas, N., John, S. G., and Rouxel, O. (2017). Iron Isotope Systematics. *Reviews in Mineralogy and Geochemistry*, 82(1):415–510.

Dauphas, N., Roskosz, M., Alp, E., Golden, D., Sio, C., Tissot, F., Hu, M., Zhao, J., Gao, L., and Morris, R. (2012). A general moment NRIXS approach to the determination of equilibrium Fe isotopic fractionation factors: Application to goethite and jarosite. *Geochimica et Cosmochimica Acta*, 94:254–275.

Dauphas, N., Roskosz, M., Alp, E., Neuville, D., Hu, M., Sio, C., Tissot, F., Zhao, J., Tissandier, L., Médard, E., and Cordier, C. (2014). Magma redox and structural controls on iron isotope variations in Earth's mantle and crust. *Earth and Planetary Science Letters*, 398:127–140.

Dawson, J. (1962). The geology of Oldoinyo Lengai. *Bulletin Volcanologique*, 24(1):349–387.

de Moor, J. M., Fischer, T. P., King, P. L., Botcharnikov, R. E., Hervig, R. L., Hilton, D. R., Barry, P. H., Mangasini, F., and Ramirez, C. (2013). Volatile-rich silicate melts from

Oldoinyo Lengai volcano (Tanzania): Implications for carbonatite genesis and eruptive behavior. *Earth and Planetary Science Letters*, 361:379–390.

Dieckmann, R. and Schmalzried, H. (1977). Defects and Cation Diffusion in Magnetite (I). *Berichte der Bunsengesellschaft für physikalische Chemie*, 81(3):344–347.

Dobson, D. P., Jones, A. P., Rabe, R., Sekine, T., Kurita, K., Taniguchi, T., Kondo, T., Kato, T., Shimomura, O., and Urakawa, S. (1996). In-situ measurement of viscosity and density of carbonate melts at high pressure. *Earth and Planetary Science Letters*, 143(1–4):207–215.

Dohmen, R. and Chakraborty, S. (2007). Fe–Mg diffusion in olivine II: point defect chemistry, change of diffusion mechanisms and a model for calculation of diffusion coefficients in natural olivine. *Physics and Chemistry of Minerals*, 34(6):409–430.

Dyar, M. D. (1985). A review of Mössbauer data on inorganic glasses: the effects of composition on iron valency and coordination. *American Mineralogist*, 70(3-4):304–316.

Dziony, W., Horn, I., Lattard, D., Koepke, J., Steinhoefel, G., Schuessler, J. A., and Holtz, F. (2014). In-situ Fe isotope ratio determination in Fe-Ti oxides and sulfides from drilled gabbros and basalt from the IODP Hole 1256D in the eastern equatorial Pacific. *Chemical Geology*, 363:101–113.

Farges, F., Lefrère, Y., Rossano, S., Berthereau, A., Calas, G., and Brown, G. E. (2004). The effect of redox state on the local structural environment of iron in silicate glasses: a combined XAFS spectroscopy, molecular dynamics, and bond valence study. *Journal of Non-Crystalline Solids*, 344(3):176–188.

Flood, H. and Foerland, T. (1947). The acidic and basic properties of oxides. *Acta Chemica Scandinavica*, 1:592–604.

Foden, J., Sossi, P. A., and Wawryk, C. M. (2015). Fe isotopes and the contrasting petrogenesis of A-, I- and S-type granite. *Lithos*, 212–215:32–44.

Freestone, I. and Hamilton, D. (1980). The role of liquid immiscibility in the genesis of carbonatites – An experimental study. *Contributions to Mineralogy and Petrology*, 73(2):105–117.

French, B. M. (1971). Stability relations of siderite ($FeCO_3$) in the system Fe-C-O. *American Journal of Science*, 271(1):37–78.

Gaillard, F., Sator, N., Gardés, E., Guillot, B., Massuyeau, M., Sifré, D., Hammouda, T., and Richard, G. (2019). The Link between the Physical and Chemical Properties of Carbon-Bearing Melts and Their Application for Geophysical Imaging of Earth's Mantle. *Deep Carbon: Past to Present*, pages 163–187.

Genge, M. J., Jones, A. P., and Price, G. (1995a). An infrared and Raman study of carbonate glasses: implications for the structure of carbonatite magmas. *Geochimica et Cosmochimica Acta*, 59(5):927–937.

Genge, M. J., Price, G., and Jones, A. P. (1995b). Molecular dynamics simulations of $CaCO_3$ melts to mantle pressures and temperatures: implications for carbonatite magmas. *Earth and Planetary Science Letters*, 131(3–4):225–238.

Gervasoni, F., Klemme, S., Rohrbach, A., Grützner, T., and Berndt, J. (2017). Experimental constraints on mantle metasomatism caused by silicate and carbonate melts. *Lithos*, 282:173–186.

Gittins, J. (1989). The Origin and Evolution of Carbonatite Magmas. In Bell, K., editor, *Carbonatites: Genesis and Evolution*. Unwin Hyman Ltd.

Gottschalk, M. (1997). Internally consistent thermodynamic data for rock-forming minerals in the system SiO_2-TiO_2-Al_2O_3-Fe_2O_3-CaO-MgO-FeO-K_2O-Na_2O-H_2O-CO_2. *European Journal of Mineralogy*, 9:175–223.

Hamilton, D. L., Freestone, I. C., Dawston, J. B., and Donaldson, C. H. (1979). Origin of carbonatites by Liquid immiscibility. *Nature*, 279:52–54.

Hammouda, T. and Keshav, S. (2015). Melting in the mantle in the presence of carbon: Review of experiments and discussion on the origin of carbonatites. *Chemical Geology*, 418:171–188.

Hammouda, T. and Laporte, D. (2000). Ultrafast mantle impregnation by carbonatite melts. *Geology*, 28(3):283–285.

Harmer, R. E. and Gittins, J. (1998). The Case for Primary, Mantle-derived Carbonatite Magma. *Journal of Petrology*, 39(11-12):1895–1903.

Heimann, A., Beard, B. L., and Johnson, C. M. (2008). The role of volatile exsolution and sub-solidus fluid/rock interactions in producing high $^{56}Fe/^{54}Fe$ ratios in siliceous igneous rocks. *Geochimica et Cosmochimica Acta*, 72(17):4379–4396.

Henderson, G. (1995). A Si K-edge EXAFS/XANES study of sodium silicate glasses. *Journal of Non-Crystalline Solids*, 183(1):43–50.

Henderson, G. S. (2005). The Structure of silicate melts: A glass perspective. *The Canadian Mineralogist*, 43(6):1921.

Hirose, K. (1997). Partial melt compositions of carbonated peridotite at 3 GPa and role of CO_2 in alkali-basalt magma generation. *Geophysical Research Letters*, 24(22):2837–2840.

Holland, T. and Powell, R. (2011). An improved and extended internally consistent thermodynamic dataset for phases of petrological interest, involving a new equation of state for solids. *Journal of Metamorphic Geology*, 29(3):333–383.

Horn, I., von Blanckenburg, F., Schoenberg, R., Steinhoefel, G., and Markl, G. (2006). In situ iron isotope ratio determination using UV-femtosecond laser ablation with application to hydrothermal ore formation processes. *Geochimica et Cosmochimica Acta*, 70(14):3677–3688.

Huang, F., Lundstrom, C., Glessner, J., Ianno, A., Boudreau, A., Li, J., Ferré, E., Marshak, S., and DeFrates, J. (2009). Chemical and isotopic fractionation of wet andesite in a temperature gradient: Experiments and models suggesting a new mechanism of magma differentiation. *Geochimica et Cosmochimica Acta*, 73(3):729–749.

Huang, F., Zhang, Z., Lundstrom, C. C., and Zhi, X. (2011). Iron and magnesium isotopic compositions of peridotite xenoliths from Eastern China. *Geochimica et Cosmochimica Acta*, 75(12):3318–3334.

Hudon, P. and Baker, D. R. (2002a). The nature of phase separation in binary oxide melts and glasses. I. Silicate systems. *Journal of Non-Crystalline Solids*, 303(3):299–345.

Hudon, P. and Baker, D. R. (2002b). The nature of phase separation in binary oxide melts and glasses. II. Selective solution mechanism. *Journal of Non-Crystalline Solids*, 303(3):346–353.

Hunter, R. H. and McKenzie, D. (1989). The equilibrium geometry of carbonate melts in rocks of mantle composition. *Earth and Planetary Science Letters*, 92(3–4):347–356.

Jochum, K. P., Nohl, U., Herwig, K., Lammel, E., Stoll, B., and Hofmann, A. W. (2005). GeoReM: A New Geochemical Database for Reference Materials and Isotopic Standards. *Geostandards and Geoanalytical Research*, 29(3):333–338.

Johnson, C., Beard, B., Weyer, S., et al. (2020). *Iron Geochemistry: An Isotopic Perspective*. Springer.

Johnson, C. M., Beard, B. L., and Albarède, F. (2004). Overview and General Concepts. *Reviews in Mineralogy and Geochemistry*, 55:1–24.

Johnson, C. M., Bell, K., Beard, B. L., and Shultis, A. I. (2010). Iron isotope compositions of carbonatites record melt generation, crystallization, and late-stage volatile-transport processes. *Mineralogy and Petrology*, 98:91–110.

Jones, A. P., Dobson, D., and Genge, M. (1995). Comment on physical properties of carbonatite magmas inferred from molten salt data, and application to extraction patterns from carbonatite-silicate magma chambers. *Geological Magazine*, 132:121–121.

Jones, A. P., Genge, M., and Carmody, L. (2013). Carbonate Melts and Carbonatites. *Reviews in Mineralogy and Geochemistry*, 75(1):289–322.

Kim, H.-I., Sur, J. C., and Lee, S. K. (2016). Effect of iron content on the structure and disorder of iron-bearing sodium silicate glasses: A high-resolution ^{2}9Si and ^{17}O solid-state NMR study. *Geochimica et Cosmochimica Acta*, 173:160–180.

Kjarsgaard, B. A. (1998). Phase relations of a Carbonated High-CaO Nephelinite at 0.2 and 0.5 GPa. *Journal of Petrology*, 39(11-12):2061–2075.

Knipping, J. L., Behrens, H., Wilke, M., Göttlicher, J., and Stabile, P. (2015). Effect of oxygen fugacity on the coordination and oxidation state of iron in alkali bearing silicate melts. *Chemical Geology*, 411:143–154.

Koster van Groos, A. F. and Wyllie, P. J. (1966). Liquid Immiscibility in the system Na_2O–Al_2O_3–SiO_2–CO_2 at pressures to 1 kilobar. *American Journal of Science*, 264:234–255.

Koster van Groos, A. F. and Wyllie, P. J. (1973). Liquid immiscibility in the join $NaAlSi_3O_8$–$CaAl_2Si_2O_8$–Na_2CO_3–H_2O. *American Journal of Science*, 273:465–487.

Kress, V. C. and Carmichael, I. S. (1991). The compressibility of silicate liquids containing Fe_2O_3 and the effect of composition, temperature, oxygen fugacity and pressure on their redox states. *Contributions to Mineralogy and Petrology*, 108(1-2):82–92.

Lagarec, K. and Rancourt, D. (1997). Extended Voigt-based analytic lineshape method for determining N-dimensional correlated hyperfine parameter distributions in Mössbauer spectroscopy. *Nuclear Instruments and Methods in Physics Research Section B: Beam Interactions with Materials and Atoms*, 129(2):266–280.

Lee, W.-J. and Wyllie, P. J. (1997). Liquid immiscibility between nephelinite and carbonatite from 1.0 to 2.5 GPa compared with mantle melt compositions. *Contributions to Mineralogy and Petrology*, 127(1-2):1–16.

Li, Q., Borup, F., Petrushina, I., and Bjerrum, N. J. (1999). Complex formation during dissolution of metal oxides in molten alkali carbonates. *Journal of The Electrochemical Society*, 146(7):2449–2454.

Li, W.-Y., Teng, F.-Z., Halama, R., Keller, J., and Klaudius, J. (2016). Magnesium isotope fractionation during carbonatite magmatism at Oldoinyo Lengai, Tanzania. *Earth and Planetary Science Letters*, 444:26–33.

Liu, D., Zhao, Z., Zhu, D.-C., Niu, Y., Widom, E., Teng, F.-Z., DePaolo, D. J., Ke, S., Xu, J.-F., Wang, Q., and Mo, X. (2015a). Identifying mantle carbonatite metasomatism through Os-Sr-Mg isotopes in Tibetan ultrapotassic rocks. *Earth and Planetary Science Letters*, 430:458–469.

Liu, J., Lin, J.-F., and Prakapenka, V. B. (2015b). High-Pressure Orthorhombic Ferromagnesite as a Potential Deep-Mantle Carbon Carrier. *Scientific Reports*, 5:7640.

Macris, C. A., Manning, C. E., and Young, E. D. (2015). Crystal chemical constraints on inter-mineral Fe isotope fractionation and implications for Fe isotope disequilibrium in San Carlos mantle xenoliths. *Geochimica et Cosmochimica Acta*, 154:168–185.

Martin, L. H., Schmidt, M. W., Mattsson, H. B., Ulmer, P., Hametner, K., and Günther, D. (2012). Element partitioning between immiscible carbonatite-kamafugite melts with application to the Italian ultrapotassic suite. *Chemical Geology*, 320–321:96–112.

Martin, L. H. J., Schmidt, M. W., Mattsson, H. B., and Guenther, D. (2013). Element Partitioning between Immiscible Carbonatite and Silicate Melts for Dry and H_2O-bearing Systems at 1 – 3 GPa. *Jounal of Petrology*, 54(11):1–38.

Matsukage, K. N. and Kubo, K. (2003). Chromian spinel during melting experiments of dry peridotite KLB-1) at 1.0–2.5 GPa. *American Mineralogist*, 88(8-9):1271–1278.

McCanta, M. C., Dyar, M. D., Rutherford, M. J., and Delaney, J. S. (2004). Iron partitioning between basaltic melts and clinopyroxene as a function of oxygen fugacity. *American Mineralogist*, 89(11-12):1685–1693.

Minarik, W. G. and Watson, E. (1995). Interconnectivity of carbonate melt at low melt fraction. *Earth and Planetary Science Letters*, 133(3–4):423–437.

Mitchell, R. H. (2005). Carbonatites and Carbonatites and Carbonatites. *The Canadian Mineralogist*, 43(6):2049–2068.

Moeller, K., Schoenberg, R., Grenne, T., Thorseth, I. H., Drost, K., and Pedersen, R. B. (2014). Comparison of iron isotope variations in modern and Ordovician siliceous Fe oxyhydroxide deposits. *Geochimica et Cosmochimica Acta*, 126:422–440.

Morizet, Y., Paris, M., Sifre, D., Carlo, I. D., Ory, S., and Gaillard, F. (2017). Towards the reconciliation of viscosity change and CO_2-induced polymerization in silicate melts. *Chemical Geology*, 458:38–47.

Morizet, Y., Vuilleumier, R., and Paris, M. (2015). A NMR and molecular dynamics study of CO_2-bearing basaltic melts and glasses. *Chemical Geology*, 418:89–103.

Moussallam, Y., Florian, P., Corradini, D., Morizet, Y., Sator, N., Vuilleumier, R., Guillot, B., Iacono-Marziano, G., Schmidt, B. C., and Gaillard, F. (2016). The molecular structure of melts along the carbonatite-kimberlite-basalt compositional joint: CO_2 and polymerisation. *Earth and Planetary Science Letters*, 434:129–140.

Murdoch, J. B., Stebbins, J. F., and Carmichael, I. S. E. (1985). High-resolution ^{29}Si NMR study of silicate and aluminosilicate glasses: the effect of network-modifying cations. *American Mineralogist*, 70:332–343.

Mysen, B. O., Virgo, D., and Scarfe, C. M. (1980). Relations between the anionic structure and viscosity of silicate melts – a Raman spectroscopic study. *American Mineralogist*, 65(7-8):690–710.

Mysen, B. O., Virgo, D., and Seifert, F. A. (1985). Relationships between properties and structure of aluminosilicate melts. *American Mineralogist*, 70:88–105.

Nebel, O., Sossi, P., Bénard, A., Wille, M., Vroon, P., and Arculus, R. (2015). Redox-variability and controls in subduction zones from an iron-isotope perspective. *Earth and Planetary Science Letters*, 432:142–151.

Oeser, M., Dohmen, R., Horn, I., Schuth, S., and Weyer, S. (2015). Processes and time scales of magmatic evolution as revealed by Fe-Mg chemical and isotopic zoning in natural olivines. *Geochimica et Cosmochimica Acta*, 154:130–150.

Oeser, M., Ruprecht, P., and Weyer, S. (2018). Combined Fe-Mg chemical and isotopic zoning in olivine constraining magma mixing-to-eruption timescales for the continental arc volcano Irazú (Costa Rica) and Cr diffusion in olivine. *American Mineralogist*, 103(4):582–599.

Oeser, M., Weyer, S., Horn, I., and Schuth, S. (2014). High-Precision Fe and Mg Isotope Ratios of Silicate Reference Glasses Determined In Situ by Femtosecond LA-MC-ICP-MS and by Solution Nebulisation MC-ICP-MS. *Geostandards and Geoanalytical Research*, 38(3):311–328.

Okabayashi, S., Yokoyama, T. D., Kon, Y., Yamamoto, S., Yokoyama, T., and Hirata, T. (2011). Evaluation of Laser Ablation in Liquid (LAL) technique as a new sampling technique for elemental and isotopic analysis using ICP-mass spectrometry. *Journal of Analytical Atomic Spectrometry*, 26:1393–1400.

Orfield, M. L. and Shores, D. A. (1989). The Solubility of NiO in Binary Mixtures of Molten Carbonates. *Journal of the Electrochemical Society*, 136(10):2862–2866.

Pohlenz, J., Rosa, A., Mathon, O., Pascarelli, S., Belin, S., Landrot, G., Murzin, V., Veligzhanin, A., Shiryaev, A., Irifune, T., and Wilke, M. (2018). Structural controls of CO_2 on Y, La and Sr incorporation in sodium-rich silicate - carbonate melts by in-situ high P-T EXAFS. *Chemical Geology*, 486:1–15.

Poitrasson, F., Delpech, G., and Gregoire, M. (2013). On the iron isotope heterogeneity of lithospheric mantle xenoliths: implications for mantle metasomatism, the origin of basalts and the iron isotope composition of the Earth. *Contributions to Mineralogy and Petrology*, 165(6):1243–1258.

Poitrasson, F. and Freydier, R. (2005). Heavy iron isotope composition of granites determined by high resolution MC-ICP-MS. *Chemical Geology*, 222(1):132–147.

Polyakov, V., Clayton, R., Horita, J., and Mineev, S. (2007). Equilibrium iron isotope fractionation factors of minerals: Reevaluation from the data of nuclear inelastic resonant X-ray scattering and Mössbauer spectroscopy. *Geochimica et Cosmochimica Acta*, 71(15):3833–3846.

Polyakov, V. B. and Mineev, S. D. (2000). The use of Mössbauer spectroscopy in stable isotope geochemistry. *Geochimica et Cosmochimica Acta*, 64(5):849–865.

Potter, N. J., Kamenetsky, V. S., Simonetti, A., and Goemann, K. (2017). Different types of liquid immiscibility in carbonatite magmas: A case study of the Oldoinyo Lengai 1993 lava and melt inclusions. *Chemical Geology*, 455:376–384.

Powell, J., Hurley, P., and Fairbairn, H. (1962). Isotopic composition of strontium in carbonatites. *Nature*, 196:1085–1086.

Pownceby, M. I. and O'Neill, H. S. C. (1994). Thermodynamic data from redox reactions at high temperatures. IV. Calibration of the Re-ReO_2 oxygen buffer from EMF and NiO + Ni-Pd redox sensor measurements. *Contributions to Mineralogy and Petrology*, 118(2):130–137.

Prescher, C., McCammon, C., and Dubrovinsky, L. (2012). MossA: a program for analyzing energy-domain Mössbauer spectra from conventional and synchrotron sources. *Journal of Applied Crystallography*, 45(2):329–331.

Richter, F. M., Davis, A. M., DePaolo, D. J., and Watson, E. (2003). Isotope fractionation by chemical diffusion between molten basalt and rhyolite. *Geochimica et Cosmochimica Acta*, 67(20):3905–3923.

Robie, R., Hemingway, B., and Fisher, J. (1995). *Thermodynamic properties of minerals and related substances at 298.15 K and 1 bar (10^5 pascals) pressure and at higher temperatures*. U.S. Geological Survey Bulletin 2131. United States Government Printing Office.

Rocholl, A., Heusser, E., Kirsten, T., Oehm, J., and Richter, H. (1996). A noble gas profile across a Hawaiian mantle xenolith: Coexisting accidental and cognate noble gases derived from the lithospheric and asthenospheric mantle beneath Oahu. *Geochimica et Cosmochimica Acta*, 60(23):4773–4783.

Roskosz, M., Sio, C. K., Dauphas, N., Bi, W., Tissot, F. L., Hu, M. Y., Zhao, J., and Alp, E. E. (2015). Spinel-olivine-pyroxene equilibrium iron isotopic fractionation and applications to natural peridotites. *Geochimica et Cosmochimica Acta*, 169:184–199.

Schauble, E. (2004). Applying Stable Isotope Fractionation Theory to New Systems. *Reviews in Mineralogy and Geochemistry*, 55:65–111.

Schauble, E., Rossman, G., and Jr, H. T. (2001). Theoretical estimates of equilibrium Fe-isotope fractionations from vibrational spectroscopy. *Geochimica et Cosmochimica Acta*, 65(15):2487–2497.

Schmidt, M. W. and Weidendorfer, D. (2018). Carbonatites in oceanic hotspots. *Geology*, 46(5):435–438.

Schoenberg, R. and von Blanckenburg, F. (2005). An assessment of the accuracy of stable Fe isotope ratio measurements on samples with organic and inorganic matrices by high-resolution multicollector ICP-MS. *International Journal of Mass Spectrometry*, 242(2–3):257–272.

Schoenberg, R. and von Blanckenburg, F. (2006). Modes of planetary-scale Fe isotope fractionation. *Earth and Planetary Science Letters*, 252(3–4):342–359.

Schuessler, J. A., Botcharnikov, R., Behrens, H., Misiti, B., and Freda, C. (2008). Oxidation state of iron in hydrous phono-tephritic melts. *American Mineralogist*, 93(10):1493–1504.

Schuessler, J. A., Kämpf, H., Koch, U., and Alawi, M. (2016). Earthquake impact on iron isotope signatures recorded in mineral spring water. *Journal of Geophysical Research: Solid Earth*, 121(12):8548–8568.

Schuessler, J. A., Schoenberg, R., Behrens, H., and von Blanckenburg, F. (2007). The experimental calibration of the iron isotope fractionation factor between pyrrhotite and peralkaline rhyolitic melt. *Geochimica et Cosmochimica Acta*, 71:417–433.

Schuessler, J. A., Schoenberg, R., and Sigmarsson, O. (2009). Iron and lithium isotope systematics of the Hekla volcano, Iceland – Evidence for Fe isotope fractionation during magma differentiation. *Chemical Geology*, 258(1–2):78–91.

Schuessler, J. A. and von Blanckenburg, F. (2014). Testing the limits of micro-scale analyses of Si stable isotopes by femtosecond laser ablation multicollector inductively coupled plasma mass spectrometry with application to rock weathering. *Spectrochimica Acta Part B: Atomic Spectroscopy*, 98:1–18.

Shahar, A., Elardo, S. M., and Macris, C. A. (2017). Equilibrium Fractionation of Non-traditional Stable Isotopes: an Experimental Perspective. *Reviews in Mineralogy and Geochemistry*, 82(1):65–83.

Shahar, A., Young, E. D., and Manning, C. E. (2008). Equilibrium high-temperature Fe isotope fractionation between fayalite and magnetite: An experimental calibration. *Earth and Planetary Science Letters*, 268:330–338.

Shatskiy, A., Sharygin, I. S., Gavryushkin, P. N., Litasov, K. D., Borzdov, Y. M., Shcherbakova, A. V., Higo, Y., Funakoshi, K.-I., Palyanov, Y. N., and Ohtani, E. (2013). The system K_2CO_3-$MgCO_3$ at 6 GPa and 900-1450 °C. *American Mineralogist*, 98(8-9):1593–1603.

Sio, C. K., Dauphas, N., Teng, F.-Z., Chaussidon, M., Helz, R. T., and Roskosz, M. (2013). Discerning crystal growth from diffusion profiles in zoned olivine by in situ Mg–Fe isotopic analyses. *Geochimica et Cosmochimica Acta*, 123:302–321.

Sio, C. K., Roskosz, M., Dauphas, N., Bennett, N. R., Mock, T., and Shahar, A. (2018). The isotope effect for Mg-Fe interdiffusion in olivine and its dependence on crystal orientation, composition and temperature. *Geochimica et Cosmochimica Acta*.

Song, W., Xu, C., Chakhmouradian, A. R., Kynicky, J., Huang, K., and Zhang, Z. (2017). Carbonatites of Tarim (NW China): First evidence of crustal contribution in carbonatites from a large igneous province. *Lithos*, 282-283:1–9.

Sossi, P., Foden, J., and Halverson, G. (2012). Redox-controlled iron isotope fractionation during magmatic differentiation: an example from the Red Hill intrusion, S. Tasmania. *Contributions to Mineralogy and Petrology*, 164(5):757–772.

Sossi, P. A., Nebel, O., and Foden, J. (2016). Iron isotope systematics in planetary reservoirs. *Earth and Planetary Science Letters*, 452:295–308.

Sossi, P. A. and O'Neill, H. S. (2017). The effect of bonding environment on iron isotope fractionation between minerals at high temperature. *Geochimica et Cosmochimica Acta*, 196:121–143.

Stagno, V., Cerantola, V., Aulbach, S., Lobanov, S. S., McCammon, C. A., and Merlini, M. (2019). Carbon-bearing phases throughout Earth's interior. In *Deep Carbon: Past to Present*, pages 66–88. Cambridge University Press.

Steinhoefel, G., Horn, I., and von Blanckenburg, F. (2009). Matrix-independent Fe isotope ratio determination in silicates using UV femtosecond laser ablation. *Chemical Geology*, 268(1–2):67–73.

Su, B.-X., Teng, F.-Z., Hu, Y., Shi, R.-D., Zhou, M.-F., Zhu, B., Liu, F., Gong, X.-H., Huang, Q.-S., Xiao, Y., Chen, C., and He, Y.-S. (2015). Iron and magnesium isotope fractionation in oceanic lithosphere and sub-arc mantle: Perspectives from ophiolites. *Earth and Planetary Science Letters*, 430:523–532.

Sun, P., Niu, Y., Guo, P., Duan, M., Chen, S., Gong, H., Wang, X., and Xiao, Y. (2020). Large iron isotope variation in the eastern Pacific mantle as a consequence of ancient low-degree melt metasomatism. *Geochimica et Cosmochimica Acta*, 286:269–288.

Tappe, S., Romer, R. L., Stracke, A., Steenfelt, A., Smart, K. A., Muehlenbachs, K., and Torsvik, T. H. (2017). Sources and mobility of carbonate melts beneath cratons, with implications for deep carbon cycling, metasomatism and rift initiation. *Earth and Planetary Science Letters*, 466:152–167.

Teng, F.-Z., Dauphas, N., and Helz, R. T. (2008). Iron Isotope Fractionation During Magmatic Differentiation in Kilauea Iki Lava Lake. *Science*, 320(5883):1620–1622.

Teng, F.-Z., Dauphas, N., Helz, R. T., Gao, S., and Huang, S. (2011). Diffusion-driven magnesium and iron isotope fractionation in Hawaiian olivine. *Earth and Planetary Science Letters*, 308(3–4):317–324.

Teng, F.-Z., Dauphas, N., Huang, S., and Marty, B. (2013). Iron isotopic systematics of oceanic basalts. *Geochimica et Cosmochimica Acta*, 107:12–26.

Treiman, A. H. (1989). Carbonatite Magma: Properties and Processes. In Bell, K., editor, *Carbonatites: Genesis and Evolution*. Unwin Hyman Ltd.

Vagvoelgyi, V., Frost, R., Hales, M., Locke, A., Kristof, J., and Horváth, E. (2008). Controlled rate thermal analysis of hydromagnesite. *Journal of Thermal Analysis and Calorimetry*, 92(3):893–897.

Van Orman, J. A. and Crispin, K. L. (2010). Diffusion in oxides. *Reviews in Mineralogy and Geochemistry*, 72(1):757–825.

Veksler, I. V., Dorfman, A. M., Dulski, P., Kamenetsky, V. S., Danyushevsky, L. V., Jeffries, T., and Dingwell, D. B. (2012). Partitioning of elements between silicate melt and immiscible fluoride, chloride, carbonate, phosphate and sulfate melts, with implications to the origin of natrocarbonatite. *Geochimica et Cosmochimica Acta*, 79(0):20–40.

Veksler, I. V., Petibon, C., Jenner, G. A., Dorfman, A. M., and Dingwell, D. B. (1998). Trace Element Partitioning in Immiscible Silicate-Carbonate Liquid Systems: an Initial Experimental Study Using a Centrifuge Autoclave. *Journal of Petrology*, 39(11-12):2095–2104.

von Blanckenburg, F., Mamberti, M., Schoenberg, R., Kamber, B. S., and Webb, G. E. (2008). The iron isotope composition of microbial carbonate. *Chemical Geology*, 249(1–2):113–128.

Weidendorfer, D., Schmidt, M. W., and Mattsson, H. B. (2016). Fractional crystallization of Si-undersaturated alkaline magmas leading to unmixing of carbonatites on Brava Island (Cape Verde) and a general model of carbonatite genesis in alkaline magma suites. *Contributions to Mineralogy and Petrology*, 171(5):43.

Weyer, S. (2008). What drives iron isotope fractionation in magma? *Science*, 320:1600 – 1601.

Weyer, S., Anbar, A. D., Brey, G. P., Münker, C., Mezger, K., and Woodland, A. B. (2005). Iron isotope fractionation during planetary differentiation. *Earth and Planetary Science Letters*, 240(2):251–264.

Weyer, S. and Ionov, D. A. (2007). Partial melting and melt percolation in the mantle: The message from Fe isotopes. *Earth and Planetary Science Letters*, 259(1–2):119–133.

Weyer, S. and Seitz, H.-M. (2012). Coupled lithium- and iron isotope fractionation during magmatic differentiation. *Chemical Geology*, 294-295:42–50.

Wilding, C., Wilson, M., Alderman, O., Benmore, C., Weber, J. K. R., Parise, J. B., Tamalonis, A., and Skinner, L. (2016). Low-Dimensional Network Formation in Molten Sodium Carbonate. *Scientific Reports*, 6:24415.

Wilke, M., Farges, F., Partzsch, G. M., Schmidt, C., and Behrens, H. (2007). Speciation of Fe in silicate glasses and melts by in-situ XANES spectroscopy. *American Mineralogist*, 92(1):44–56.

Wilke, M., Farges, F., Petit, P.-E., Brown, G. E., and Martin, F. (2001). Oxidation state and coordination of Fe in minerals: An Fe K-XANES spectroscopic study. *American Mineralogist*, 86(5-6):714–730.

Wilke, M., Partzsch, G. M., Bernhardt, R., and Lattard, D. (2004). Determination of the iron oxidation state in basaltic glasses using XANES at the K-edge. *Chemical Geology*, 213(1):71–87. 7th Silicate Melt Workshop.

Williams, H., Peslier, A., McCammon, C., Halliday, A., Levasseur, S., Teutsch, N., and Burg, J.-P. (2005). Systematic iron isotope variations in mantle rocks and minerals: The effects of partial melting and oxygen fugacity. *Earth and Planetary Science Letters*, 235(1):435–452.

Williams, H. M. and Bizimis, M. (2014). Iron isotope tracing of mantle heterogeneity within the source regions of oceanic basalts. *Earth and Planetary Science Letters*, 404:396–407.

Woolley, A. R. (1989). The spatial and temporal distribution of carbonatites. In Bell, K., editor, *Carbonatites: Genesis and Evolution*, pages 15–37. Unwin Hyman Ltd.

Woolley, A. R. and Kempe, D. R. C. (1989). Carobnatites: Nomenclature, avarage chemical compositions, and element distribution. In Bell, K., editor, *Carbonatites: Genesis and Evolution*, pages 1–14. Unwin Hyman Ltd.

Woolley, A. R. and Kjarsgaard, B. A. (2008). Carbonatite Occurrences of the World: Map and Database. Geological Survey of Canada, Open File 5796.

Wu, H., He, Y., Bao, L., Zhu, C., and Li, S. (2017). Mineral composition control on inter-mineral iron isotopic fractionation in granitoids. *Geochimica et Cosmochimica Acta*, 198:208–217.

Xiao, Y., Teng, F.-Z., Su, B.-X., Hu, Y., Zhou, M.-F., Zhu, B., Shi, R.-D., Huang, Q.-S., Gong, X.-H., and He, Y.-S. (2016). Iron and magnesium isotopic constraints on the origin of chemical heterogeneity in podiform chromitite from the Luobusa ophiolite, Tibet. *Geochemistry, Geophysics, Geosystems*, 17(3):940–953.

Xue, X., Kanzaki, M., Floury, P., Tobase, T., and Eguchi, J. (2018). Carbonate speciation in depolymerized and polymerized (alumino)silicate glasses: Constraints from ^{13}C MAS and static NMR measurements and ab initio calculations. *Chemical Geology*, 479:151–165.

Yaxley, G. M., Ghosh, S., Kiseeva, E. S., Mallik, A., Spandler, C., Thomson, A. R., and Walter, M. J. (2019). CO2-rich melts in Earth. In *Deep carbon: past to present*, pages 129–162. Cambridge University Press.

Young, E. D., Manning, C. E., Schauble, E. A., Shahar, A., Macris, C. A., Lazar, C., and Jordan, M. (2015). High-temperature equilibrium isotope fractionation of non-traditional stable isotopes: Experiments, theory, and applications. *Chemical Geology*, 395:176–195.

Zaitsev, A. N., Keller, J., Spratt, J., Perova, E. N., and Kearsley, A. (2008). Nyerereite–pirssonite–calcite–shortite relationships in altered natrocarbonatites, Oldoinyo Lengai, Tanzania. *The Canadian Mineralogist*, 46(4):843–860.

Zhang, Y., Ni, H., and Chen, Y. (2010). Diffusion data in silicate melts. *Reviews in Mineralogy and Geochemistry*, 72(1):311–408.

Zhao, X., Zhang, H., Zhu, X., Tang, S., and Tang, Y. (2010). Iron isotope variations in spinel peridotite xenoliths from North China Craton: implications for mantle metasomatism. *Contributions to Mineralogy and Petrology*, 160(1):1–14.

Zhao, X., Zhang, H., Zhu, X., Tang, S., and Yan, B. (2012). Iron isotope evidence for multistage melt-peridotite interactions in the lithospheric mantle of eastern China. *Chemical Geology*, 292-293:127–139.

Zhao, X., Zhang, Z., Huang, S., Liu, Y., Li, X., and Zhang, H. (2017a). Coupled extremely light Ca and Fe isotopes in peridotites. *Geochimica et Cosmochimica Acta*, 208:368–380.

Zhao, X. M., Cao, H. H., Mi, X., Evans, N. J., Qi, Y. H., Huang, F., and Zhang, H. F. (2017b). Combined iron and magnesium isotope geochemistry of pyroxenite xenoliths from Hannuoba, North China Craton: implications for mantle metasomatism. *Contributions to Mineralogy and Petrology*, 172(6):40.

Zhao, X.-M., Zhang, H.-F., Zhu, X.-K., Zhu, B., and Cao, H.-H. (2015). Effects of melt percolation on iron isotopic variation in peridotites from Yangyuan, North China Craton. *Chemical Geology*, 401:96–110.

Appendix A

Characterization of the Fe-58 doped silicate glass

The Fe-58 enriched glass has magnetic properties. By design the glass has a relatively high iron content, since sodium and calcium had to be added later in the process as carbonate powders to the powdered glass to add the required CO_2 content. The glass was checked for homogeneity by EMP-WDX analyses (linescans, Table A.1) and BSE images (Figure A.1). In the BSE images homogeneously distributed iron oxide spherules with diameters < 50 nm are visible, that most likely exsolved from the melt into shperules during quenching. It was assumed that iron isotope fractionation would not be influenced by this heterogenity due to the very small size of the spherules compared to the capsule volume.

TABLE A.1: Composition (EMP-Analyses) of the Fe-58 enriched glass (starting material of Sp2, linescan with a 15 µm beam)

	SiO_2	FeO	CaO	Na_2O	Al_2O_3	MgO	$Total_{meas.}$	Total (all Fe as Fe_2O_3)
Average	55.78	19.07	2.96	4.23	13.37	1.24	96.65	98.83
SD	0.53	0.33	0.08	0.17	0.23	0.08	0.84	
n	50							

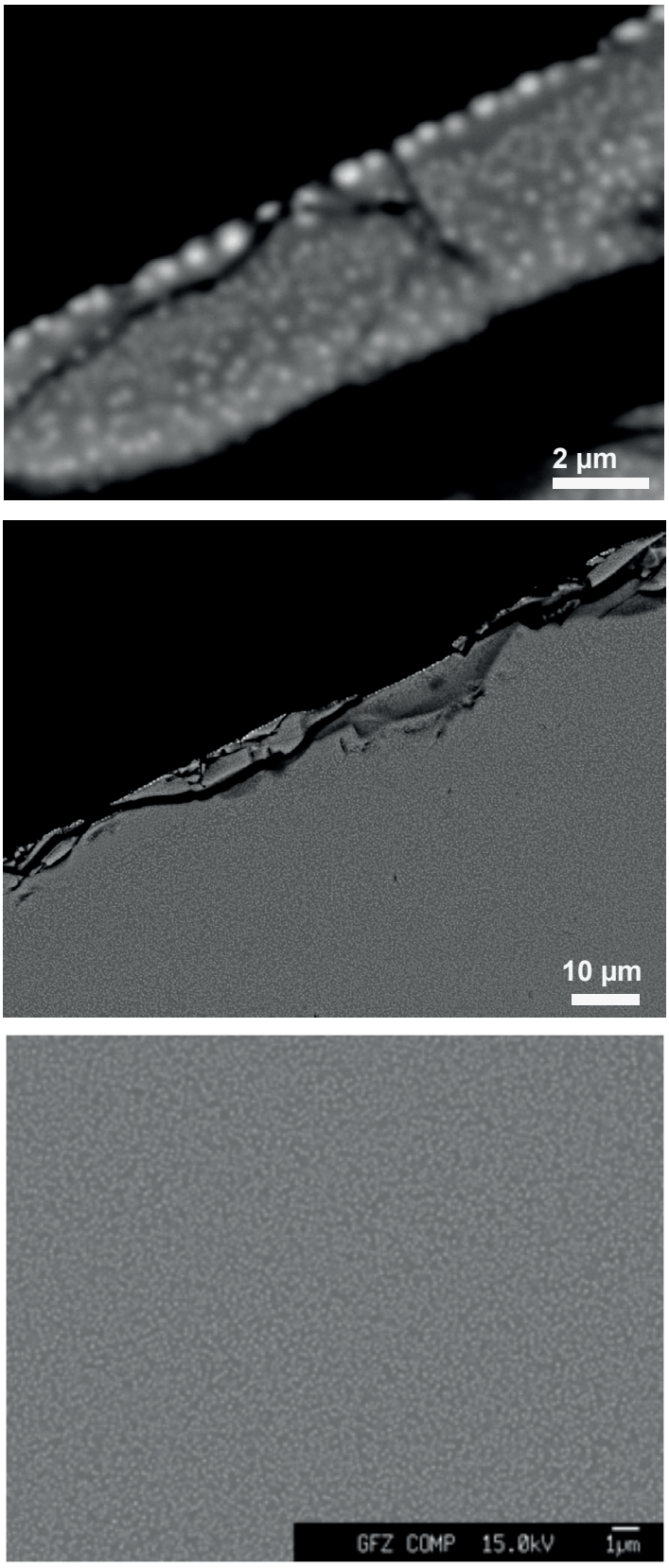

FIGURE A.1: BSE images of the synthetic Fe-58 enriched glass (starting material of Sp2)

Appendix B

Iron isotope compositions of the starting materials

TABLE B.1: Iron isotope compositions of the starting materials

Sample	$\delta^{56}Fe$	2SD	$\delta^{57}Fe$	2SD	$\delta^{58}Fe$	2SD	n	Averages $\delta^{56}Fe$	2SD	$\delta^{57}Fe$	2SD	$\delta^{58}Fe$	2SD
Merck Fe_2O_3													
Equilibration experiments							*28*	*-0.29*	*0.05*	*-0.43*	*0.08*	*-0.51*	*0.36*
Pure Merck Fe_2O_3	-0.30	0.04	-0.44	0.04	-0.55	0.40	6						
Synth. glass $BR_{middle1}$	-0.28	0.06	-0.42	0.06	-0.50	0.38	3						
Synth. glass BR_{rim}	-0.28	0.05	-0.39	0.06	-0.42	0.35	3						
Starting mixture BR	-0.28	0.05	-0.40	0.10	-0.45	0.39	7						
Starting mixture $CaNa_{24}$	-0.28	0.05	-0.43	0.07	-0.61	0.12	3						
Starting mixture $KB_{2.6}$	-0.30	0.07	-0.46	0.08	-0.55	0.54	3						
Starting mixture KB_{5}	-0.30	0.04	-0.44	0.02	-0.55	0.33	3						
Kinetic experiments							*12*	*-0.29*	*0.04*	*-0.40*	*0.10*	*385.50*	*0.48*
Synth. glass $Sp1_{middle}$	-0.31	0.03	-0.44	0.09	n.d.	n.d.	4						
Synth. glass $Sp2_{middle1}$	-0.30	0.03	-0.40	0.09	385.52	0.58	4						
Synth. glass $Sp2_{middle2}$	-0.28	0.03	-0.36	0.05	385.48	0.45	4						
Synth. glass $Sp2_{rim1}$	-0.18	0.05	-0.24	0.11	385.35	0.86	4						
Synth. glass $Sp2_{rim2}$	-0.19	0.03	-0.22	0.02	385.81	0.37	3						
Fe (II) oxalate dihydrate							*10*	*0.39*	*0.09*	*0.57*	*0.14*	*0.89*	*0.49*
Synth. siderite Sid-H01	0.36	0.07	0.54	0.10	0.79	0.66	7						
Synth. siderite Sid-H03	0.42	0.03	0.60	0.11	0.98	0.44	3						
Starting mixture Sp3*	0.02	0.04	0.03	0.06	209.24	0.31	4						

* Consisting of Sid-H03 and glass Sp2

Appendix C

Preparation of the run products

As described above (subsection 2.1.6), the surface roughness < 0.25 µm required for EMP-WDX analyses could not be obtained for the Na-Ca-carb$_{qu}$ samples. Even the preparation of the samples for SEM-EDX analyses proved challenging.

- Due to the extreme differences in hardness between silicate phases, calcite, oxide minerals, and the carbonate quench products, during polishing relief formed easily (Figure C.1). To reduce this effect, the Na-Ca-carb$_{qu}$ was seperated from other phases as thourough as possible.
- To avoid loss of material (Figure C.3), polishing times were kept as short as possible. Furtheremore, the embedded samples were rehardend several times with epoxy under vacuum before starting the polishing routine.
- The Na-Ca-carb$_{qu}$ sample material is highly soluble not only in water but also in ethanol and isopropanol. Therefore, paraffine oil was tested as a medium for polishing. This polishing routine was performed by S. Gehrmann. While the method succeeded in producing a rather plain surface, the oil could not be removed sufficiently from the sample surface (Figure C.2).
- To avoid the sample dissolution during polishing, a manual dry polishing routine using lapping film was developed. After the samples were mounted in epoxy, they were very carefully polished down to the sample surface on silicon carbide abrasive paper (P600, P800, P1200). In between, the mount was cleaned repeatedly with ethanol without contact to any opened sample surface. This was necessary, since cleaning the sample surface between polishing steps in an ultra sonic bath was obviously not possible. Upon reaching the sample surface, polishing was continued on lapping film (6 µm, 3 µm and 1 µm), while the mount surface was cleaned by dry wiping only.

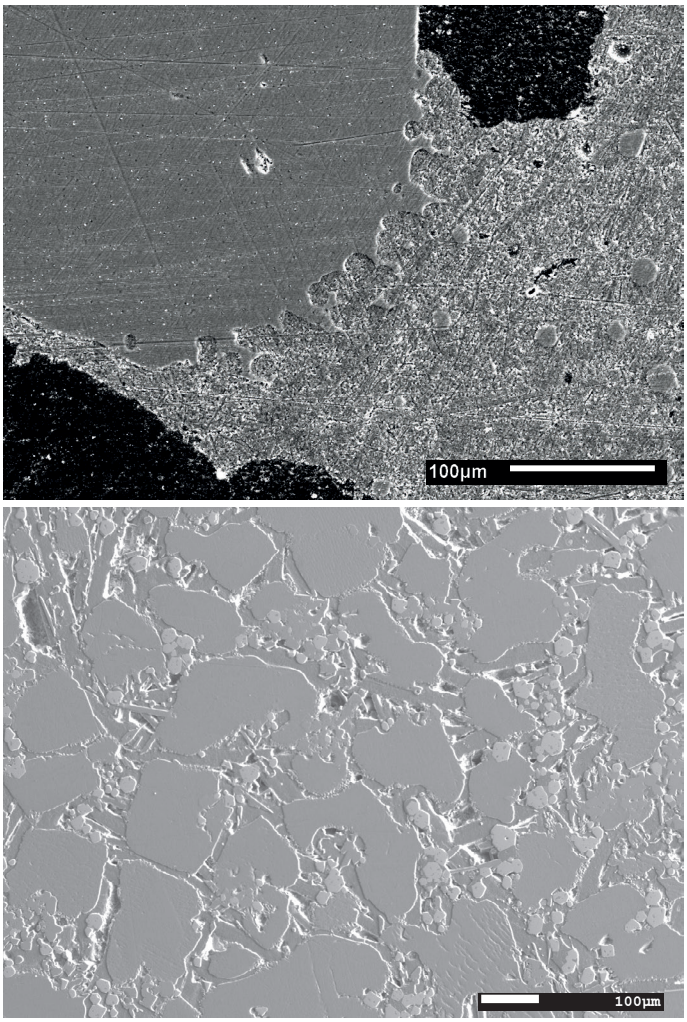

FIGURE C.1: SE images of the polished mounts (samples R01-4 and R16-3, systems $KB_{17.3}$ and KGW_{hAl}) show the relief that formed during polishing of the samples.

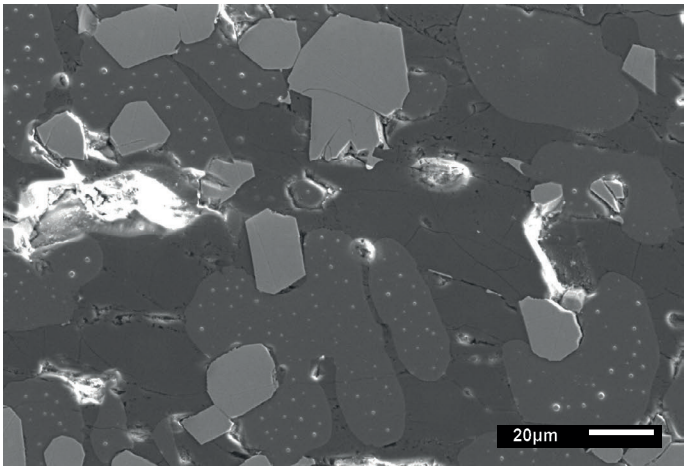

FIGURE C.2: SE image of a polished mount. The light round spots on the sample surface are remnants of paraffine oil, which were drawn from in sample in the SEM vacuum.

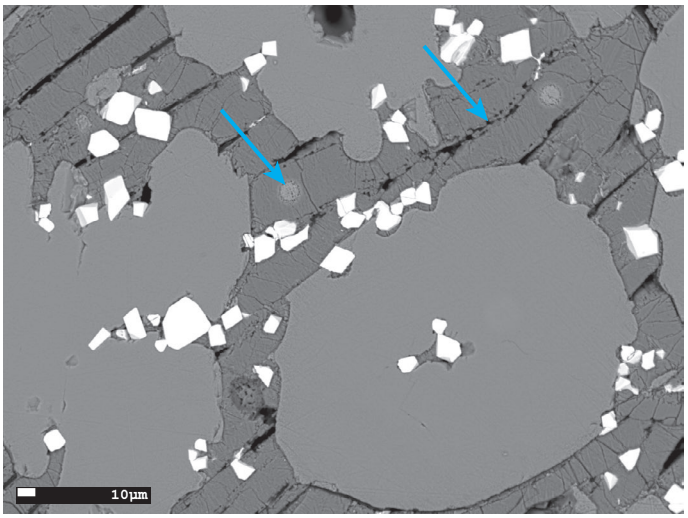

FIGURE C.3: SE image of a polished mount. The arrows point to cavities, where material was lost during polishing, and to light round spots signaling damage by electron beam, respectively.

Appendix D

EDX spectra on the Re inlay

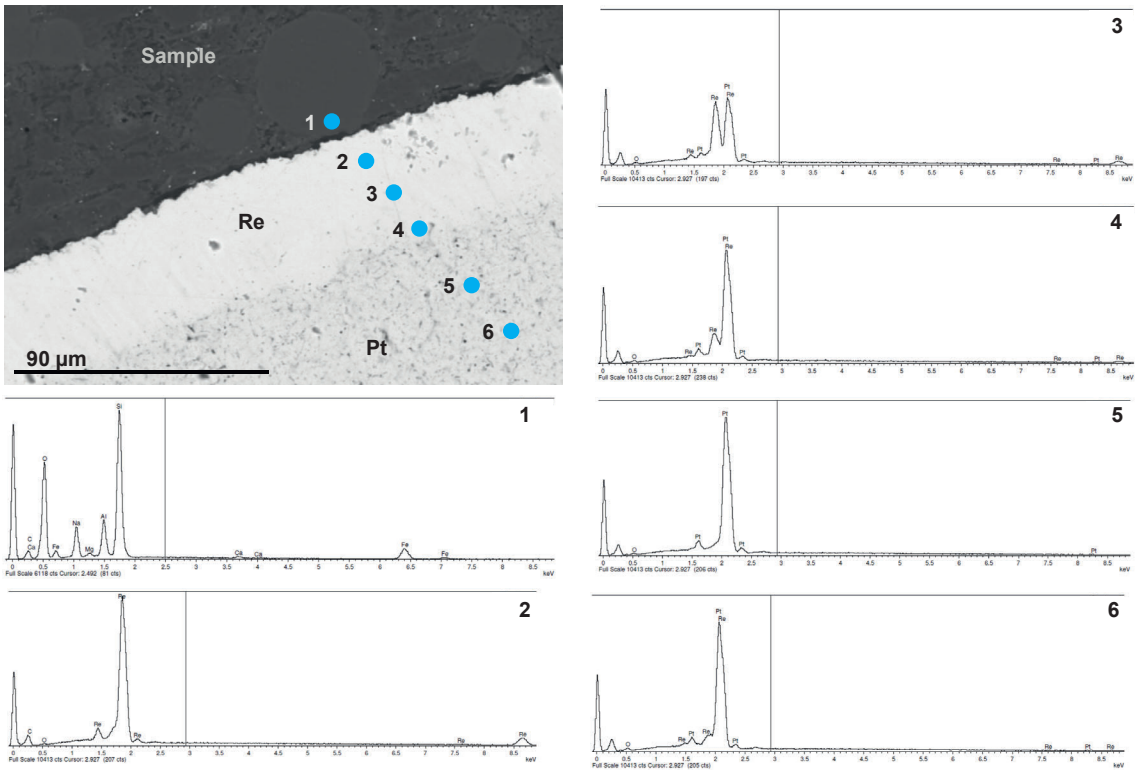

FIGURE D.1: Representative BSE image and EDX-spectra of the Pt capsule and Re inlay